DOCTOR OF PHILOSOPHY

DSP-enabled Reconfigurable Optical Network Devices and Architectures for Cloud Access Networks

Duan, Xiao

Award date:
2018

Awarding institution:
Bangor University

DSP-enabled Reconfigurable Optical Network Devices and Architectures for Cloud Access Networks

Xiao Duan

PRIFYSGOL
BANGOR
UNIVERSITY

A thesis submitted for the degree of

Doctor of Philosophy

School of Computer Science

Bangor University

March 2018

Abstract

To meet the ever-increasing bandwidth requirements, the rapid growth in highly dynamic traffic patterns, and the increasing complexity in network operation, whilst providing high power consumption efficiency and cost-effectiveness, the approach of combining traditional optical access networks, metropolitan area networks and 4-th generation (4G)/5-th generation (5G) mobile front-haul/back-haul networks into unified cloud access networks (CANs) is one of the most preferred "future-proof" technical strategies. The aim of this dissertation research is to extensively explore, both numerically and experimentally, the technical feasibility of utilising digital signal processing (DSP) to achieve key fundamental elements of CANs from device level to network architecture level including: i) software reconfigurable optical transceivers, ii) DSP-enabled reconfigurable optical add/drop multiplexers (ROADMs), iii) network operation characteristics-transparent digital filter multiple access (DFMA) techniques, and iv) DFMA-based passive optical network (PON) with DSP-enabled software reconfigurability.

As reconfigurable optical transceivers constitute fundamental building blocks of the CAN's physical layer, digital orthogonal filtering-based novel software reconfigurable transceivers are proposed and experimentally and numerically explored, for the first time. By making use of Hilbert-pair-based 32-tap digital orthogonal filters implemented in field programmable gate arrays (FPGAs), a 2GS/s@8-bit digital-to-analogue converter (DAC)/analogue-to-digital converter (ADC), and an electro-absorption modulated laser (EML) intensity modulator (IM), world-first reconfigurable real-time transceivers are successfully experimentally demonstrated in a 25km IMDD SSMF system. The transceiver dynamically multiplexes two orthogonal frequency division multiplexed (OFDM) channels with a total capacity of 3.44Gb/s. Experimental results also indicate that the transceiver performance is fully transparent to various subcarrier modulation formats of up to 64-QAM, and that the maximum achievable transceiver performance is mainly limited by the cross-talk effect between two spectrally-overlapped orthogonal channels, which can, however, be minimised by adaptive modulation of the OFDM signals. For further transceiver optimisations, the impacts of major transceiver design parameters including digital filter tap number and subcarrier modulation format on the transmission performance are also numerically explored.

Reconfigurable optical add/drop multiplexers (ROADMs) are also vital networking devices for application in CANs as they play a critical role in offering fast and flexible network reconfiguration. A new optical-electrical-optical (O-E-O) conversion-free, software-switched flexible ROADM is extensively explored, which is capable of providing dynamic add/drop operations at wavelength, sub-wavelength and orthogonal sub-band levels in software defined networks incorporating the reconfigurable transceivers. Firstly, the basic add and drop operations of the proposed ROADMs are theoretically explored and the ROADM designs are optimised. To crucially validate the practical feasibility of the ROADMs, ROADMs are experimentally demonstrated, for the first time. Experimental results show that the add and drop operation performances are independent of the sub-band signal spectral location and add/drop power penalties are <2dB. In addition, the ROADMs are also robust against a differential optical power dynamic range of >2dB and a drop RF signal power range of 7.1dB.

In addition to exploring key optical networking devices for CANs, the first ever DFMA PON experimental demonstrations are also conducted, by using two real-time, reconfigurable, OOFDM-modulated optical network units (ONUs) operating on spectrally overlapped multi-Gb/s orthogonal channels, and an offline optical line terminal (OLT). For multipoint-to-point upstream signal transmission over 26km SSMF in an IMDD DFMA PON, experiments show that each ONU achieves a similar upstream BER performance, excellent robustness to inter-ONU sample timing offset (STO) and a large ONU launch power variation range. Given the importance of IMDD DFMA-PON channel frequency response roll-off, both theoretical and experimental explorations are undertaken to investigate the impact of channel frequency response roll-off on the upstream transmission of the DFMA PON system Such work provides valuable insights into channel roll-off-induced performance dependencies to facilitate cost-effective practical network/transceiver/component designs.

Acknowledgements

First of all, I would like to express my deep and sincere gratitude to my supervisor Dr. Roger Giddings for his continuous guidance, encouragement and support throughout my PhD journey. My sincere gratitude also extends to Dr. Sa'ad Mansoor who provided financial support for my PhD study, and Prof. Jianming Tang who offered constructive and detailed insights and comments on various different aspects of my dissertation research. In addition, Dr. Mingliang Deng also deserves a big thanks for his technical assist.

I am also deeply grateful to Prof. Kun Qiu for introducing me into the field of optical communications throughout my study for the Master's degree at the University of Electronic Science and Technology of China and his recommendation for PhD study in Bangor University.

I would also like to sincerely thank all my colleagues in the optical communications research group and all the friends I know in Bangor. Together we shared lots of unforgettable memories. I would like to wish them all the very best for the future.

Last but not least, I would like to sincerely appreciate my family for their everlasting love and support. To them I dedicate this thesis.

Abbreviations

ADC	Analogue to Digital Converter
AM	Amplitude Modulation
AMOOFDM	Adaptively Modulated Optical OFDM
APD	Avalanche Photodiode
AWG	Arbitrary Waveform Generator
AWGN	Additive White Gaussian Noise
BER	Bit Error Rate
BTB	Back to Back
CANs	Cloud Access Networks
CAP	Carrierless Amplitude and Phase
CAPEX	Capital Expenditure
CD	Chromatic Dispersion
CDF	Cumulative Density Function
CFO	Carrier Frequency Offset
CP	Cyclic Prefix
CTF	Channel Transfer Function
DAC	Digital to Analogue Converter
DBPSK	Differential Binary Phase Shift Keying
DFMA	Digital Filter Multiple Access
DFB	Distributed Feedback Laser
DMD	Differential Mode Dispersion
DML	Directly Modulated DFB Laser
DMT	Discrete Multitone Modulation
DQPSK	Differential Quadrature Phase Shift Keying
DSL	Digital Subscriber Loop
DSO	Digital Storage Oscilloscope
DSP	Digital Signal Processing
EAM	Electro-Absorption Modulator
EDFA	Erbium-Doped Fibre Amplifier
EML	Electro-absorption Modulated Laser
EO	Electrical-to-Optical

FDM	Frequency Division Multiplexing
FEC	Forward Error Correction
FIR	Finite Impulse Responses
FFT	Fast Fourier Transform
FOOFDM	Fast Optical Orthogonal Frequency Division Multiplexing
FOADM	Fixed Optical Add/Drop Multiplexer
FPGA	Field-Programmable Gate Array
HDTV	High-Definition Television
ICI	Inter-Channel-Interference
IIR	Infinite Impulse Responses
IFFT	Inverse Fast Fourier Transform
IMDD	Intensity Modulation and Direct Detection
ISI	Inter-Symbol-Interference
LAN	Local Area Network
LR-PON	Long-Reach Passive Optical Network
MAN	Metropolitan Area Network
MF	Matching Filter
MIMO	Multiple Input, Multiple Output
MMF	Multi-Mode Fiber
MZM	Mach-Zehnder Modulator
NG-PONs	Next Generation Passive Optical Networks
OC	Optical Coupler
OE	Optical-to-Electrical
OFDM	Orthogonal Frequency Division Multiplexing
OLT	Optical Line Terminal
ONU	Optical Network Unit
OOFDM	Optical Orthogonal Frequency Division Multiplexing
OSNR	Optical Signal-to-Noise Ratio
PAM	Pulse Amplitude Modulation
PAPR	Peak-to-Average Power Ratio
PD	Photodetector
PMD	Polarization Mode Dispersion
PON	Passive Optical Network
P/S	Parallel-to-Serial

PSK	Phase Shift Keying
QAM	Quadrature Amplitude Modulation
RF	Radio Frequency
ROADM	Reconfigurable Optical Add/Drop Multiplexer
ROP	Received Optical Power
SIPM	Subcarrier Index-Power Modulated
SCO	Sampling Clock Offset
SDN	Software Defined Networking
SF	Shaping Filter
S/H	Sample-and-Hold
SMF	Single-Mode Fiber
SNR	Signal-to-Noise Ratio
S/P	Serial-to-Parallel
STO	Symbol Timing Offset/Sample Timing Offset
TIA	Transimpedance Amplifier
WDM	Wavelength Division Multiplexing

Contents

1. Introduction

Contents

1.1 Future Network Challenges and Cloud Access Networks

Due to phenomena such as the explosive growth in content consumption by smart mobile devices and the rapidly increasing use of server virtualization and cloud computing services, it is estimated that there was a total of 1.2 zettabyte (ZB) of global internet protocol (IP) data transferred on the internet in 2016 [1]. It is also forecast [1] that by 2021, global IP traffic will reach 3.3 ZB per year, and will increase threefold over the next 5 years and will have increased nearly 127-fold from 2005 to 2021. In addition, it is predicted that smartphone traffic will exceed PC traffic by 2021 [1].

In addition to the unprecedented explosion in internet traffic, there is also a significant change in data traffic patterns happening at present both in today's carrier networks and enterprise data centre networks. On the one hand, end-users are changing network traffic patterns as they push for access to a widely diversified range of unprecedentedly emerging network applications and services such as high-definition (HD) video sharing and online gaming by using many types of devices (smartphones, tablets, laptops, etc.), connecting from anywhere, at any time. This consumerization of various internet content puts pressure on the current network infrastructures to accommodate these personal devices in a dynamic and elastic manner. On the other hand, in contrast to traditional client-server applications where the bulk of communications occur between one client and one server, today's applications access different databases and servers, generating a flurry of machine-to-machine (M2M) traffic before returning data to the end user devices in the traditional traffic pattern. Furthermore, both carriers and enterprises are currently facing reduced profits because of the escalated capital equipment costs and the flattened or even declined revenue [2].

These abovementioned trends are driving the optical communications and networking research community to re-examine traditional network architectures, as such static networks are ill-suited to meet the requirements of highly dynamic seamless access to the various bandwidth-hungry internet services with improved quality of service (QoS). It is noted that the abovementioned trends cannot be addressed simply by increasing the capacity of the traditional networks [2] due to the prohibitively high costs associated with delivering excessive bandwidth provisioning to end users and the aggregation of the high bandwidth user traffic. Therefore, the key challenge is to provide networks that not only meet the future requirements but achieve sufficient provision of services in a cost-effective way. To resolve

these challenging problems, software-defined networking (SDN) has been proposed [3] and there has been a strong research and development initiative world-wide to harness SDN to vastly increase network reconfigurability, flexibility and elasticity with centralized abstraction and virtualization of the network infrastructure [4-8]. The core concept behind the widely pursued SDN solution is that the underlying network is directly managed by applications and services in the top layer via a logically centralized control plane which is decoupled from the data plane. The abstraction facilitates the formation of a technology-agnostic platform which provides a consolidated view of diversified optical technologies and devices, thus allowing for automatic network service provisioning by hiding transmission technology and network infrastructure specific details, whilst providing visibility of the necessary network resources to the applications. In addition, the virtualization facilitates the partitioning of the physical network infrastructure into multiple independent networks each tailored to a specific application or service requirement [9]. As such, the SDN solution allows the network operator not only to rapidly adapt the networks to provide various connection/bandwidth-on-demand services with effective traffic congestion control, but also to generate more on-demand service provision-based revenue with considerably reduced revenue dependence on excessive bandwidth-provisioning only [10].

In terms of the practical applicability of SDN, it is worth addressing that the SDN operation model is particularly desirable for cost-sensitive optical access networks, which are currently facing a rapidly increasing divergence between required bandwidth provision and revenue growth. The most "future-proof" cost-effective technical strategy for massive deployment of optical access networks is passive optical networks (PONs) which are standardised and extensively deployed worldwide. Furthermore, there is extensive research and development activity targeting the next-generation PONs (NG-PONs) [11, 12]. Consequently, recent years have seen attention moving away from the traditional time division multiple access (TDMA) PONs [13, 14] to wavelength division multiple access (WDMA) PONs [15, 16], to hybrid TWDMA PONs [17, 18], to frequency division multiple access (FDMA) PONs [19, 20], and to orthogonal frequency division multiple access (OFDMA) PONs [21, 22]. However, these developments are basically aimed at increasing network capacity and are not specifically designed to provide a highly dynamic and elastic network architecture. To avoid excessive costs a challenge of future optical access networks is to provide flexible and reconfigurable networks whilst using the existing fibre infrastructure. Furthermore, the convergence of access and metro networks is already a well-established trend [23] needed

to meet future requirements such as high ubiquity, high flexibility, low power consumption, low operational costs as well as provision of multi-service and multi-tenancy. Convergence of access and metro networks however faces many challenges associated with the required increase in fibre transmission distances. One solution for such convergence is the Long-Reach PON (LR-PON) architecture [23]. In the LR-PON, the maximum PON reach is extended to >100km through the use of in line optical amplifiers in the optical distribution network (ODN). Even though LR-PON can also support the metro network by directly linking access fibre to the metro network nodes, it does not inherently increase the network flexibility, in terms of functions such as fine granularity bandwidth provisioning or network slicing, for increased network utilisation efficiency.

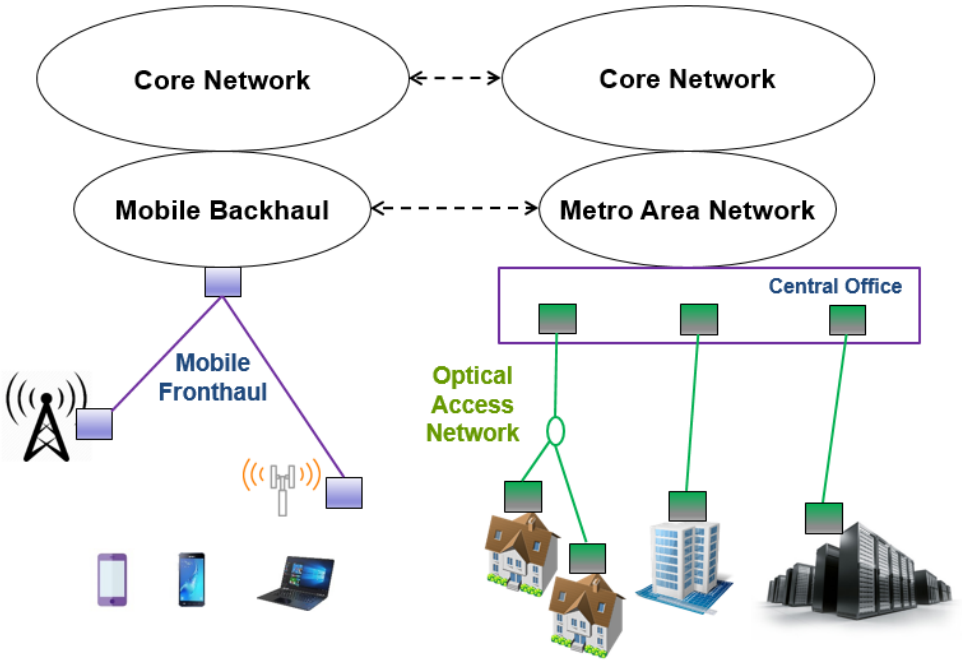

Fig.1 Current network configuration for fixed and mobile services

In addition to the evolution in optical access networks, wireless networks are also subject to significant evolutions from third-generation (3G) and fourth-generation (4G) to fifth-generation (5G). The Next Generation Mobile Networks (NGMN) Alliance [24] has envisaged various 5G demands such as ultra-high data rate and mobility, ultra-low latency and cost in order to deliver End-to-End (E2E) services. It is expected that mobile broadband technologies will further evolve rapidly, and the 5G mobile technologies will realize access speeds of up to 10 Gb/s per user [25]. The cloud radio access network (C-RAN) [26] has been playing an essential role in next-generation mobile networks to support efficient

operation of both macro cells and small cells. Mobile fronthaul [27] and mobile backhaul [28] are also both key network elements in the C-RAN architecture. To efficiently support numerous small cells for increased network capacity, mobile fronthaul connects centralized baseband units (BBUs) with remote radio heads (RRHs) located in each cell. The BBUs support centralised baseband processing for multiple cells thus reducing complexity and cost of the RRHs. The C-RAN also supports technologies such as massive multiple-input multiple-output (M-MIMO) [29] which is a key technology since 3G, and coordinated multi-point process (CoMP) which improves performance at cell edges. Mobile backhaul connects BBUs with the mobile core networks to transport the baseband data streams to mobile switching centres (MSCs). To meet the ever-increasing mobile bandwidth demands, optical network (metro and access) technologies and architectures have been used to support mobile fronthaul and backhaul [30] as there is a comparable synergy between the above two network platforms in terms of data rate, latency and traffic patterns.

Use can be made of the aforementioned synergy, from the practical network design and deployment point of view, to reduce the enormous investments network operators make in independent mobile and fixed optical network infrastructures, as seen in Fig. 1.1. It is therefore of great benefit to heterogeneously amalgamate access networks, metropolitan area networks and 4G/5G mobile fronthaul/backhaul networks into a seamlessly integrated dynamically reconfigurable cloud access network (CAN) [31-34] to provide both broadband wired and wireless services over the existing network infrastructures. Such provision can bring further improved network bandwidth utilization efficiency, network operation functionality, power consumption efficiency together with reduced network capital expenditure (CAPEX) and operation expenditure (OPEX). It is also greatly advantageous if the CANs not only have strong adaptability to highly dynamic traffic with arbitrary signal bandwidth granularity, but can also simultaneously accommodate various major network characteristics including, for example, signal modulation format, signal detection scheme, WDM grid, multiple access technique, as well as network topology. In addition, the CANs are also envisaged to support SDN down to the physical layer with a wide diversity of SDN features.

In order to realise future CANs capable of not only providing various types of network services but also offering highly desired synergy with the SDN solution, it is easy to comprehend that software reconfigurable adaptive optical transceivers, reconfigurable

optical add/drop multiplexers (ROADMs) and flexible PONs enabled by digital integrated circuit-based digital signal processing (DSP) play crucial roles in enabling the SDN-based CANs paradigm at the physical layer. All the above-mentioned elements require cost-effective implementation as well as high scalability and adaptability, DSP is therefore a key enabler for realising the future CANs due to the high-performance processing capability and low cost associated with mass produced digital electronics. Apart from performing advanced signal modulation and adaptive linear/nonlinear compensations of component/system/network impairments [35, 36], the expansion of the reconfigurable optical transceiver's embedded DSP functions are envisaged to improve transceiver controllability, intelligence, cost-effectiveness and overall system compactness and power consumption efficiency compared to SDN solutions employing existing conventional transceivers, and more importantly, to introduce extra on-line reconfigurable networking functionalities, such as channel add/drop, which are essential for CANs. By making use of digital orthogonal filtering implemented with hardware-based DSP, this dissertation research aims to numerically and experimentally investigate a series of novel techniques with high potential for practically implementing future CANs including: i) new software reconfigurable optical transceivers with channel multiplexing/demultiplexing in the digital domain without involving any extra analogue hardware [37], ii) new optical-electrical-optical (O-E-O) conversion-free, DSP-switched flexible ROADMs [38], and iii) a new PON access technique termed digital filter multiple access (DFMA) PONs [39]. The dissertation work not only verifies theoretical predictions but also proves the technical feasibility through practical realization of the abovementioned techniques for future CANs.

1.2 Major Achievements of the Dissertation Research

To address the challenges outlined above, the dissertation research work has been carried out to numerically and experimentally investigate software reconfigurable transceivers, DSP-switched flexible ROADMs and DSP-enabled flexible PONs, all utilizing DSP-embedded digital orthogonal filters, for application in future SDN-based CANs. The major achievements of the research work are summarized as followings:

- **Real-time experimental demonstrations and numerical investigation of software reconfigurable optical OFDM transceivers for SDN-based CANs [40, 41].**

For the first time, novel real-time reconfigurable optical transceivers with on-line software-controllable digital orthogonal filtering-enabled channel reconfigurability and transmission performance adaptability have been numerically investigated and experimentally demonstrated. In numerical simulations, the impacts of major transceiver design aspects including the number of digital filter taps and different modulation formats on the transmission performance have been investigated in an IMDD SSMF system consisting of two digital orthogonal filtering-based channels using OFDM-modulated signals. The optimum digital filter tap count is subsequently identified. In the real-time experimental demonstrations, by making use of Hilbert-pair-based 32-tap digital orthogonal filters implemented in FPGAs, a 2GS/s@8-bit digital-to-analogue converter (DAC)/analogue-to-digital converter (ADC), and an electro-absorption modulated laser (EML) intensity modulator (IM), the reconfigurable transceivers have been demonstrated supporting end-to-end real-time simultaneous adaptive transmissions, within a 1GHz signal spectrum region, of an in-phase OOFDM channel and a quadrature-phase OOFDM channel over a 25km SSMF intensity-modulation and direct-detection (IMDD) system. In addition, experimental explorations have also been undertaken of the key physical mechanisms limiting the maximum achievable transmission performance, impacts of transceiver's channel multiplexing/demultiplexing operations on the system bit error rate (BER) performance, and the feasibility of utilizing adaptive modulation to combat impairments associated with low-complexity digital filter DSP designs. Furthermore, experimental results have also indicated that the transceiver incorporating a fixed digital orthogonal filter architecture can be made transparent to various signal modulation formats of up to 64-quadrature amplitude modulation (QAM).

- **Experimental demonstration and numerical investigation of DSP-switched flexible ROADMs for CANs [38, 42].**

  For the first time, making use of Hilbert-pair-based digital filtering, intensity modulation and passive optical coupling, new optical filter- and O-E-O conversion-free flexible DSP-switched ROADMs have been numerically investigated and experimentally demonstrated. In the numerical simulations, add and drop operation characteristics at sub-wavelength and spectrally-overlapped orthogonal sub-band

levels have been explored using ideal optical add/drop elements, to provide an initial validation of the technical feasibility of the proposed ROADMs. The experimental work has been undertaken to perform DSP-enabled dynamic physical-layer add and drop operations at sub-wavelength and spectrally overlapped orthogonal sub-band levels. Extensive experimental explorations of add and drop operations' robustness to variations in both differential optical power dynamic range and drop RF signal power are also undertaken in IMDD-based optical network nodes incorporating commercially-available, low-cost electrical/optical components.

- **Experimental demonstration of upstream transmission in digital filter multiple access PONs with real-time reconfigurable optical network units (ONUs) [43].**

  As IMDD DFMA PONs are essential elements for realising reconfigurable CANs, multipoint-to-point upstream signal transmission in IMDD DFMA PONs is experimentally demonstrated for the first time, using two real-time, reconfigurable, OOFDM-modulated ONUs and an offline optical line terminal (OLT). Experimental demonstrations show that each ONU achieves similar upstream BER performance, excellent tolerance to inter-ONU sample timing offset and a relatively large ONU launch power variation range.

- **Numerical investigation of upstream performance tolerance of IMDD DFMA PONs to channel frequency response roll-off [44].**

  The channel frequency response characteristics of the DFMA PON influence the orthogonality between ONUs assigned to orthogonal channels, this leads to cross-channel interference (CCI) and subsequent system performance degradation, the impacts of the channel frequency response roll-off effect on upstream optical OFDM transmission performance in DFMA PONs based on IMDD are numerically investigated, for the first time. Tolerance to channel roll-off is explored in terms of BER performance versus received optical power, ONU transmission capacity, ONU launch power variation range and inter-ONU sample timing offset (STO). The effect of signal bandwidth is also explored by comparing tolerance to the channel roll-off effect for two different signal bandwidths. Over all of the aforementioned aspects, good agreements are obtained between numerical simulations and experimental measurements in [43]. The results provide important insights into channel roll-off-

induced performance dependencies to facilitate cost-effective designs of both DFMA transceivers and IMDD DFMA PONs for application in CANs.

The above-mentioned work has resulted in the publication of 3 papers in world-leading journals [40, 43, 44], 2 papers in international conferences including the world-leading OFC conference [41, 42] and 1 full paper submitted to major international journal.

1.3 Thesis Structure

This thesis is organized into six chapters. A review of current and future optical access networks is presented in Chapter 2 and the work performed solely as part of this research is presented in Chapters 3-6. The chapters are outlined as follows:

This chapter provides a brief introduction to the research work including future network challenges, the motivation of designing CANs and the motivation for researching software-reconfigurable optical transceivers, flexible ROADMs and DSP-enabled flexible PONs for CANs.

Chapter 2: To enable a better understanding of the work presented in the thesis, key aspects of current and future optical access networks are described in detail, including PONs, advanced modulation formats, SDN, DSP-based optical transceivers and ROADMs. In addition, major requirements of future CANs are also discussed.

Chapter 3: In this chapter both numerical and experimental investigations are undertaken to explore the technical feasibility and performance of novel software reconfigurable transceivers, for application in CANs, utilizing digital orthogonal filters embedded in DSP logic. The numerical simulation work investigates the impacts of major transceiver design aspects, including the number of digital filter taps and different modulation formats, on the transmission performance in an IMDD SSMF system consisting of two digital orthogonal filtering-based channels using OFDM-modulated signals. Numerical simulation results show that 32-taps provide the optimum number of digital filter coefficients to achieve a good trade-off between performance and DSP complexity. It was also demonstrated that different modulation formats ranging from 16-QAM to 256-QAM can be supported. The experimental

demonstration section firstly describes in detail, the FPGA-based real-time DSP platform, the overall DSP architecture of the reconfigurable transceivers and the DSP design and implementation of the digital orthogonal finite impulse response (FIR) filters. The chapter then presents the first experimental demonstration and analysis of the implemented real-time reconfigurable transceivers with on-line software-controllable channel reconfigurability and transmission performance adaptability utilizing Hilbert-pair-based 32-tap digital orthogonal filters. It is demonstrated that the transceivers can support real-time adaptive transmission of a 2.03Gb/s in-phase OOFDM channel and a 1.41Gb/s quadrature-phase OOFDM channel over a 25km SSMF IMDD system. In addition, experimental results show that the cross-talk effect between these two channels are the major physical mechanism limiting the maximum achievable performance. Furthermore, it is also shown that the transceivers incorporating a fixed digital orthogonal filter architecture can be made transparent to various signal modulation formats of up to 64-QAM.

Chapter 4: In this chapter both numerical and experimental investigations are undertaken to explore newly proposed DSP-enabled flexible ROADMs for application in IMDD-based CANs. In the numerical simulation work, add and drop operation characteristics at sub-wavelength and spectrally-overlapped orthogonal sub-band levels are investigated using ideal optical add/drop elements, to provide an initial validation of the technical feasibility of the proposed ROADMs. Numerical simulation results show that the add operation brings no power penalty at both sub-wavelength and sub-band levels, whilst the drop operation gives rise to 1.6 dB power penalty (FEC limit of $1x10^{-3}$) due to the imperfect digital filter design. In the experimental demonstration work, physical-layer add and drop operation performances of the proposed ROADMs are demonstrated for the first time. The ROADM's robustness to variations in both differential optical power dynamic range and drop RF signal power are also investigated. Experimental results show that the add and drop operation performances are independent of the sub-band signal spectral location, and the maximum ROADM-introduced power penalties are only 1.8dB for the add operation and 1.2dB for the drop operation (FEC limit of $2.3x10^{-3}$). In addition, the add operation can tolerate a differential optical power dynamic range of >2dB with received optical power fixed at -12dBm. Whilst for the drop operation, an optical power penalty as low as 2dB is observed over a broad drop RF signal power variation range as large as 7.1dB. The experimental work clearly demonstrates the technical feasibility of the proposed ROADM.

Chapter 5: In this chapter experimental demonstrations are performed, for the first time, to verify the feasibility and explore the performance of multipoint-to-point upstream signal transmission in IMDD DFMA PONs for application in CANs. Here two real-time, reconfigurable, OOFDM-modulated ONUs are employed with and an offline implemented OLT. Experimental results show that each ONU achieves similar upstream BER performance, excellent tolerance to inter-ONU sample timing offset and a relatively large ONU launch power variation range. Furthermore, as channel frequency response roll-off influences the orthogonality between the orthogonal DFMA channels and leads to CCI and subsequent system performance degradation in DFMA PONs, numerical investigations are also undertaken to explore the impacts of different levels of channel roll-off for different signal bandwidths in upstream DFMA PONs. Transmission performance is analysed in terms of BER versus received optical power, ONU transmission capacity, ONU launch power variation range and inter-ONU STO. Over all the aforementioned aspects, excellent agreements are obtained between numerical simulations and the experimental measurements. These observed impacts of channel roll-off on the various performance aspects provide important insights into the trade-offs between selected component/channel characteristics and performance, thus facilitating the implementation of cost-effective designs of both DFMA transceivers and IMDD DFMA PONs for application in CANs.

Finally, Chapter 6 summarizes the thesis and suggests future research work.

References

[1] Cisco White Paper “Cisco Visual Networking Index: Forecast and Methodology, 2016–2021”, June 6, 2017

[2] ONF White Paper “Software-Defined Networking: The New Norm for Networks”, April 13, 2012

[3] M. Casado, “Architectural Support for Security Management in Enterprise Networks,” Doctoral, Stanford University, Stanford, CA, USA, 2007

[4] A. Felix, N. Borges, H. P. Wu, M. Hanlon, M. Birk, and A. Tschersich, "Multi-layer SDN on a commercial network control platform for packet optical networks," in *Optical Fiber Communication Conference (OFC)*, San Francisco, 2014, paper Th5A.1.

[5] X. Li, K. Kanonakis, N. Cvijetic, A. Tanaka, C. M. Qiao, and T. Wang, “Joint bandwidth provisioning and cache management for video distribution in software-defined passive optical networks,” in *Optical Fiber Communication Conference (OFC)*, San Francisco, 2014, paper Tu3F.5.

[6] L. Liu, Y. W. Yin, M. Xia, M. Shirazipour, Z. Q. Zhu, R. Proietti, Q. Xu, S. Dahlfort, and S. J. Ben Yoo, “Software-defined fragmentation-aware elastic optical networks enabled by openFlow,” in *European Conference and Exhibition on Optical Communication (ECOC)*, (Optical Society of America, 2013), paper We.3.E.2.

[7] N. Cvijetic, M. Angelou, A. Patel, P. N. Ji, and T. Wang, “Defining optical software-defined networks (SDN): from a compilation of demos to network model synthesis,” in *Optical Fiber Communication Conference (OFC)*, Anaheim, 2013, paper OTh1H.1.

[8] N. Amaya, S. Yan, M. Channegowda, B. R. Rofoee, Y. Shu, M. Rashidi, Y. Ou, E. Hugues-Salas, G. Zervas, R. Nejabati, D. Simeonidou, B.J. Puttnam, W. Klaus, J. Sakaguchi, T. Miyazawa, Y. Awaji, H. Harai, and N. Wada, “Software defined

networking (SDN) over space division multiplexing (SDM) optical networks: features, benefits and experimental demonstration," *Opt. Express*, vol. 22, no. 3, pp. 3638-3647, 2014.

[9] M. Channegowda, R. Nejabati, and D. Simeonidou, "Software-defined optical networks technology and infrastructure: enabling software-defined optical network operations [Invited]," *J. Opt. Commun. Netw,*, vol. 5, no. 10, pp. A274-A282, 2013.

[10] N. Cvijetic, "Software-defined optical access networks for multiple broadband access solutions," in *OptoElectronics and Communications Conference and Photonics in Switching (OECC/PS),* (Optical Society of America, 2013), paper TuP2-1.

[11] D. Nesset, "The PON roadmap," in *Optical Fiber Communication Conference (OFC),* Anaheim, 2016, paper W4C.1.

[12] J. L. Wei, K. Grobe, C. Wagner, E. Giacoumidis, H. Griesser, "40 Gb/s Lane Rate NG-PON using Electrical/Optical Duobinary, PAM-4 and Low Complex Equalizations," in *Optical Fiber Communication Conference (OFC),* Anaheim, 2016, paper Tu3C.5.

[13] A.R. Dhaini, P.H. Ho, G. X. Shen, and B. Shihada, "Energy efficiency in TDMA-based next-generation passive optical access," *IEEE/ACM Trans. Netw*., vol. 22, no. 3, pp. 850-863, 2013.

[14] S. Li, Z.C. Ye, N. Cheng, and X. Liu, "Demonstration of a Real-Time 25-Gb/s TDM-PON System with 25-Gb/s Downstream Based on Optical Duobinary and 10-Gb/s Burst-Mode Upstream Based on NRZ," in *Optical Fiber Communication Conference (OFC),* Anaheim, 2016, paper Th1I.3.

[15] K. Honda, T. Kobayashi, T. Shimada, J. Terada, and A. Otaka, "WDM passive optical network managed with embedded pilot tone for mobile fronthaul," in *European Conference on Optical Communication (ECOC),* Valencia, 2015, paper ID 0093.

[16] C. Wei, K. Chen, L. Chen, C. Lin, W. Huang, J. Chen, "High-Capacity Carrierless Amplitude and Phase Modulation for WDM Long-Reach PON Featuring High Loss Budget," *J. Lightwave. Technol.*, vol. 35, no. 4, pp. 1075-1082, 2017.

[17] K. Kondepu, L. Valcarenghi, P. Castoldi, "Reconfiguration triggering optimization in TWDM PONs with fluctuating load," in *Optical Fiber Communication Conference (OFC),* Anaheim, 2016, paper W2A.67.

[18] X. Wang, L. Wang, C. Cavdar, M. Tornatore, G.B. Figueiredo, H.S. Chung, H.H. Lee, S. Park, B. Mukherjee, "Handover reduction in virtualized cloud radio access networks using TWDM-PON fronthaul," *J. Opt. Commun. Netw*., vol. 8, no. 12, pp. B124-B134, 2016.

[19] G. F. Bai, C. T. Lin, C. H. Lin, C. H. Ho, C. C. Wei, Y. Jiang, S. Chi and L. Hu, "Delay division multiplexing DFT spread FDMA PON by sub-Nyquist sampling rate receiver," in *Optical Fiber Communication Conference (OFC),* Anaheim, 2016, paper Th3C.6.

[20] A. Gatto, P. Parolari, M. Brunero, P. Martelli, R. Brenot, P. Boffi, "RSOA-based FDM PON upstream with flexible multiple access capabilities in an NG-PON2 compliant architecture," *J. Opt. Commun. Netw*., vol. 8, no. 5, pp. 302-307, 2016.

[21] X. Q. Jin, E. Hugues-Salas, R. P. Giddings, J. L. Wei, J. Groenewald, and J. M. Tang, "First real-time experimental demonstrations of 11.25Gb/s optical OFDMA PONs with adaptive dynamic bandwidth allocation," *Opt. Express*, vol. 19, no. 21, pp. 20557-20570, 2011.

[22] I. N. Cano, X. Escayola, P. C. Schindler, M. C. Santos, V. Polo, J. Leuthold, I. Tomkos, J. Prat, "Experimental demonstration of a statistical OFDM-PON with multiband ONUs and elastic bandwidth allocation," *J. Opt. Commun. Netw*., vol. 7, no. 1, pp. A73-A79, 2015.

[23] M. Ruffini, "Access-metro convergence in next generation broadband networks," in *Optical Fiber Communication Conference (OFC),* Anaheim, 2016, paper Th4B.1.

[24] S. Gosselin, A. Pizzinat, X. Grall, D. Breuer, E. Bogenfeld, S. Krauß, J. Alfonso T. Gijón, A. Hamidian, N. Fonseca, and B. Skubic, "Fixed and Mobile Convergence:

Which Role for Optical Networks?," *J. Opt. Commun. Netw.*, vol. 7, no. 11, pp. 1075-1083, 2015.

[25] J. Kani, J. Terada, K. Suzuki, and A. Otaka, "Solutions for Future Mobile Fronthaul and Access-Network Convergence," *J. Lightwave Technol.*, vol. 35, no. 3, pp. 527-534, 2017.

[26] A. Gatto, P. Boffi, L. Combi, P. Parolari, U. Spagnolini, R. Brenot, M. Martinelli, "LTE-A Mobile Fronthaul Exploiting Pulse-Width Modulation in a RSOA-based WDM PON," in *Optical Fiber Communication Conference (OFC)*, Anaheim, 2016, paper W3C.6.

[27] B. G. Kim, H. Kim, Y. C. Chung, "Impact of Multipath Interference on the Performance of RoF-Based Mobile Fronthaul Network Implemented by Using DML," *J. Lightwave. Technol.*, vol. 35, no. 2, pp. 145-151, 2017.

[28] J. W. Zhang, J. Wang, M. Xu, F. Lu, L. Cheng, J. J. Yu, G. K. Chang, "Full-Duplex Mobile Backhaul Transportation based on Fiber-Wireless Integrated FSO and MMW Hybrid Links with Adaptive Signal Processing to Combat," in *European Conference and Exhibition on Optical Communication (ECOC)*, 2016, pp. 1-3.

[29] C. H. Ye, X. F. Hu, X. A. Huang, Q. J. Chang, Z. S. Gao, S. M. Xiao, X. Sun, K. B. Zhang, "Cloud-based Indoor Wireless Access and Fronthaul Solution for High Capacity MIMO Services using Fixed Network Architecture of Economical LAN Cables and Fiber," in *Optical Fiber Communication Conference (OFC)*, Anaheim, 2016, paper W2A.59.

[30] X. Liu and F. Effenberger, "Emerging Optical Access Network Technologies for 5G Wireless [Invited]," *J. Opt. Commun. Netw.*, vol. 8, no. 12, pp. B70-B79, 2016.

[31] S. Gosselin, A. Pizzinat, X. Grall, D. Breuer, E. Bogenfeld, S. Krauß, J. Alfonso T. Gijón, A. Hamidian, N. Fonseca, and B. Skubic, "Fixed and Mobile Convergence: Which Role for Optical Networks?," *J. Opt. Commun. Netw.*, vol. 7, no. 11, pp. 1075-1083, 2015.

[32] J. E. Mitchell, "Integrated wireless backhaul over optical access networks," *J. Lightwave Technol.*, vol. 32, no. 20, pp. 3373-3382, 2014.

[33] P. Chanclou, A. Cui, F. Geilhardt, J. Nakamura and D. Nesset, "Network operator requirements for the next generation of optical access networks," *IEEE Network*, vol. 26, no. 2, pp. 8-14, 2012.

[34] Y. Okumura and J. Terada, "Optical network technologies and architectures for backhaul/fronthaul of future radio access supporting big mobile data," in *Optical Fiber Communication Conference (OFC),* San Francisco, 2014, paper Tu3F.1.

[35] R. P. Giddings, "Real-time digital signal processing for optical OFDM-based future optical access networks," *J. Lightwave. Technol.,* vol. 32, no. 4, pp. 553-570, 2014.

[36] M. Morant, T. M. F. Alves, R. Llorente, and A. V. T. Cartaxo, "Broadband impairment compensation in hybrid fiber-wireless OFDM long-reach PONs," *J. Lightwave. Technol.*, vol. 32, no. 7, pp. 1387-1393, 2014.

[37] M. Bolea, R. P. Giddings, and J. M. Tang, "Digital orthogonal filter-enabled optical OFDM channel multiplexing for software-reconfigurable elastic PONs," *J. Lightwave. Technol.*, vol. 32, no. 6, pp. 1200-1206, 2014.

[38] W. Jin, X. Duan, Y. X. Dong, B. Y. Cao; R. P. Giddings, C. F. Zhang, K. Qiu, J. M. Tang, "DSP-Enabled Flexible ROADMs Without Optical Filters and O-E-O Conversions," *J. Lightwave. Technol.,* vol. 33, no. 19, pp. 4124-4131, 2015.

[39] M. Bolea, R. P. Giddings, M. Bouich, C. Aupetit-Berthelemot, J. M. Tang, "Digital filter multiple access PONs with DSP-enabled Software Reconfigurability," *J. Opt. Commun. Netw*., vol. 7, no. 4, pp. 215-222, 2015.

[40] X. Duan, R. P. Giddings, M. Bolea, Y. Ling, B. Cao, S. Mansoor, and J. M. Tang, "Real-time experimental demonstrations of software reconfigurable optical OFDM transceivers utilizing DSP-based digital orthogonal filters for SDN PONs," *Opt. Express*, vol. 22, no. 16, pp. 19674-19685, 2014.

[41] X. Duan, R. P. Giddings, M. Bolea, Y. Ling, S. Mansoor, and J. M. Tang, "Real-time Demonstrations of Software Reconfigurable Optical OFDM Transceivers Utilising DSP-based Digital Orthogonal Filters for Channel Multiplexing," in *Asia Communications and Photonics Conference (ACP),* Shanghai, 2014, paper AW3E.1.

[42] X. Duan, M. L. Deng, W. Jin, R. P. Giddings, S. Mansoor, and J. M. Tang, "Experimental Demonstration of DSP-enabled Drop Operations of Flexible ROADMs Excluding Optical Filters and O-E-O Conversions," in *Optical Fiber Communication Conference (OFC),* Anaheim, 2016, paper M3E.4.

[43] X. Duan, R. P. Giddings, S. Mansoor, and J. M. Tang, "Experimental Demonstration of Upstream Transmission in Digital Filter Multiple Access PONs With Real-Time Reconfigurable Optical Network Units," *J. Opt. Commun. Netw*., vol. 9, no. 1, pp. 45-52, 2017.

[44] X. Duan, R.P. Giddings, S. Mansoor, and J.M. Tang, "Performance Tolerance of IMDD DFMA PONs to Channel Frequency Response Roll-off," *IEEE Photon. Technol. Lett*., vol. 29, no. 19, pp. 1655-1658, 2017.

2. Current and Future Optical Access Networks

Contents

2.1 Introduction

This chapter provides the introduction to the essential aspects of CANs including PONs, advanced modulation formats, SDN, DSP-based optical transceivers and ROADMs which also form the foundation of the work presented in the thesis.

2.2 Passive Optical Network (PON) Technologies

2.2.1 Basic Concept of Passive Optical Networks

PONs have emerged as a promising and attractive solution to deliver broadband services to a large number of subscribers. A PON leverages a point-to-multipoint physical network topology in which a passive optical splitter/coupler is used to enable a single optical fibre of several 10s of kilometres, to serve multiple end-users co-located within a few kilometres. A key advantage is that no active power-consuming elements are deployed in the signal path from the source to the destination [1].

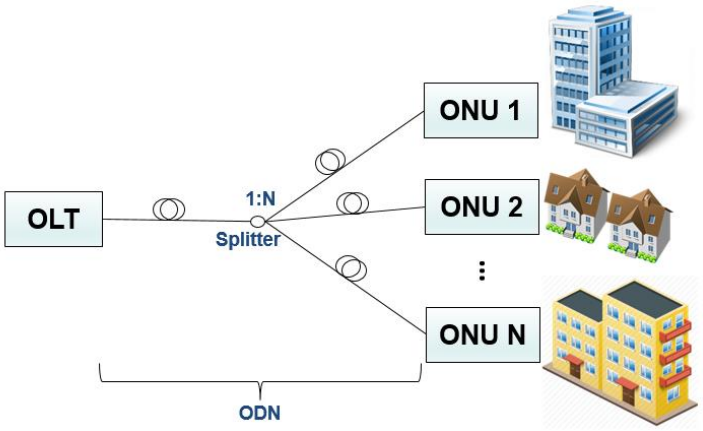

Fig. 2.1 Typical PON architecture

A typical PON system is shown in Fig. 2.1, which consists of an optical line terminal (OLT) at the service provider's central office (CO) and a number of optical network units (ONUs) near or at the end-users' premises. The section between OLT and ONUs is referred to as the optical distribution network (ODN). The PON architecture generally supports 32 ONUs for

example, with a covered transmission distance of usually 20 to 60km [2]. The architecture in Fig. 2.1 can support bidirectional transmission with downstream and upstream traffic decoupled by either separate fibres for each direction, or by employing different optical wavelengths. In the downstream direction, the OLT transmits data frames to all connected ONUs over a shared optical fibre network. In the upstream direction, the OLT schedules ONU transmissions to avoid collisions between ONUs.

PONs have a number of advantages over active optical networks (AON) including:

1) The elimination of active optoelectronic and electronic devices located in the remote node (RN) in the harsh outside environment. Thus low maintenance cost and better system performance stability are achieved.
2) Topological flexibility by placing the power splitter (PS) anywhere along the fibre link.
3) No power source is needed at the remote node, which is beneficial for both operator energy saving and global energy saving.

There are two traditional types of PONs: time division multiplexing-PON (TDM-PON), and wavelength division multiplexing-PON (WDM-PON). In addition, optical orthogonal frequency division multiplexing-PON (OOFDM-PON) has also been widely researched as a future PON candidate technology.

2.2.1.1 TDM-PON

Fig. 2.2 illustrates a typical TDM-PON system. The TDM-PON system uses different time slots to multiplex/demultiplex signal channels to/from different ONUs. Separate wavelength bands at 1490 nm and 1310 nm for example are utilized to carry downstream and upstream traffic, respectively. The downstream traffic is continuously broadcast to all ONUs, and each ONU selects the packets addressed to it and discards the packets addressed to other ONUs. In the upstream direction, each ONU transmits data only during the time slots that are allocated by the OLT [3]. Ranging procedures, based on the timed ONU response to OLT-range requests are typically used to determine the transmission delays in the upstream direction and subsequently adjust ONU timings to achieve upstream timeslot synchronisation.

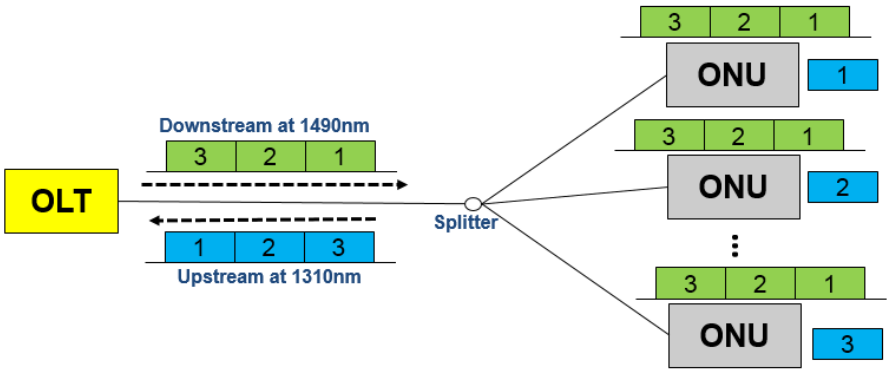

Fig. 2.2 A typical structure of a TDM-PON

2.2.1.2 WDM-PON

Fig. 2.3 shows a general WDM-PON [4] architecture. In the downstream direction, the OLT uses a mixed wavelength laser array or a Multi-Frequency Laser (MFL) to generate downstream signals, then the signals are individually modulated before being multiplexed with an Arrayed Waveguide Grating (AWG) to form a combined WDM signal. An AWG is also employed in the remote node to separate and route the individual wavelengths to different ONUs. In the upstream direction, each ONU uses an individual wavelength to carry its signal and these ONU signals are aggregated into a WDM signal by the AWG located at the remote node. The OLT receiver demultiplexes the received WDM signal using the OLT-base AWG and a photodetector array. It is noted that the synchronisation between ONUs is not required in the WDM-PON system.

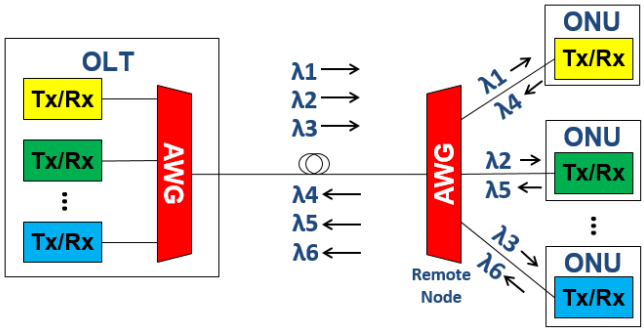

Fig. 2.3 A general WDM-PON architecture

In practice, a WDM-PON can also be combined with a TDM-PON to increase ONU count, transmission distance, system scalability and capacity. A hybrid TDM/WDM-PON (TWDM-PON) [5] is a PON in which more than one wavelength is used in each direction for communications between an OLT and a number of ONUs and each wavelength is shared among several ONUs by using the TDM technique. The TWDM-PON possesses a number of advantages from both WDM and TDM such as the ability to increase total PON capacity and to keep costs down by still sharing wavelengths between users. In addition, with the increased number of customers and transmission distance enabled by the TWDM PON, the number of COs can also be reduced leading to considerable power and maintenance cost savings.

WDM-PON is a "future-proof" solution to support the required bandwidth and scalability for NG-PONs due to the mature WDM technology. TWDM-PON has been selected as the base technology for NG-PON2 by the full service access network (FASN) group [5]. TWDM-PON provides better flexibility than pure WDM-PONs do, which allows delivery of services to more subscribers and the efficient use of the bandwidth of each wavelength.

2.2.1.3 OOFDM-PONs

An OOFDM-PON [6] is the combination of OFDM with TDM such that different OFDM subcarriers can be dynamically assigned to different customers/services in different TDM time slots. Fig. 2.4 shows a typical architecture and multiple access strategy of OOFDM-PON. For downstream traffic, different services such as ROF signals and Ethernet data share the same laser and downstream wavelength. The downstream signal is broadcast to all ONUs by using an optical splitter. Each ONU recovers its signal from its allocated subcarriers and timeslots. For upstream traffic, each ONU maps its data to its allocated subcarriers, sets all the other subcarriers to zero, and completes the modulation to generate electrical OFDM symbols. The electrical OOFDM signals are then converted to optical signals with low cost optical intensity modulators such as directly modulated lasers (DMLs) for transmission over the fibre. The OOFDM symbols from multiple ONUs will be combined at the optical coupler (OC) in the remote node, and detected by a single photodetector at the OLT receiver. To avoid collisions in the upstream, the OLT-managed accurate synchronisation of the OFDM symbols at the ONUs is essential.

Compared to conventional TDM-PON technologies, OOFDM PON has a number of salient advantages such as high spectral efficiency, high chromatic dispersion (CD) tolerance, excellent system scalability and fine granularity bandwidth control.

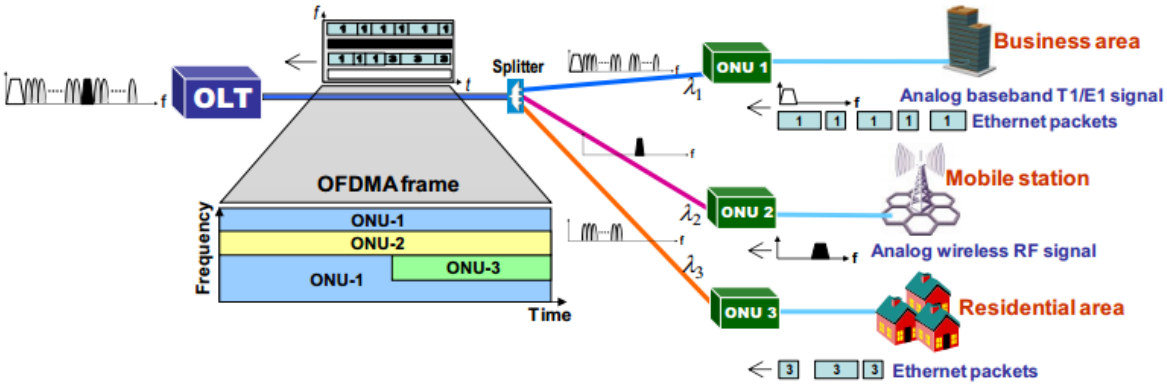

Fig. 2.4 A typical structure of an OOFDM-PON system ([12])

2.2.2 Current and Future PON standards

There are two standardisation bodies that have created PON standards, and standards from both bodies have enjoyed widespread implementation and deployment. The ITU-T develops standards for the GPON family, while the IEEE develops standards for the EPON family [7].

2.2.2.1 ITU-T APON/BPON and GPON

Asynchronous Transfer Mode (ATM) PON (APON) was started by FSAN/ITU-T and later transferred to ITU-T G983.1 standard in 1998. Broadband PON (BPON) is a higher speed version of APON and was specified in G983.3 in 2001 [8]. Both APON and BPON utilise TDM technology. In APON and BPON, both upstream and downstream frames are based on ATM cells. APON can provide signal line rates of 155Mb/s in both upstream and downstream over 20km, and BPON can support signal line rates of 155Mb/s upstream and 622Mb/s downstream over 20km.

In BPON standards, there are three classes of optical power budgets which are Class A (5 to 20dB), Class B (10 to 25dB) and Class C (15 to 30dB), which are specified in ITU-T G.982

[9]. Typical power split ratios are 1:32 or 1:64. The upstream uses the 1260-1360nm window and downstream uses the 1480-1500nm window.

G.984 GPON is an evolution of the BPON standard with an increased data rate [8]. The first version of G.984 GPON was ratified in 2003. It supports signal line rates of 2.488 Gb/s for downstream and 1.244 Gb/s for upstream [9]. GPON also support transmission distance of up to 60km and split ratios up to 1:128.

APON and BPON have now been widely replaced by GPON which is very broadly used worldwide today.

2.2.2.2 IEEE EPON

Ethernet PON (EPON) was standardized by the IEEE 802.3ah study group in 2004 [10]. EPON also employs TDM. It uses Ethernet protocol and provides bidirectional 1.25 Gb/s downstream and upstream signal bit rates over a reach of up to 20km by using the entire O-band (1260-1360nm) for upstream and 1480-1500nm for downstream and reserving 1550nm for future extensions or additional services such as analogue video broadcast [10].

In the IEEE 802.3ah EPON standard, the power budget is conservatively specified as 24 dB with a minimum 1:16 split ratio. In practice, the transceiver technology has matured enough so that components providing 29 dB power budget became commercially available, resulting in most EPON-based networks being deployed with a split ratio of 1:32, with some being as high as 1:64 [10].

EPON has been massively deployed in the Asia Pacific region. Japanese service providers, including NTT, USEN, K-Opticom, KDDI and others, have been ramping up on a truly massive scale with EPON beginning in late 2004.

2.2.2.3 10Gb/s NG-PONs

To meet the ever-increasing future bandwidth demand, 10G PON standards were developed which include ITU-T XG-PON and IEEE 10G-EPON [11]. XG-PON (G.987) was approved in 2010 while 10G-EPON (IEEE 802.3av) was approved in 2009. 10G PONs are also generally known as NG-PON1.

2.2.2.3.1 ITU-T XG-PON

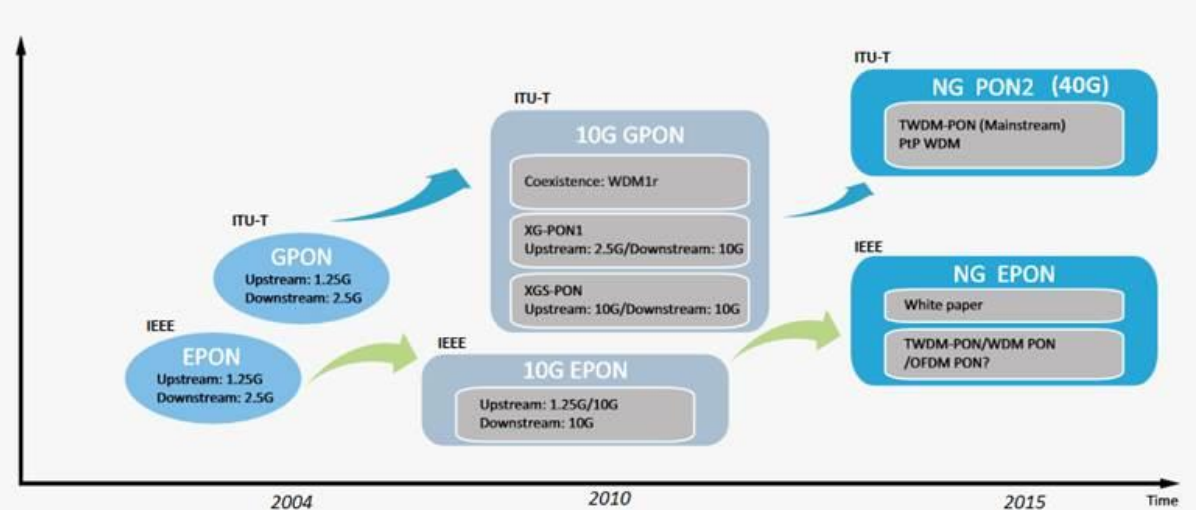

Fig. 2.5 NG-PON evolution roadmap from ITU-T [12]

Fig. 2.5 shows the evolution roadmap of ITU-T GPON. XG-PON is a smooth evolution of ITU-T G.984 GPON as XG-PON inherits all the requirements of GPON with a few new additions. ITU-T defined asymmetrical bit rates of 10Gb/s for downstream and 2.5Gb/s for upstream under the name of XG-PON, and symmetry bit rates of 10Gb/s for both downstream and upstream under the name of XGS-PON.

For XG-PON, the wavelength allocation plan is 1575-1580nm for downstream and 1260-1280nm for upstream. The power budget is 29-31 dB for a reach of at least 20km and split ratio of at least 1:64. For XGS-PON, it has already been standardised as G.9807.1.

2.2.2.3.2 IEEE 10G-EPON

10G-EPON is a smooth evolution of IEEE 802.3ah 1G-EPON. It was ratified as IEEE 802.3av standard in 2009. In Asia, 10G-EPON is mainly deployed for quad-wavelength or Tri-wavelength applications. In the US, the 10G-EPON is mainly preferred for dual wavelength symmetric applications. IEEE 802.3av defines two types of bit rates for 10G-EPON: symmetric bit rates of 10Gb/s for both downstream and upstream under the name of PR, and asymmetric bit rates of 10Gb/s for downstream and 1Gb/s for upstream under the name of PRX. The wavelength plans are 1575-1580nm for downstream and 1260-1280nm for upstream. There are three classes of optical power budget listed as follows:

- IEEE 802.3av-PR(X)10: 5-20dB power budget for 10km distance and split ratio of at least 1:16.
- IEEE 802.3av-PR(X)20: 10-24dB power budget for 20km distance and split ratio of 1:16.
- IEEE 802.3av-PR(X)30: 15-29dB power budget for 20km and split ratio of at least 1:32.

2.2.2.4 Beyond NG-PON1

ITU-T also offers the long-term plan beyond XG-PON/10G-EPON targeting even higher signal bit rates, which is referred to as NG-PON2 [12], as shown in Fig. 2.5. FSAN selected TWDM (4 wavelengths at 10Gbps each) for NG-PON2 in April 2012. TWDM-PON coexists with commercially deployed G-PON and XG-PON systems. However, NG-PON2 is not very cost effective as it is basically 4x 10GPON which requires 4 tunable lasers and corresponding tunable optical filters, meanwhile technologies such as OOFDM can potentially achieve 40Gb/s or more on a single wavelength [13-15] making it a more cost-effective PON technology due to the utilization of low-cost mass produced electronics for future PON generations such as NG-PON3. In addition, technologies for 100G-EPON (25-Gb/s per wavelength) are currently under consideration by the IEEE P802.3ca 100G-EPON Task Force. In order to reuse the optical components in XG-PON for cost-effectiveness, advanced modulation formats have been proposed to support 25-Gb/s data rate based on 10G-class optical devices, such as 4-level pulse amplitude modulation (PAM-4) [16] and OOFDM [17].

2.3 Advanced Modulation Formats

2.3.1 Introduction

Traditional optical modulation techniques such as on-off keying (OOK) and amplitude shift keying (ASK) are reaching the limit of their performance due to linear and nonlinear impairments in optical fibre communication systems. New advanced modulation techniques are therefore required in future networks to support both higher data rate transmission, by increasing spectral efficiency, and improved dynamic bandwidth allocation efficiency. The

need for advanced modulation techniques for CANs is explained in detail in section 2.5.2.1. As OFDM and CAP are modulation techniques utilised in this thesis, they are described in details in this section.

2.3.2 OFDM

OFDM was firstly proposed by R. W. Chang in 1966 [18] as a special case of Frequency Division Multiplexing (FDM) [19] and it has been widely used in wireless communications such as wireless local access networks (WLAN), wireless wide area networks (WWAN) [18] and fourth generation (4G) long-term evolution (LTE) [20] mobile networks as well as in wired networked such as digital subscriber line (DSL). A typical FDM system is shown in Fig. 2.6. In the transmitter, a serial bit stream is divided into parallel bit streams with lower bit rates and encoded using a classical modulation format such as M-ary quadrature amplitude modulation (QAM) [21]. Then simultaneously each of these data streams is modulated onto different subcarriers operating at different RF frequencies. There is a sufficiently wide inter-channel guardband between two adjacent subcarrier frequencies, which is illustrated in Fig. 2.7 (a). After that all the modulated different subcarriers are multiplexed for transmission in the channel. In the receiver, the parallel data streams are recovered by demodulating each of these subcarriers with an identical RF frequency, low pass filtered and finally decoded.

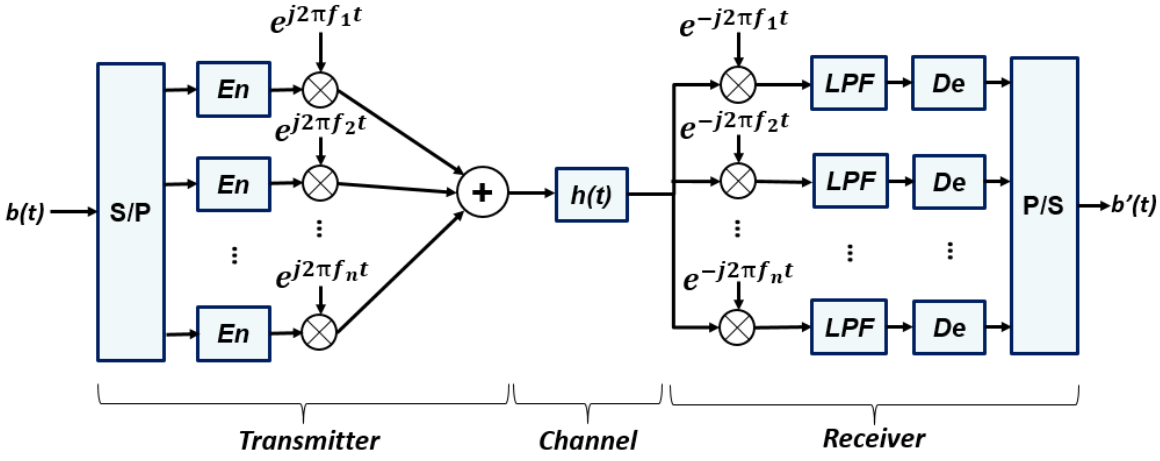

Fig. 2.6 Block diagram of a generic FDM system. S/P: Serial-to-Parallel, P/S: Parallel-to-Serial, LPF: Low-pass Filter, En: Encoder, De: Decoder.

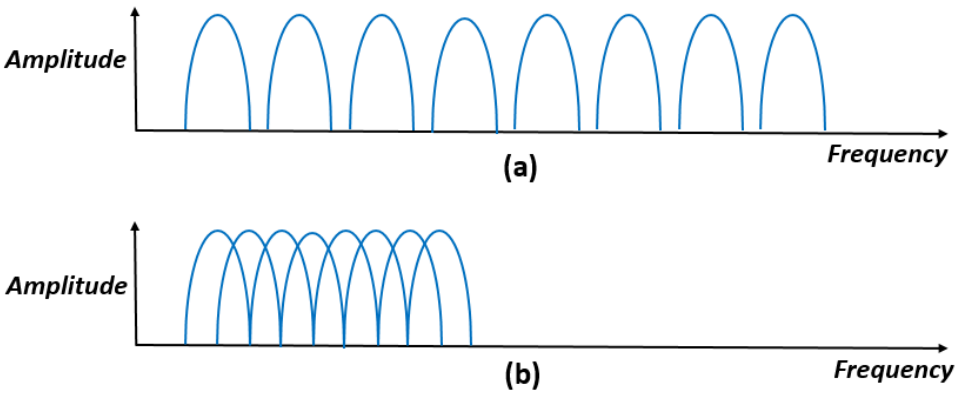

Fig. 2.7 Spectra of (a) FDM, (b) OFDM

Compared with FDM, OFDM precisely chooses the inter-subcarrier RF frequency spacing such that all RF frequencies are harmonically related and thus ensuring orthogonality between subcarriers. The orthogonality allows spectral overlap between subcarriers without interference and this results in significant enhancement in spectral efficiency (at least 50%) compared to FDM, as shown in Fig. 2.7 (b).

To explain the principle of orthogonality between OFDM subcarriers, the *k*-th subcarrier in the *n*-th OFDM symbol can be written as:

$$x_{k,n}(t) = X_{k,n} e^{j2\pi f_k t} p(\frac{t-nT}{T}) \tag{2.1}$$

where

$$X_{k,n} = A_{k,n} e^{j\theta_{k,n}} \tag{2.2}$$

$$p(\frac{t}{T}) = \begin{cases} 1, & 0 \le t \le T \\ 0, & otherwise \end{cases} \tag{2.3}$$

$A_{k,n}$ and $\theta_{k,n}$ are the amplitude and phase of the signal constellation points and $X_{k,n}$ is either user information or pilot signals. T is the time period of an OFDM symbol, f_k is the frequency of the *k*-th subcarrier which satisfies:

$$f_k = f_c + \frac{k}{T} \qquad k = -\frac{N}{2}, -\frac{N}{2}+1, \dots, 0, 1, 2, \dots, \frac{N}{2}-1 \tag{2.4}$$

where f_c is a frequency offset common to all subcarriers, generally set to zero. The correlation between any two subcarriers in the *n*-th OFDM symbol period is given by:

$$\frac{1}{T}\int_{(n-1)T}^{nT} x_{k,n}x_{l,n}^{*}\,dt = \frac{1}{T}\int_{(n-1)T}^{nT} X_{k,n}\,X_{l,n}^{*}e^{j2\pi(f_k-f_l)t} = \begin{cases} = 0, & k \neq l \\ \neq 0, & k = l \end{cases} \quad (2.5)$$

Eq. (3.5) indicates that the orthogonality is achieved among all the subcarriers. The orthogonality property means that when the OFDM symbol, which contains multiple subcarriers, is correlated with a single complex valued, reference subcarrier with a fixed frequency, only the subcarrier at the same frequency will contribute to a non-zero correlation output while other subcarriers at different frequencies will result in zero-valued correlation outputs. The correlation output thus reveals the amplitude and phase of the of the subcarrier at the correlated frequency. Therefore suitable correlation functions, such as a fast Fourier transform (FFT), can be performed in the receiver to recover the individual OFDM subcarriers.

2.3.3 Carrierless Amplitude Phase (CAP) modulation

CAP modulation is a bandwidth efficient multilevel and multidimensional modulation technique proposed by Bell Labs [22]. Fig 2.8 shows the schematic diagram of a transceiver system based on CAP modulation.

In the CAP transmitter, the original bit stream is first fed to an encoder which maps blocks of bits into complex symbols $A_n = a_n + jb_n$. The encoded data is up-sampled by a factor of *M*, i.e. *M*-1 zeros are inserted between two consecutive symbols. After the up-sampling, the in-phase and quadrature components of the symbols are separately fed to different digital shaping filters. The outputs of the filters are added and the result is passed through a DAC. The digital shaping filters and DAC operate at a sampling rate of $\frac{M}{T}$, where *T* is the original symbol period before up-sampling. The output signal of the CAP transmitter can be written as:

$$q(t) = \sum_{n=-\infty}^{\infty}[a_{up\_n} \otimes s_1(t) \mp b_{up\_n} \otimes s_2(t)] \quad (2.6)$$

where a_{up_n} and b_{up_n} are the up-sampled a_n and b_n which are discrete multilevel symbols of the in-phase and quadrature components respectively, and $s_1(t)$ and $s_2(t)$ are the impulse response of in-phase and quadrature shaping filters, respectively. $\otimes$ denotes convolution. A key property of CAP modulation is that the frequency responses of $s_1(t)$ and $s_2(t)$ have the

same amplitude characteristics but the phase characteristics differ by π/2 so that the shaping filters form a Hilbert pair [23].

In the CAP receiver, the received digital signal after an ADC is fed into two different digital matching filters to separate the in-phase and quadrature components. The ADC and matching filters operate at the same sampling rate as used in the transmitter. With an ideal transmission channel, the output signals of the two matching filters can be expressed as:

$$r_1(t) = q(t) \otimes m_1(t) = [\sum_{n=-\infty}^{\infty}\left[a_{up\_n} \otimes s_1(t) \mp b_{up\_n} \otimes s_2(t)\right]] \otimes m_1(t) \quad (2.7)$$

$$r_2(t) = q(t) \otimes m_2(t) = [\sum_{n=-\infty}^{\infty}\left[a_{up\_n} \otimes s_1(t) \mp b_{up\_n} \otimes s_2(t)\right]] \otimes m_2(t) \quad (2.8)$$

Here $m_1(t) = s_1(-t)$ and $m_2(t) = s_2(-t)$ [19] are the impulse response of the corresponding matching filters with

$$s_i(t) \otimes m_j(t) = \begin{cases} \delta(t - t_0) & i = j \\ 0 & i \neq j \end{cases} \quad (2.9)$$

where t_0 is the total discrete time delay of the filters. Using Eq. 2.9, Eq. 2.7 and Eq. 2.8 can be rewritten as:

$$r_1(t) = \sum_{n=-\infty}^{\infty} a_{up\_n} \otimes \delta(t - t_0) \quad (2.10)$$

$$r_2(t) = \sum_{n=-\infty}^{\infty} b_{up\_n} \otimes \delta(t - t_0) \quad (2.11)$$

After the matching filter, the signal is down-sampled by a factor of *M* and equalization is employed for the combined complex signal to account for the effects of the channel and finally decoding is utilized to recover the original bit stream.

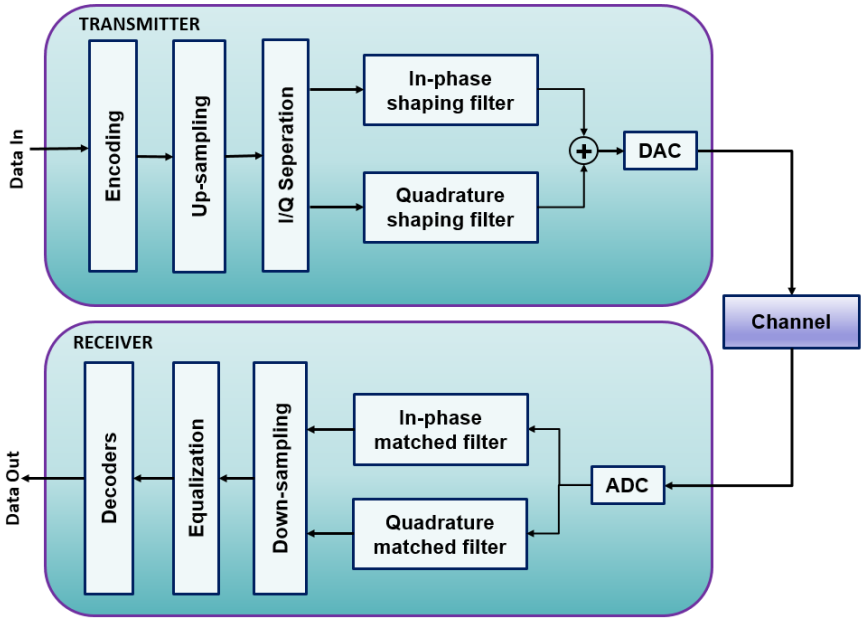

Fig. 2.8 Schematic diagram of transceivers based on CAP modulation

Here it is worth giving a comparison between CAP and the proposed digital orthogonal filtering in section 3.2. Both CAP and the digital orthogonal filtering employ filters to achieve carrier I/Q modulation without using any mixers. However the major difference is that in CAP the I and Q signals are discrete multi-level digital values which result in fixed constellation points for each combination of I and Q levels (e.g. if I and Q have two levels the carrier has four constellation points), whereas in the digital orthogonal filtering case each of the I and Q inputs are arbitrary analogue signals which could use any arbitrary modulation format.

2.4 SDN Fundamentals

2.4.1 Limitations of Current Networking Technologies

Fig. 2.9 illustrates a traditional network architecture. As seen in Fig. 2.9, traditional networks consist of multiple interconnected nodes (routers and switches) and many different distributed communication protocols are running between different nodes. Current traditional networks are finding it challenging to meet the requirements of today's users, enterprises and carriers as they have limitations listed as follows [24]:

- Excess complexity and cost. Network technologies to date consists largely of discrete sets of protocols designed to connect hosts reliably over arbitrary distances, link speed and topologies. Protocols defined in isolation result in high complexity and high cost. Multiple switches, routers, firewalls, web authentication protocols, VLANs, QoS, and other protocol-based mechanisms using network device-level management tools must be configured and updated when adding more network devices.
- Inability to scale. Current networks become vastly more complex with the addition of thousands of network devices that need to be configured and managed. In addition, in today's virtualized data centres, traffic patterns are incredibly dynamic and therefore unpredictable. Network operators face daunting scalability challenges. They need hyperscale networks that can provide high-performance, low-cost connectivity among potentially millions of physical servers and end-user devices. However, such scaling cannot be done efficiently with traditional network configuration tools.
- Vendor dependence. Carriers and enterprises seek to deploy new capabilities and services in rapid response to changing business needs or user demands. However, their ability to respond is hindered by vendors' equipment product cycles, which can be typically three years or more. Also the lack of unified network management standards and open interfaces limits the ability of network operators to easily tailor the network to their individual requirements.
- Limited network virtualisation. Future networks must support network virtualisation to provide independent virtual networks that share the same physical infrastructure. The virtual networks are then customised to meet the specific needs of applications, services, devices and customers, thus tailoring the guaranteed levels of service, such as capacity, latency and security, for each virtual network. This is not possible to achieve at the physical layer in traditional networks and so the virtual networks in traditional networks cannot be fully decoupled and independent. To provide truly independent virtual networks on the same network infrastructure, network virtualisation at the physical layer must be supported in future networks which must also provide dynamic reconfiguration to efficiently utilise the physical network resources.

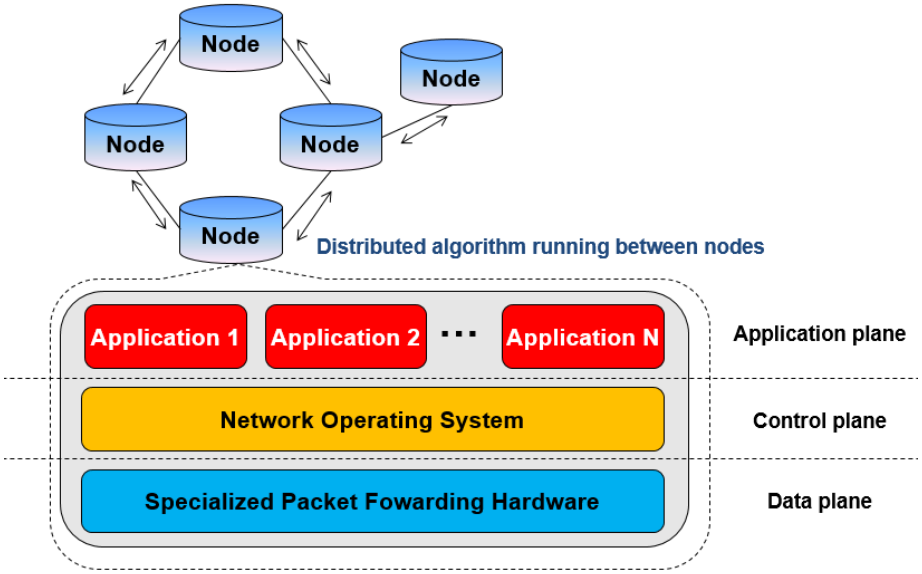

Fig. 2.9 Traditional network architecture

2.4.2 History of SDN

The concept of SDN was first proposed by Dr Martin Casado from Stanford University [25], which initially targeted improving security in Ethernet-based enterprise networks. Specifically, it was noted that because source-to-address and address-to-principle bindings are loose and insecure in today's networks, policy declarations need to be made over low-level identifiers that don't have clear mappings to network principles and are topology dependent. Such hard-wiring of topology into security policy then inevitably requires manual intervention, which complicates network operation, slows down network evolution, and does not fully address security loopholes. One of the first SDN projects was AT&T's GeoPlex [26]. AT&T Labs Geoplex project members Michah Lerner, George Vanecek, Nino Vidovic, and Dado Vrsalovic leveraged the network application programme interfaces (APIs) and dynamic aspects of the Java language as a means to implement middleware networks. SDN has changed the way we design and manage networks. SDN has two defining characteristics: i) SDN separates the control plane (which decides how to handle the traffic) from the data plane (which forwards traffic according to decisions that the control plane makes). ii) SDN consolidates the control plane so that a single software program controls multiple data-plane elements. The SDN control plane performs direct control over the networks' data-plane elements (i.e., routers and switches) via a well-defined API such as OpenFlow.

2.4.3 SDN Architecture

Fig. 2.10 depicts the basic SDN architecture, where the network control is decoupled from the forwarding and is directly programmable. The SDN architecture comprises three layers [27], known as the Data plane, Controller plane and Application plane:

- The data plane comprises network elements, which expose their capabilities toward the control plane via the data-controller plane interface (D-CPI).
- In the Controller Plane, the SDN controller translates the applications' requirements and exerts more granular control over the network elements, while providing relevant information up to the SDN applications. Services are offered to applications via the application-controller plane interface (A-CPI, often called northbound interface (NBI) by way of an information model instance that is derived from the underlying resources, management-installed policy, and local or externally available support functions. An SDN controller may orchestrate competing application demands for limited network resources.
- SDN applications reside in the Application Plane, and communicate their network requirements toward the Controller Plane via the A-CPI.
- The management/operating support systems (OSS) provides policy-based configuration and management at each of the SDN layers, sets the relatively static operational parameters within which the SDN controller and SDN applications are able to operate.

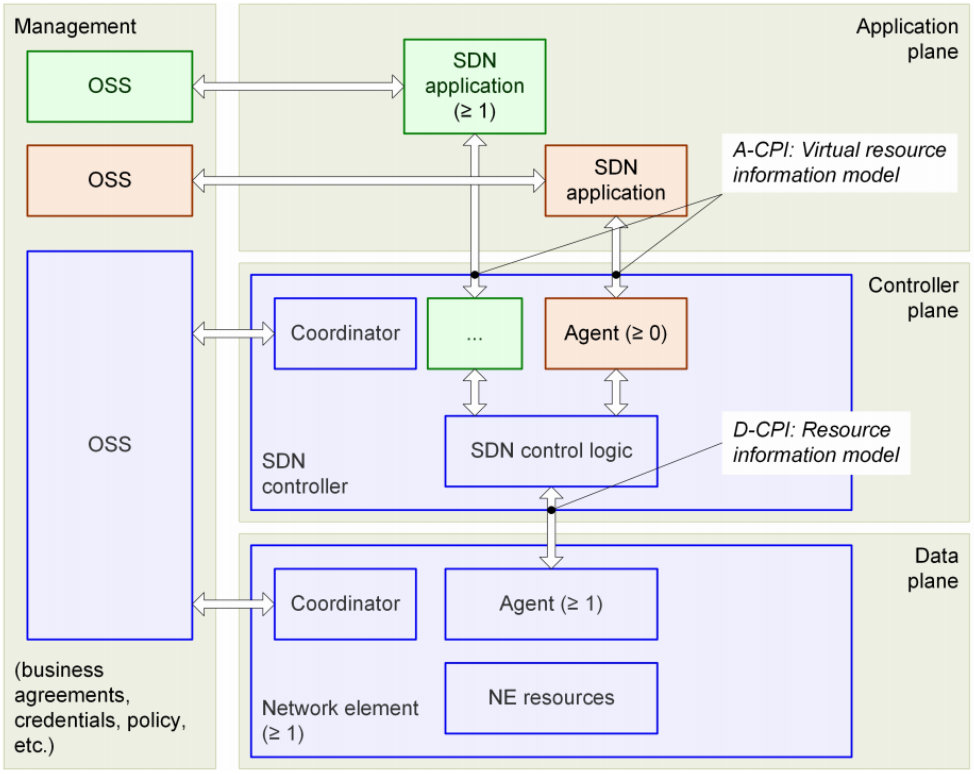

Fig. 2.10 SDN architecture overview ([27])

The SDN architecture has a number of salient advantages including [27]:

- Reduced complexity through automation. This migration of control enables the underlying infrastructure to be abstracted for applications and network services, which can treat the network as a logical or virtual entity. The SDN controller maintains a global view of the network. This not only greatly simplifies the network design and operation but also simplifies the network devices as there is no need of understanding and processing thousands of protocol standards but merely accept instructions from the SDN controller.
- Higher rate of innovation. SDN accelerates business innovation by allowing network operators to literally program the network in real time to meet specific business needs and user requirements as they arise. SDN gives network operators and potentially even end-users the ability to tailor the behaviour of the network and introduce new services and network capabilities in a matter of hours.
- Increased network security and reliability. SDN allows network operators to define high-level configuration and policy statements. It eliminates the need to individually configure network devices each time an end point, service, or

application is added or moved, or a policy changes, which reduces the likelihood of network failures due to configuration or policy inconsistencies.

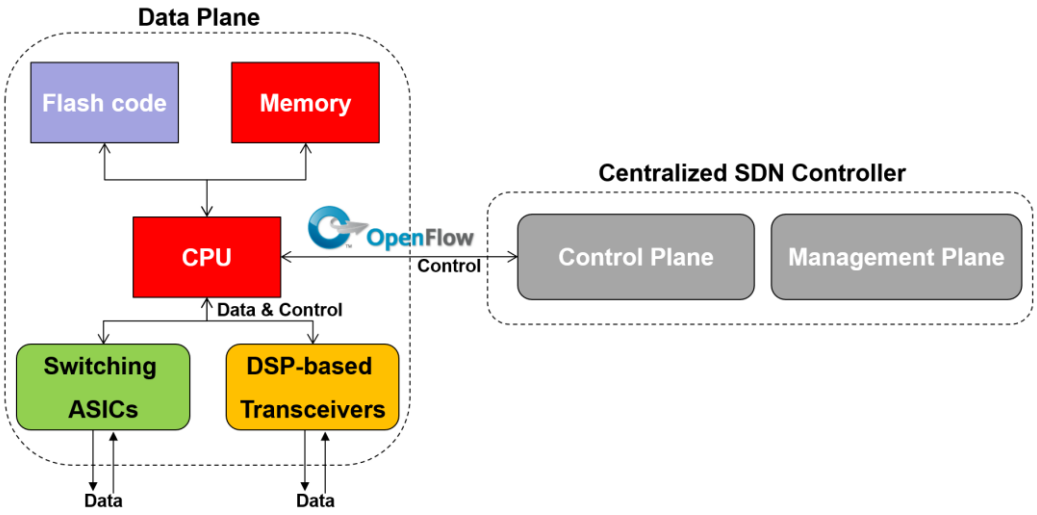

Fig. 2.11 Synergy between SDN and DSP-based transceivers

It should be noted, as shown in Fig. 2.11, that, from the data plane point of view, SDN has unique synergy with DSP-based reconfigurable optical transceivers [28] presented in this thesis, as not only do the transceivers enable network flexibility, but also the SDN provides a highly effective means of dynamically controlling the transceivers' reconfigurability and thus maximising its effectiveness. DSP-based adaptive reconfigurable optical transceivers can enable software defined optical transmission in the physical layer according to the traffic demand, channel condition and selected path, for an efficient assignment of the network recourses [29]. By using DSP-based reconfigurable optical transceivers, the system can dynamically adapt to transmission and component impairments of a selected network path, and be flexibly reconfigured according to the requested data rate and performance.

2.4.4 OpenFlow

OpenFlow is the first standard communications interface protocol defined between the control and data layers of an SDN architecture [24]. OpenFlow allows direct access to and manipulation of the data plane of network devices such as switches and routers, both physically and virtually (hypervisor-based). It is the absence of an open interface to the data plane that has led to the characterization of today's networking devices as monolithic, closed, and mainframe-like. No other standard protocol does what OpenFlow does, and a protocol

like OpenFlow is needed to move network control out of the networking devices to logically centralized control software.

As shown in Figure 2.12, the OpenFlow protocol specifies basic primitives that can be used by an external software application to program the data plane of network devices, just like the instruction set of a CPU would program a computer system.

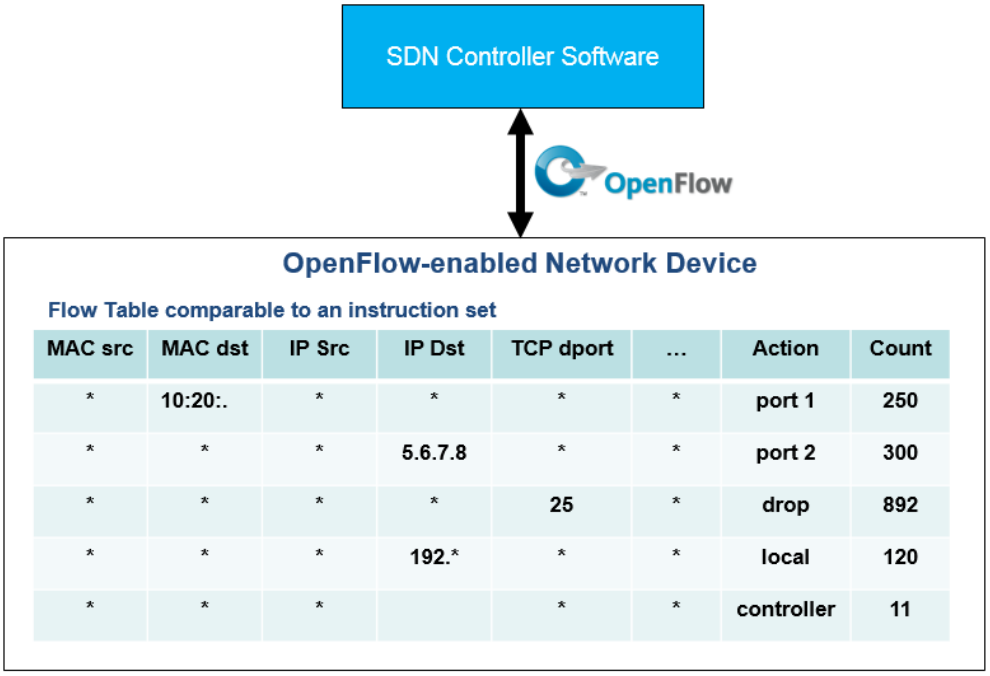

Fig. 2.12 Example of OpenFlow Instruction Set

The OpenFlow protocol is implemented on both sides of the interface between network infrastructure devices and the SDN control software. OpenFlow uses the concept of flows to identify network traffic based on pre-defined match rules that can be statically or dynamically programmed by the SDN control software. It also allows network operators to define how traffic should flow through network devices based on parameters such as usage patterns, applications and cloud resources. Since OpenFlow allows the network to be programmed on a per-flow basis, an OpenFlow-based SDN architecture provides extremely granular control, enabling the network to respond to real-time changes at the application, user, and session levels. Current IP-based routing does not provide this level of control, regardless of their different requirements. The OpenFlow protocol is a key enabler for software-defined networks and currently is the only standardized SDN protocol that allows direct manipulation of the data plane of network devices. While initially applied to Ethernet-

based networks, OpenFlow switching can extend to a much broader set of use cases. OpenFlow-based SDNs can be deployed on existing networks, both physical and virtual. Network devices can support OpenFlow-based data as well as traditional data, which makes it very easy for enterprises and carriers to progressively introduce OpenFlow-based SDN technologies, even in multi-vendor network environments.

For the interest of the thesis, it can be comprehended that OpenFlow would need to be extended so it could support the control and management of the physical layer aspects associated with the reconfigurable optical network elements. Therefore, the network device's local software functionality, as illustrated in Fig. 2.11, can support an embedded DSP controller function which handles the low-layer DSP parameters determined by the high-layer OpenFlow commands.

2.5 Requirements for Future Cloud Access Networks

2.5.1 CAN Architecture

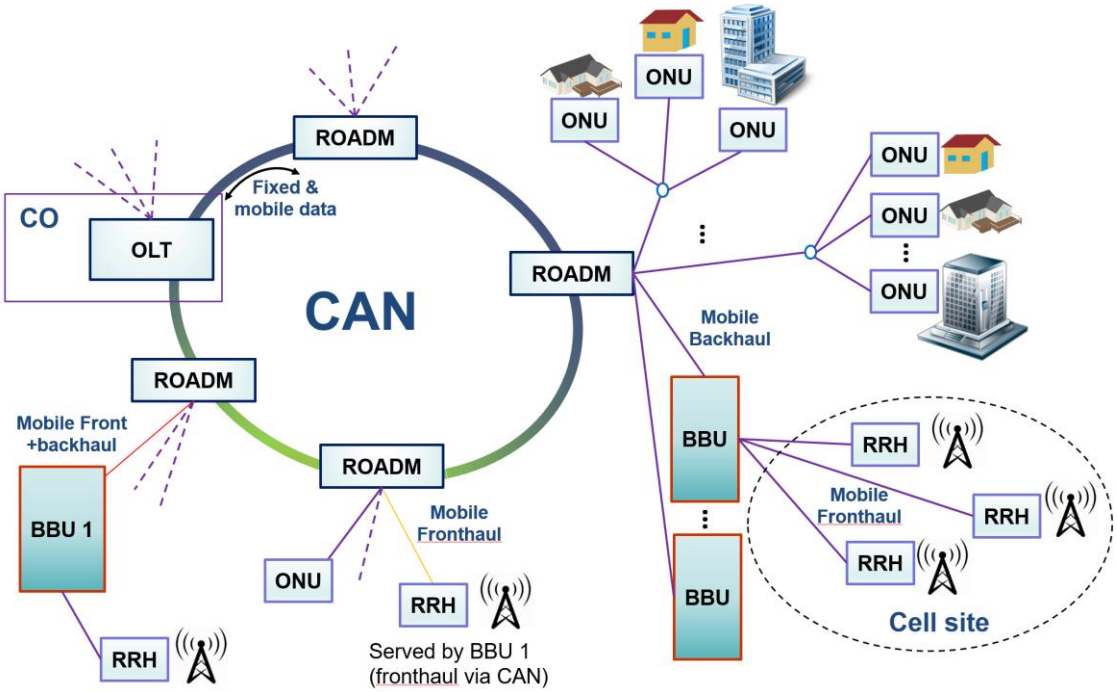

Fig. 2.13 CAN architecture

As described in the previous chapter, CANs seamlessly integrate traditional optical access networks, metro optical networks and mobile fronthaul/backhaul networks. In this section, an example of a CAN architecture is given, as seen in Fig. 2.13.

In a CAN carrying fixed, mobile backhaul and mobile fronthaul data, multiple ROADMs are interconnected in a ring. Each ROADM can 1) feed one or more PONs; 2) provide mobile backhaul links to BBUs, and 3) connect BBUs and RRHs located at different locations with the fronthaul connected via the CAN.

2.5.2 Future Requirements for CANs

2.5.2.1 Advanced Modulation Techniques

OOK [30] has been the modulation format extensively used in optical fibre communications for decades due to its various advantages such as cost-effective transceiver structure and robustness against noise and nonlinear impairments. However, as the data rate increases, distortion such as chromatic dispersion-induced inter-symbol interference (ISI) arises [30]. On the other hand, there is stringent requirements for bandwidth of the available optical and electrical components. As a result, OOK is reaching the limit of its performance [31]. Therefore, advanced modulation formats [32] are needed to achieve spectrally efficient high-speed optical networks to support future CANs.

In addition to OFDM and CAP described in section 2.3, some other examples of advanced modulation formats that have been researched extensively include QAM, PAM and subcarrier index-power modulated OOFDM (SIPM-OOFDM).

QAM [33] is a modulation technique widely used for digital transmission in both wireless and wired applications ranging from cellular to digital video broadcasting (DVB). QAM employs a single carrier frequency in which both amplitude and phase are modulated so it is able to carry a higher data rate than a traditional amplitude or phase modulation scheme. The constellation diagram shows the combinations of carrier amplitude and phase for different QAM symbols, the level of the QAM is indicated by the number of constellation points. Example QAM constellations are shown in Fig. 2.14. The constellation points are normally arranged in a square grid with equal vertical and horizontal spacing to maximise tolerance to noise. Using a higher level of QAM means more points on the constellation, thus more

bits can be transmitted per symbol, however, for a fixed peak signal power, the constellation points are now closer together so there is now less resilience to noise and distortion.

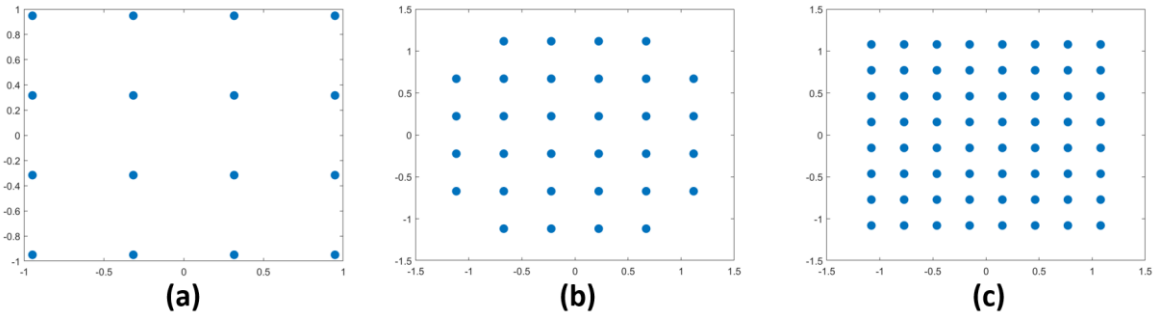

Fig. 2.14 Example constellation diagrams. (a) 16-QAM, (b) 32-QAM, (c) 64-QAM

PAM is a modulation format where multiple information bits are encoded in the amplitude of a series of signal pulses. Among different PAM schemes using different number of discrete pulse amplitudes, the most promising one is 4-level PAM known as PAM-4 [34], as seen in Fig. 2.15. From the time domain perspective, PAM-4 has advantage over traditional non-return-to-zero (NRZ) in that for each symbol there are 2 bits of information thus providing twice as much capacity for the same symbol rate. From the frequency domain perspective, PAM-4 also requires only half the bandwidth of that of NRZ for a fixed bit rate, allowing a lower sampling rate at the receiver. In addition, PAM-4 also has increased bit rate compared to NRZ with the same symbol rate at the cost of reduced tolerance to channel impairments which however can be compensated by making use of advanced equalisation techniques. Recently 56Gb/s PAM-4 transmission over 20km SSMF has been reported [35].

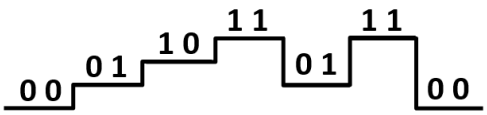

Fig. 2.15 Example of PAM-4 signal

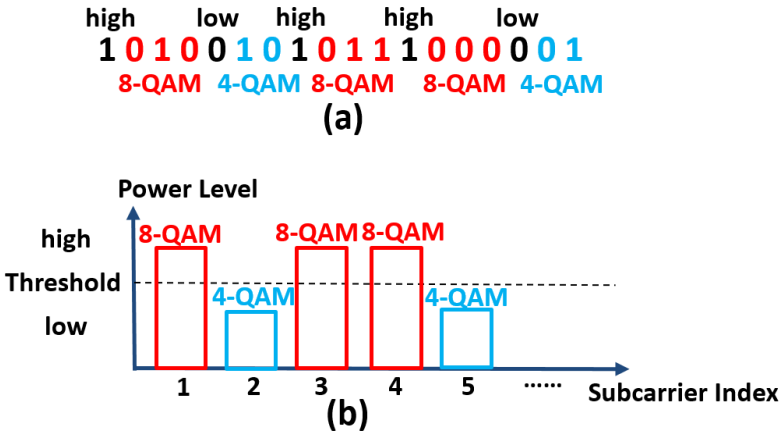

Fig. 2.16 Example of SIPM-OOFDM (a) data encoding process, (b) Schematic diagram showing how a subcarrier of a specific power level is encoded in the transmitter using 4-QAM and 8-QAM

SIPM-OOFDM is another novel modulation technique proposed and exploited in [36] for use in cost-sensitive IMDD PON systems. In SIPM-OOFDM, the combined subcarrier index and subcarrier power acts as an extra information-carrying dimension, i.e. a specific subcarrier is set at a low or high power according to an incoming data sequence. As shown in Fig. 2.16 (a), when a "1(0)" bit is encountered, the corresponding subcarrier power is set high (low) as illustrated in Fig. 2.16 (b), and the following 3(2) bits of the data sequence are then encoded using 8-QAM (4-QAM). Setting each individual subcarrier at a specific power level enables not only the subcarrier to carry an extra information bit but also permits all the subcarriers to be active all the time. In addition, a training sequence-based subcarrier power level decision threshold is also determined in the receiver to recover the information conveyed in the extra dimension without complicated transceiver negotiations. Compared to conventional OOFDM, SIPM-OOFDM offers considerable signal transmission capacity improvement without degrading system power budget and dispersion/nonlinearity tolerances [36]. Recently significantly enhanced variants of SIPM-OOFDM including multilevel-SIPM-OOFDM (ML-SIPM-OOFDM) [37] and SIPM-OOFDM with superposition multiplexing (SIPM-OOFDM-SPM) [38] have been proposed to further improve the transmission performance.

2.5.2.2 Reconfigurable Optical Transceivers

In order to support future CANs to offer on-demand heterogeneous mobile and fixed connectivity, from the physical layer perspective, reconfigurable optical transceivers play a vital role in enabling a software defined optical transmission to flexibly assign available network resources according to transient traffic demand and channel condition. By means of DSP, reconfigurable optical transceivers incorporating various advanced modulation formats can be dynamically configured to handle programmable network parameters/attributes including data rate, required BER performance, spectral occupancy and bandwidth of signal, modulation format, wavelength etc. [39, 40]. In addition, reconfigurable optical transceivers are also envisaged to be managed by the control plane in the SDN scenario [41]. As an example, a sliceable bandwidth variable transceiver (S-BVT) adopting multicarrier modulation (OFDM or discrete multitoned modulation (DMT)) was recently proposed for metro/regional elastic networks and data centre applications [42]. In such S-BVT, after the OFDM/DMT adaptive DSP modules, an array of tunable laser sources (TLS) and Mach-Zehnder modulators are used in the transmitter front-end to generate multiple flows which are then aggregated by a spectrum selective switch (SSS). The aggregated flow can be sliced to serve multiple destination nodes at variable rate and bandwidth. Another example is the Ethernet to elastic optical network (E-EON) interface with reconfigurable superchannel (SC) transmitters [43]. In [43] the E-EON interface implemented using FPGA-based optoelectronics can aggregate several 10GbE data to SC signals which can be reconfigured in modulation format, symbol rate or subcarrier numbers, managed and controlled by open-flow SDN to satisfy flexible bandwidth request according to the total capacity requirement and transmission link conditions. However, to provide high flexibility, adaptability and scalability in a cost-effective manner required by future CANs, the transceiver should also support SDN-controllable multiplexing of multiple dynamic physical channels without using expensive optical switching and filtering components. Such a transceiver is one of the key contributions of this thesis and will be described in detail in the Chapter 3.

2.5.2.3 PON Technologies

As discussed in the last chapter, CANs integrate optical access networks with mobile networks to provide heterogeneous services to end-users. Since PONs are being extensively deployed worldwide and are considered to be the most favourable future optical access

network due to its cost effectiveness and its inherent future-proof characteristics, CANs should fully exploit the advantages of PON technologies. However CANs also introduce new key requirements for consideration when designing future PON technologies as follows:

- High network transparency to underlying signal modulation format, signal detection scheme, WDM grid, arbitrary bandwidth granularity and network topology.
- Improved network operation reconfigurability with extended SDN functionality to the physical layer.
- Provision of multiplexing of multiple physical channels which enables the dynamic configuration of multiple virtual networks on the same fiber infrastructure.
- Compatibility with low cost flexible ROADMs which are capable of performing add/drop functions at subwavelength levels.

2.5.2.4 ROADMs

Recently a number of ROADMs with various advanced architectures have been reported as detailed in section 2.7. However, these ROADMs only work at the wavelength level, and they are also expensive and bulky for the converged metro/access networks due to the utilisation of hard-wired switching elements, which significantly limits the ROADM's flexibility, upgradability, as well as its adaptability and cost-effectiveness. To meet the challenging requirements of CANs, it is easy to comprehend that it is critical that ROADMs should be equipped with new features as listed below:

- Optical-electrical-optical (O-E-O) conversion free.
- SDN controllable ROADM configurations.
- Highly flexible and tunable add/drop operations at wavelength, subwavelength and orthogonal sub-band levels.
- Low cost and low energy consumption.
- Small footprint.

2.6 DSP-based Optical Transceiver

As previously stated, flexible optical transceivers are key building blocks for software-defined CANs as they provide software-programmable properties such as transmission

schemes, advanced modulation formats, data rates, signal bandwidths and forward-error correction (FEC) protocols to be configured dynamically, thus enabling full optimization and utilization of network resources. Hardware-based DSP algorithms provide a highly powerful and cost-effective technology for implementing flexible optical transceivers with the aforementioned properties [42-45]. Modern digital integrated circuits can achieve the ultra-high processing speeds needed for high capacity transceivers and continuous developments in digital chip densities means the cost and power per DSP function is steadily decreasing with time, similarly the complexity of signal processing algorithms that can be implemented via DSP is also progressively increasing over time. Also, as optical transceivers are high volume products, low costs are achieved by leveraging the economies of scale associated with mass produced integrated circuits. Clear evidence of the advanced capabilities of DSP technology is the highly successful deployment of DSP-enabled coherent optical transceivers in long-haul applications, where DSP is used to implement highly powerful and sophisticated algorithms required for coherent optical signal detection.

In addition to providing the aforementioned reconfigurable transceiver properties, DSP algorithms can be utilised to provide functions such as linear (CD [46] and polarisation mode dispersion (PMD) [47]) and nonlinear [48, 49] compensation, interference cancellation [50, 51] and increased energy efficiency [52, 53].

This section discusses the basic structure and key elements of a DSP-based optical transceiver and explains in detail the implementation of an optical OFDM transceiver.

2.6.1 Transceiver Structure and Key Elements

The general structure of a DSP-based optical transceiver [54] is illustrated in Fig. 2.17. The key elements in the transmitter are: high speed digital logic for hardware-based DSP, high speed digital-to-analogue converter (DAC) to convert digital samples to analogue electrical signal, a wideband radio frequency (RF) section to amplify, filter and possibly up-convert the signal onto an RF carrier, and an electrical-to-optical (EO) converter that converts the analogue electrical signal into an optical signal. The key elements in the receiver are: an optical-to-electrical (OE) converter to detect the optical signal and convert to an electrical signal, a wideband RF section to filter, amplify and possibly down-convert the signal, and a high speed analogue-to-digital converter (ADC) to convert the analogue electrical signal to digital samples and finally the high speed digital logic for signal processing.

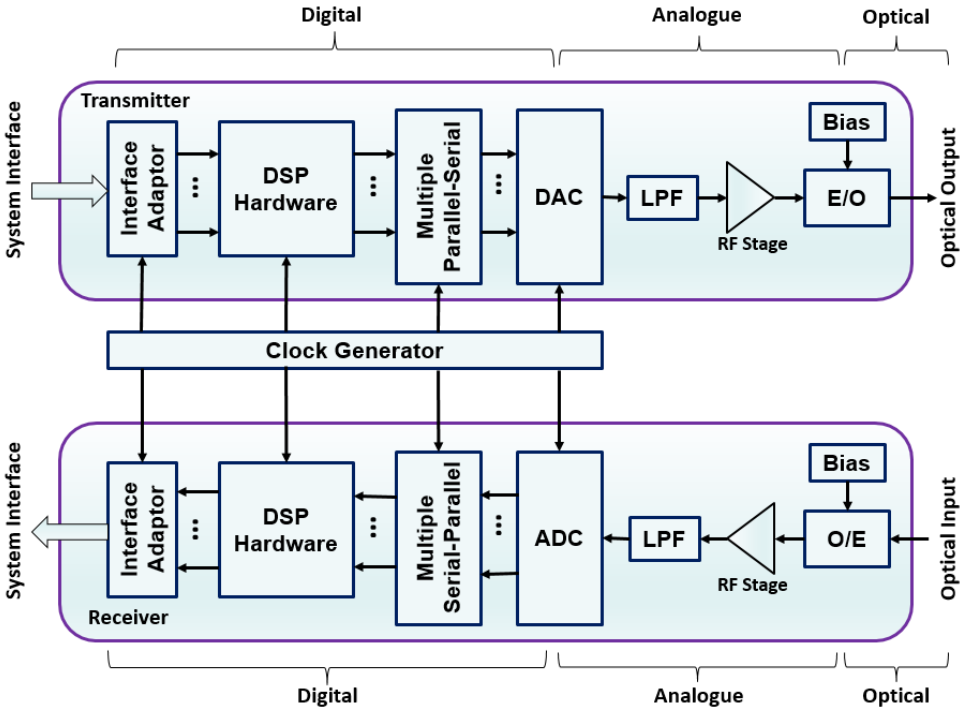

Fig. 2.17 System elements of DSP-based optical transceivers. E/O: electrical to optical converter, O/E: optical to electrical converter, LPF: low pass filter.

The DSP functions must be implemented in digital hardware due to the ultra-high processing speeds necessary to support the multi-Gb/s optical signals. As the digital hardware operates at clock speeds of several 100 MHz the use of parallel processing techniques can be fully exploited to easily achieve sufficient processing throughput. For prototyping real-time DSP hardware, field programmable gate arrays (FPGAs) [55] offer the ideal solution due to their re-programmability. This enables rapid evaluation and optimization of the hardware-based algorithms. The high cost and power consumption of FPGAs, however, makes them inappropriate for the cost and power sensitive PON applications. Therefore, it is necessary to employ custom designed application specific integrated circuits (ASICs) [56] for real-time DSP in commercial products. ASICs obviously require significant capital investment for development but reap the benefits of low costs associated with high volume mass production of integrated circuits. ASICs also offer the advantage of significant power reduction compared to FPGAs. The DAC and ADC are highly critical components in the transceiver and will be discussed in more detail in the next section.

The RF section performance can also have a big impact on the transceiver performance. RF components must have characteristics such as high linearity (as the modulated signal is analogue), low noise figure, flat frequency response, wide bandwidth, high return loss and

automatic gain control in the receiver. The ultra-wide bandwidth of optical systems can be challenging for the RF components (near DC to several 10s GHz) as they must have good performance over a very wide band compared to radio systems where the operating bandwidth can be relatively small (few MHz) compared to the carrier frequency.

For optical front ends, IMDD [57] is highly preferred due to the cost-sensitive nature of the optical access networks. IMDD operates by either direct modulation or external modulation of a laser source. Directly modulated lasers (DML) offer the lowest cost solution. However, DMLs suffer from the phenomenon of frequency chirp [58] which can degrade transceiver performance compared with the almost chirp-free external modulation scheme. For direct detection, a photodiode or avalanche photodiode is employed which is a so-called square-law detector as the electrical current generated is proportional to the square of the optical field and therefore the optical signal intensity. The photodiode is followed by a transimpedance amplifier to convert the detected current to a voltage for the following RF section. For low cost IMDD optics, the vertical cavity surface emitting laser (VCSEL) [59] is a highly promising laser source as these lasers can be produced at extremely low cost mainly due to the reduced manufacturing process costs. Although VSCELs have lower performance and lower bandwidth compared to more expensive lasers, such as DFBs, the DSP can be utilised in the transceivers to compensate for the VCSELs' limitations [60].

2.6.2 DACs and ADCs

The DAC and ADC are highly critical components in DSP-based optical transceivers. DACs convert the digital domain signals to the analogue domain for subsequent E/O conversion, whilst the ADCs convert the received analogue signals after the O/E conversion back to the digital domain. As a consequence, the required DAC/ADC basic characteristics are: high sample rates to support the 10s Gb/s bit rates, bit resolutions in the region of 8 bits (modulation format dependent), high linearity and low noise. DAC/ADC aspects that can have impact on transceiver performance include: quantization noise due to the discrete signal levels, non-ideal linear behaviour which causes the effective number of bits (ENOB) to be lower than the physical resolution, and the ENOB decreasing with signal frequency. The full-scale range of the DAC/ADC should be utilized to minimize the effect of quantization noise, which can necessitate automatic gain control (AGC) before the ADC. DACs also typically have a characteristic roll-off in frequency response due to the inherent sin(x)/x

shaping due to the zero-order-hold output format, as well as low pass filtering effects of the on-chip analogue front end. Furthermore, the sampling clock quality can affect performance due to clock jitter and frequency offset. It should be emphasized here that DSP algorithms can be exploited to mitigate some of the non-ideal DAC/ADC properties and/or relax the required DAC/ADC performance requirements. The required DAC/ADC sampling rate for a given line rate of R (bits/s) is dependent on the electrical spectral efficiency E (b/s/Hz) of the adopted modulation format. The required signal bandwidth is B = R/E (Hz). Therefore assuming operation over the entire Nyquist band and single-band transmission, the required sampling rate is S = 2·B = 2·(R/E) (samples/s). For example, if the sampling rate is limited to 20 GS/s, a 40 Gb/s line rate would require a modulation format with at least 4 b/s/Hz spectral efficiency. Modulation formats with high spectral efficiency are thus important to minimize DAC/ADC sample rates. Fig. 2.18 shows the bit resolution and sample rates of some commercial high speed DACs and ADCs currently available. The trend in DAC/ADC sampling rates has shown a steady growth [54] and developments are generally led by the progress in high-end test equipment such as digital sampling oscilloscopes (for ADCs) and arbitrary waveform generators (for DACs).

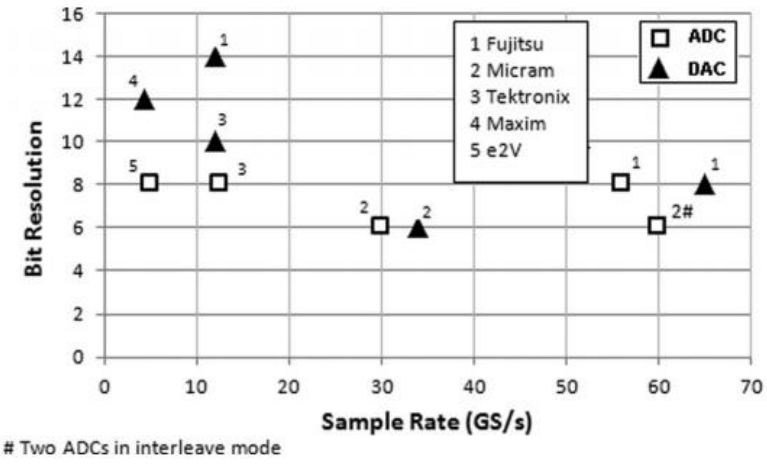

Fig. 2.18 Sample rates and bit resolutions of commercially available DAC/ADCs ([54])

2.6.3 DSP-based OFDM Transceiver Implementation

As the implemented optical transceivers throughout the thesis all employ OFDM for signal modulation, this section describes how OFDM is implemented in DSP.

By using modern DSP technology, modulation/demodulation in the OFDM system can be simply realized by efficient Inverse Fast Fourier Transform (IFFT) and FFT algorithms, respectively. Therefore, when there are a large number of subcarriers employed in the system, DSP makes low cost OFDM implementation feasible compared to the conventional approach of generating each individual subcarrier in the analogue domain [61] which is highly challenging. A practical OFDM system generally consists of a transmitter, a receiver and a transmission link, as depicted in Fig. 2.19.

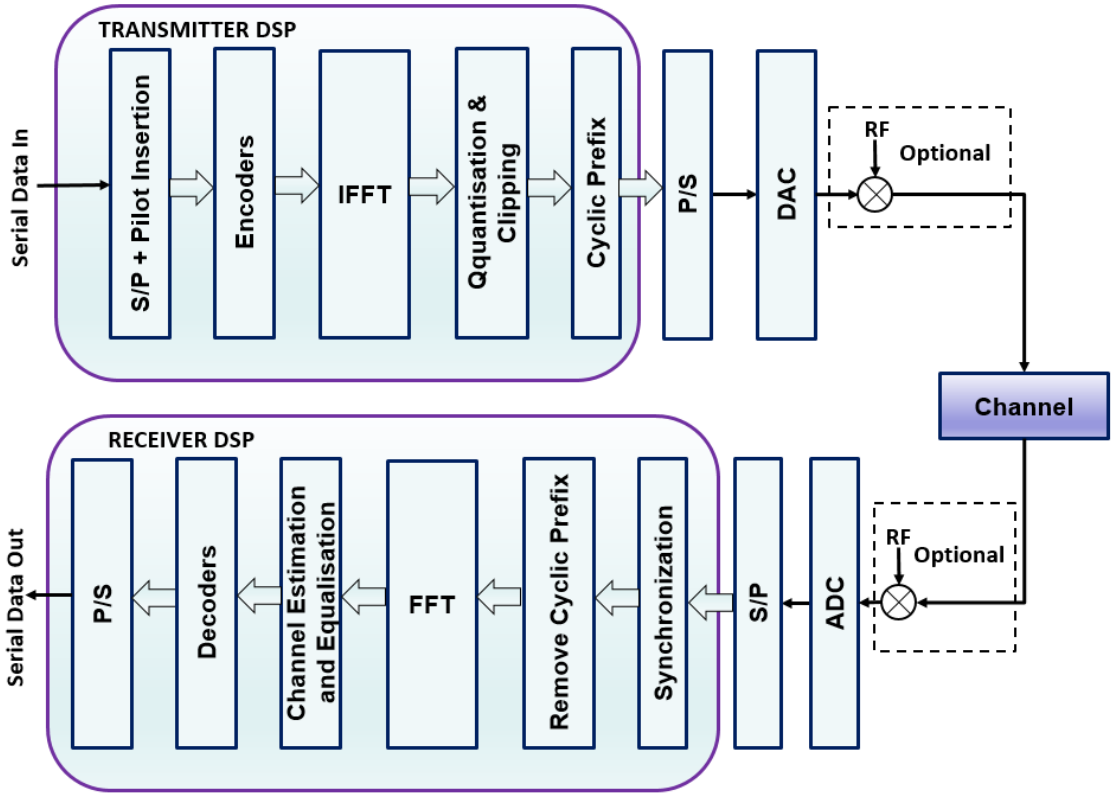

Fig. 2.19 Block diagram of a typical OFDM system. (I)FFT: (inverse) fast fourier transform, DAC: digital-to-analog converter, RF: radio frequency, ADC: analog-to-digital-converter.

The major DSP procedures in the OFDM transmitter include: serial-to-parallel conversion of the incoming binary data, pilot data insertion for channel estimation, bit encoding of each parallel data stream, IFFT, quantisation and clippling, cyclic prefix (CP) insertion and parallel-to-serial conversion of the generated digital samples forming one OFDM symbol. The digital signal is then converted to an analogue signal in a DAC. After that, the analog signal is optionally up-converted with a RF carrier for transmission in the channel.

In the OFDM receiver, the received OFDM signal is firstly optionally down-converted with a RF carrier if required, digitalized in an ADC and then subject to the DSP procedures which are essentially the inverse of those in the transmitter. Here it is noted that symbol synchronization is performed prior to the CP removal stage. In addition, channel estimation and equalization are needed after FFT and prior to decoding stage to compensate for the amplitude and phase response of the whole channel between DAC input and ADC output.

To gain a better understanding of the OFDM transceiver, detailed descriptions of the abovementioned key procedures are presented in the following subsections.

2.6.3.1 IFFT/FFT

IFFT/FFT are the core algorithms at the heart of the OFDM transceiver, as these functions distinguish OFDM from single carrier systems. IFFT/FFT are highly efficient algorithms for computing the Inverse Discrete Fourier Transform (IDFT)/Discrete Fourier Transform (DFT) performing the transformation of signals from frequency to time domain and time to frequency domain, respectively.

In the transmitter, after the encoders the parallel bit streams are mapped onto complex numbers representing QAM or PSK constellations. These parallel complex numbers are then fed to the IFFT, denoted as X_k (k=-N/2,-N/2+1,…,0,1,2,…,(N/2)-1) where X_k is the complex number modulated on the *k*-th subcarrier and *N/2* is the total number of subcarriers (including 0Hz). The output time domain signal of the *N* point IFFT, x_i, can be expressed as [62]:

$$x_i = \frac{1}{N}\sum_{k=-\frac{N}{2}}^{\frac{N}{2}-1} X_k e^{j\frac{2\pi}{N}ki} \qquad i = -\frac{N}{2}, -\frac{N}{2}+1, \dots, 0, 1, 2, \dots, \frac{N}{2}-1 \tag{2.12}$$

In the receiver, the output discrete frequency domain complex numbers of the N point FFT, Y_k, can be expressed as:

$$Y_k = \sum_{i=-\frac{N}{2}}^{\frac{N}{2}-1} y_i e^{-j\frac{2\pi}{N}ik} \qquad k = -\frac{N}{2}, -\frac{N}{2}+1, \dots, 0, 1, 2, \dots, \frac{N}{2}-1 \tag{2.13}$$

where y_i is the sampled time domain signal at the input of the FFT with all y_i samples originating from the same OFDM symbol. Y_k is the frequency domain signal for the *k*th subcarrier at the output of the FFT.

It is worth mentioning that to ensure the generated time domain signal from the IFFT is real valued for use with the IMDD-based optics, the frequency coefficients at the IFFT inputs are arranged with Hermitian symmetry ($X_{-k} = X_k^*$) then for the FFT in the receiver only the positive frequency bins are needed as they contain the same data as the negative frequency bins. Also it should be noted that X_0 is the subcarrier at DC so cannot be used to carry data. The number of data-carrying subcarriers is therefore (N/2)-1.

The FFT is able to extract each subcarrier from the symbol by effectively performing a correlation of the symbol with each of the discrete subcarrier frequencies. If the subcarrier frequency matches the discrete frequency the correlation result is non-zero otherwise it is zero.

After multiplexing all the subcarriers, the resulting time-domain *n*-th OFDM symbol waveform within [(*n-1*)*T*, *nT*], where *T* is the OFDM symbol period, can be written as:

$$x_n(t) = \frac{1}{N}\sum_{k=-\frac{N}{2}}^{\frac{N}{2}-1} X_{k,n} e^{j2\pi f_k t} \tag{2.14}$$

When $x_n(t)$ is sampled at a speed of $f_s = \frac{N}{T}$, then the *m*-th sample within [(*n-1*)*T*, *nT*] can be expressed as:

$$x_n(m) = \frac{1}{N}\sum_{k=0}^{\frac{N}{2}-1} X_{k,n} e^{j2\pi f_k \frac{Tm}{N}} = \frac{1}{N}\sum_{k=0}^{\frac{N}{2}-1} X_{k,n} e^{j\frac{2\pi km}{N}} \tag{2.15}$$

where *m*=0, 1, 2, …, *N*-1. It should be noted that if Eq. (3.15) is rewritten to include the negative frequencies it is similar to Eq. (3.12) thus the OFDM signal can be directly generated by using IFFT.

2.6.3.2 Cyclic Prefix

One of the salient advantages of OFDM is its effective tolerance to ISI in a dispersive transmission channel. ISI causes adjacent received symbols to overlap, so an inter-symbol gap can be inserted between two adjacent symbols to reduce ISI. A cyclic prefix (CP) [63]

which is a copy of the last part of the OFDM symbol, is thus added to the front of the symbol, as shown in Fig. 2.20.

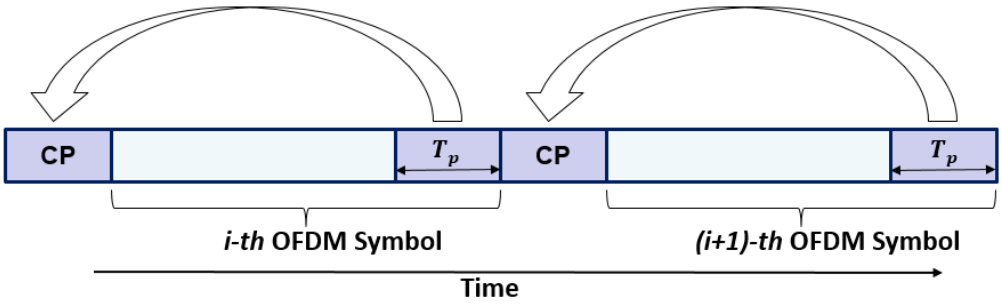

Fig. 2.20 Time domain sequence of OFDM symbols showing the cyclic prefix

If N_s is the number of samples in an original OFDM symbol and $N_c$is the number of samples in the CP, then the new OFDM symbol contains $N_c + N_s$ samples. Therefore, if the time duration of the CP is T_p and the original OFDM symbol period is T_s, then the new OFDM symbol period is $T_p + T_s$. As CP does not carry any extra information for a fixed bandwidth, it reduces the overall transmission capacity. Throughout the thesis, the CP parameter is defined as:

$$\eta = \frac{T_p}{T_s} \tag{2.16}$$

If the delay spread between the subcarrier with the highest delay and subcarrier with the lowest delay is T_d. To effectively compensate the ISI effect, T_p needs to be chosen to satisfy:

$$T_p \geq T_d \tag{2.17}$$

After transmission, the dispersive effect is limited within the CP region only. The distorted CP is removed before performing the FFT in the receiver, thus the original OFDM symbol with useful information can be recovered without interference between different symbols. However, if the CP length is excessive, it prevents the full utilization of available signal bandwidth.

2.6.3.3 Clipping and Quantisation

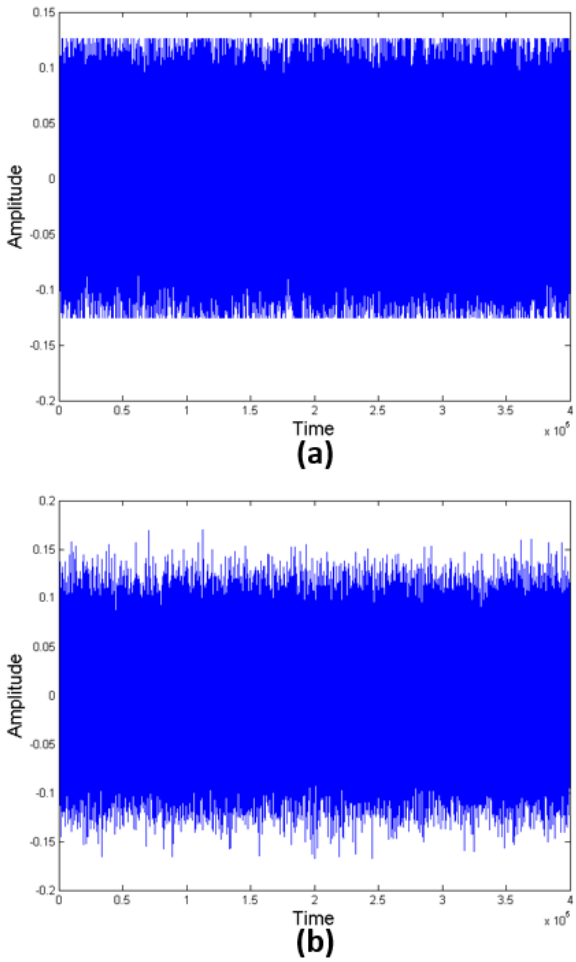

Fig. 2.21 Clipping effet on the OFDM signal at different clipping ratios. (a) 12dB, (b) 15dB.

One of the disadvantages of OFDM is the signal's high peak-to-average power ratio (PAPR) [63]. High peak powers in the optical signal can lead to the non-linear fibre effects associated with high optical signal powers. The high peak optical powers can result in the Kerr effect which leads to non-linear effects such as Self-Phase Modulation, Cross-Phase Modulation and Four-wave Mixing. High PAPR also poses a wide dynamic range requirement for components in the transmitter and receiver, for example high resolution DAC/ADCs. Therefore in the transmitter DSP, clipping is applied to the transmitted OFDM signal to reduce its PAPR. For a given clipping level of $\pm\Lambda$, and assuming $A(t)$ is real, the clipped signal is given by:

$$A_{clip}(t) = \begin{cases} A(t), & -\Lambda \le A(t) \le \Lambda \\ \Lambda, & A(t) > \Lambda \\ -\Lambda, & A(t) < -\Lambda \end{cases} \tag{2.18}$$

The clipping ratio (peak power / average power) ξ is defined as $\xi = \frac{\Lambda^2}{P_m}$ with P_m being the normalised average signal power. Fig. 2.21 shows clearly the OFDM signals subject to different clipping ratios (ξ in dB). An optimum ratio exists as excessive clipping will distort the signal and as mentioned above insufficient clipping will leave the signal with higher PAPR which leads an increased quantisation noise effect.

After clipping, the signal consists of high precision discrete samples and so is then linearly quantized into a set of equally distributed quantization levels within the entire range of [-Λ, Λ] in order to match the bit resolution of the DAC. The quantisation process can be described as follows:

$$A_Q = Q \sum_{i=-\frac{L}{2}+1}^{\frac{L}{2}} \frac{A_i + A_{i-1}}{2} g(A_s, A_i, A_{i-1}) \tag{2.19}$$

where A_Q is the quantized value (in quantisation levels), Q is a scaling factor, A_s is the sampled OFDM signal value, A_i and A_{i-1} represent the i-th and (i-1)-th quantization threshold value. L is the number of quantization levels given by $L = 2^b$ where b is the number of quantization bits. g is the rectangular function defined as:

$$g(x, x_1, x_2) = \begin{cases} 1, & x_1 \le x < x_2 \\ 0, & otherwise \end{cases} \tag{2.20}$$

From the above analysis, it could be understood that the DAC/ADC introduces two major effects on the OFDM signal characteristics which limit system performance: 1) clipping-induced distortion to the signal waveform, and 2) quantization noise due to finite discrete values determined by quantization bits.

2.6.3.4 Pilot-Assisted Channel Estimation and Equalization

The frequency response of a transmission channel introduces subcarrier amplitude and phase changes during transmission. To effectively compensate for this channel frequency response effect, channel estimation and equalization can be employed after the FFT in the receiver. Channel estimation can be realized by transmitting known pilot signals that are interspersed in the useful information in the transmitter [64]. In the receiver, the channel transfer function (CTF) is estimated by extracting the pilot data from the received signals. After transmission, the received OFDM signal for the k-th subcarrier can be written as:

$$y_k(t) = x_k(t) \otimes h_k(t) + w_k(t) \tag{2.21}$$

where $x_k(t)$ is the transmitted OFDM signal for the *k*-th subcarrier, $\otimes$ denotes the convolution operation, $h_k(t)$ is the channel impulse response and $w_k(t)$ is the corresponding total channel noise on the k-th subcarrier. According to the Fourier Transform, after performing the FFT in the receiver, the FFT output for the *k*-th subcarrier is expressed as:

$$Y_k = X_k H_k + W_k \tag{2.22}$$

The CTF based on pilot signals for the k-th subcarrier, ignoring nose, is then determined as:

$$H_k = Y_{p,k}/X_{p,k} \tag{2.23}$$

where $Y_{p,k}$ and $X_{p,k}$ are the received and transmitted pilot signals for the *k*-th subcarrier, respectively. Following the channel estimation, channel equalization can be undertaken to recover the transmitted complex data X_k for the *k*-th subcarrier, as given below:

$$X_k' = Y_k H_k^{-1} = X_k + \frac{W_k}{H_k} \tag{2.24}$$

where X_k' is the recovered complex data and W_k is the complex channel noise for the *k*-th subcarrier. It should be noted that the effects of channel noise on the CTF can be drastically reduced as the estimated CTF can be averaged over a relatively long time duration as long as the channel can be considered to be static over the averaging period [64] and periodically updating the CTF estimate. It should be mentioned that this is one tap equalisation as each subcarrier is multiplied by a single complex coefficient.

2.6.3.5 Synchronization

In practical OFDM system designs, one of the most critical technical issue is synchronization as it considerably affects the system performance. Synchronization errors occur due to two major physical effects: 1) symbol timing offset (STO) induced by the transmission channel [65], 2) sampling clock offset (SCO) [66] induced by the clock mismatch between transmitter and receiver.

STO may cause a fraction of a FFT window for an OFDM symbol to occur in an extended region of the adjacent symbol, leading to system performance degradation. SCO brings about inter-channel interference (ICI) effect as the discrete frequency values do not correspond to the peaks of the sinc [sin(x)/x] waveforms after the FFT in the receiver.

There are mainly two solutions for synchronization: 1) the so-called blind approaches which make use of the features of the repeated OFDM symbol patterns with predetermined time period, and 2) non-blind approaches which take advantage of the features of training or pilot symbols that are interspersed with the transmitted user data. For both approaches, correlation calculations are usually performed, i.e., a sequence of samples is multiplied by a time-shifted copy of the same sequence to produce a time-dependent synchronization profile.

2.7 ROADM Fundamentals

2.7.1 Optical Add Drop Multiplexer (OADM) Functionality

Optical networks have evolved from simple point-to-point connections, to multi-node rings, to all-optical richly interconnected mesh topologies which now fully exploit WDM technology in the core and metro networks. This has introduced a demand for wavelength selective optical add-drop multiplexers (OADM) [67] to separate/route different wavelength channels. An OADM is a device used in WDM systems for multiplexing and routing different channels of light to/from single mode fibre (SMF). The term "Add" refers to the capability of the device to add one or more new wavelength channels to an existing multi-wavelength WDM signal while the term "drop" refers to the extraction of one or more wavelength channels from one network path and passing those signals to another network path. OADMs can be used at different points along the optical link to insert/extract or re-route selected channels therefore configuring the network connectivity. There are two main types of OADM: filter-based OADM and AWG-based OADM.

Fig. 2.22 illustrates the basic operation of a filter-based OADM where 2 channels ($\lambda 1$, $\lambda 3$) are dropped at the 2 drop outputs respectively from the input port. Simultaneously, a stream of 3 channels with central wavelengths $\lambda 2$, $\lambda 4$, $\lambda 6$ are added through the add ports into the signal stream at output port. Alternatively, Fig 2.23 shows an AWG-based OADM where

AWGs are used at both ends to realise the add/drop functions similar to those in Fig. 2.22. The filter-based OADM requires separate filters for each add/drop port and connections must be done manually, whilst the AWG-based OADM provides a simpler design structure. The filter-based OADMs use fixed filters that add/drop a preselected wavelength without the need to demultiplex/multiplex all WDM wavelengths, thus passing the express wavelengths through the node with minimal disturbance. Static wavelength-filtering technology is used which eliminates the cost and attenuation associated with demultiplexing all WDM signals in a signal path. The configuration of the added/dropped channels at each OADM in the network therefore allows control of network interconnections at the wavelength level, thus making OADMs key networking elements for controlling network architecture at the optical wavelength level.

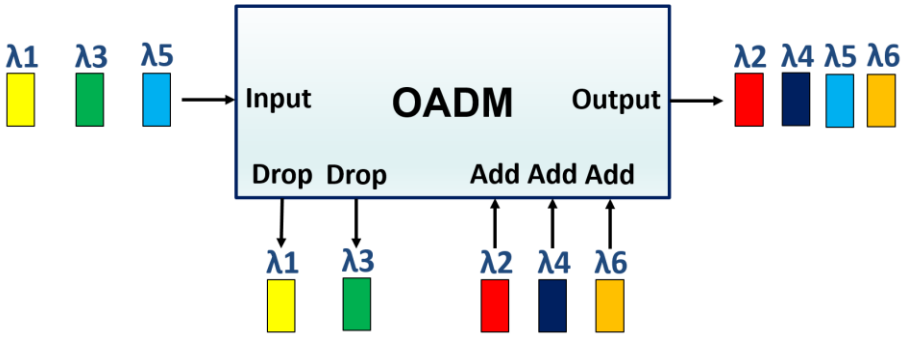

Fig. 2.22 Basic operation of a filter-based OADM

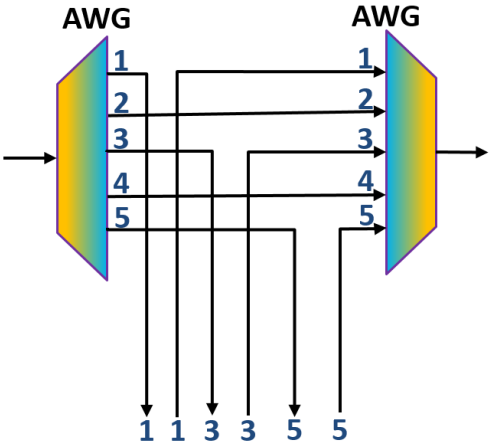

Fig. 2.23 Basic operation of a AWG-based OADM

However, in OADMs the wavelength(s) added and dropped are fixed at the time of add/drop configuration. No configuration changes or additional filters can be added therefore without

interrupting express wavelengths or add/drop wavelengths traveling through the node. The OADM therefore has significant limitations when considering the rapid reconfigurability of the network.

2.7.2 ROADM

As discussed in the last section, an OADM operates on preselected fixed wavelengths and requires manual reconfiguration so is basically fixed once configured. Whereas a ROADM can be reconfigured remotely to dynamically route the different wavelengths in the network. Today's networks must be much more agile than in the past in order to cope with the transition from static traffic patterns to increasingly more dynamic traffic patterns, whilst maintaining high quality of service and network scalability, therefore ROADMs [68] were developed to: i) provide greater flexibility and speed in rerouting optical wavelengths, ii) bypass faulty connections, allowing minimal service disruption and iii) ease the ability to adapt or upgrade the optical network to newer WDM technologies. In a ROADM an optical channel can be dynamically added and dropped under remote software control without the network operator needing to accurately predict the traffic pattern changes as the network can be rapidly reconfigured as required. It therefore introduces huge flexibility in network design and management. ROADMs are key networking elements in the current generation of both long-haul and metro optical networks. They further enhance the communication networks' efficiency as well as offering dynamic connectivity in the optical networks with added network survivability. Current ROADMs use field-proven technology and components, contributing to highly reliable solutions.

ROADMs can be constructed in various ways giving varying levels of performance and cost [69] i.e. liquid crystal [70], micro electromechanical systems (MEMS) [71] tunable optical filter technology [72], and integrated planar lightwave circuit (PLC) [73]. Two typical examples of constructing ROADMs, are shown in Fig. 2.24 and 2.25. Fig. 2.24 shows the basic structure of a ROADM using AWGs and reconfigurable optical switches (OSWs). In AWG and OSW-based ROADMs [74], each add/drop port is dedicated to a specific wavelength reducing flexibility. A more flexible architecture is illustrated in Fig. 2.25 in which wavelength selective switches (WSSs) [75, 76] are utilised so that in such ROADMs each add/drop port can support multiple wavelengths and any wavelength can be routed to any port, and more than one wavelength can be routed to the same port.

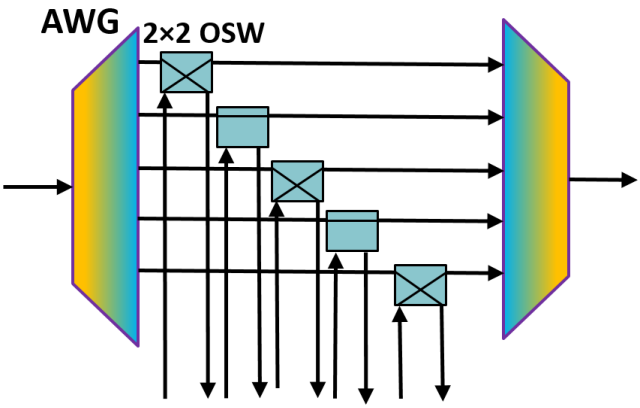

Fig. 2.24 ROADM using AWGs and reconfigurable OSWs.

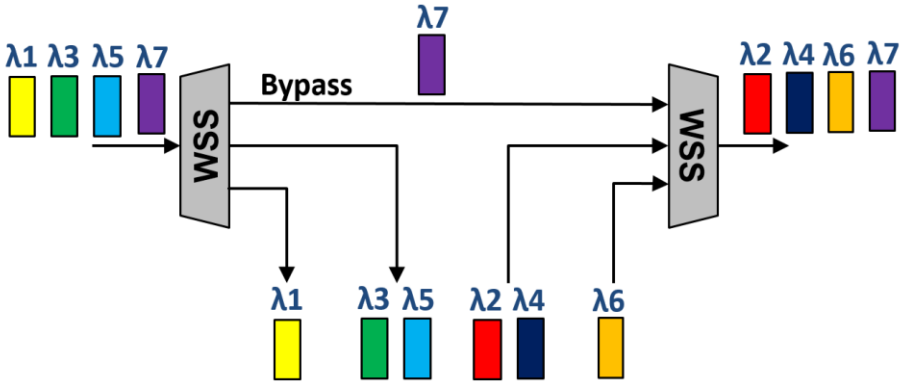

Fig. 2.25 ROADM using WSSs.

To meet the challenges in future optical networks ROADM technology has continued to evolve to improve wavelength agility in a network. There are three key ROADM properties to consider when evaluating ROADM performance: A ROADM should ideally be colourless, directionless and contentionless (CDC) [69, 77, 78]. Colourless indicates that any add/drop port of the ROADM can accommodate any wavelength. Colourless is realized by implementing an add/drop structure that is not wavelength specific. Directionless refers to the ability of an incoming wavelength to be redirected to any arbitrary ROADM output port. Contentionless means cross-connects between add/drop ports and outbound/inbound ports are always possible regardless of cross-connects set up between other ports.

As discussed in section 2.5.2.4, the existing ROADM technologies are not suitable for application in CANs principally due to the fact that they are restricted to switching at the wavelength level only and are too costly. To realise CANs, new cost effective ROADMs are therefore required which meet the requirements outlined in section 2.5.2.4.

References

[1] L. G. Kazovsky, W. T. Shaw, D. Gutierrez, N. Cheng, and S. W. Wong, "Next-generation optical access networks," *J. Lightw. Technol.*, vol. 25, no. 11, pp. 3428-3442, Nov. 2007.

[2] C. F. Lam, Passive Optical Networks: Principles and Practice, Academic Press, Oct. 2007.

[3] D. Veen, V. Houtsma, "High Speed TDM-PON Beyond 10G," in *Optical Fiber Communication Conference (OFC)*, Anaheim, 2016, paper Tu3C.3.

[4] P. Iannone, A. H. Gnauck, M. Straub, J. Hehmann, L. Jentsch, T. Pfeiffer, M. Earnshaw, "An 8-×10-Gb/s 42-km High-Split TWDM PON Featuring Distributed Raman Amplification and a Remotely Powered Intelligent Splitter," *J. Lightw. Technol.*, vol. 35, no. 7, pp. 1328-1332, 2017.

[5] K. Kondepu, L. Valcarenghi, P. Castoldi, "Reconfiguration Triggering Optimization in TWDM PONs with Fluctuating Load," in *Optical Fiber Communication Conference (OFC)*, Anaheim, 2016, paper W2A.67.

[6] D. Y. Qian, J. Q. Hu, P. N. Ji, T. Wang, "10-Gb/s OFDMA-PON for Delivery of Heterogeneous Services," in *Optical Fiber Communication Conference and Exhibition/National Fiber Optic Engineers Conference (OFC/NFOEC)*, San Diego, 2008, paper OWH4.

[7] J. P. Elbers, "Optical access solutions beyond 10G-EPON/XG-PON," *Optical Fiber Communication Conference and Exhibition/National Fiber Optic Engineers Conference (OFC/NFOEC)*, 2010, paper OtuO1.

[8] ITU-T G.983.3, A broadband optical access system with increased service capability by wavelength allocation, available at http://www.itu.int/rec/T-REC-G/e, 2001.

[9] ITU-T G.982, Optical access networks to support services up to the ISDN primary rate or equivalent bit rates, available at http://www.itu.int/rec/T-REC-G/e, 1996.

[10] M. Abrams, P. C. Becker, Y. Fujimoto, V. O'Byrne, and D. Piehler, "FTTP deployments in the United States and Japan—equipment choices and service provider imperatives," *J. Lightw. Technol.*, vol. 23, no. 1, pp. 236-246, Jan. 2005.

[11] IEEE Standard 802.3, *Carrier sense multiple access with collision detection(CSMA/CD) access method and physical layer specifications*, 2005 Edition..

[12] IEEE Standard 802.3, Carrier sense multiple access with collision detection (CSMA/CD) access method and physical layer specifications, 2005 Edition.

[13] D. Nesset, "The PON roadmap," in *Optical Fiber Communication Conference (OFC)*, Anaheim, 2016, paper W4C.1.

[14] K. Habel, M. Koepp, S. Weide, L. Fernandez, C. Kottke, V. Jungnickel, "100G OFDM-PON for Converged 5G Networks: From Concept to Real-Time Prototype," in *Optical Fiber Communication Conference (OFC)*, Los Angeles, 2017, paper W1K.4.

[15] B. Y. Cao, M. L. Deng, Q. W. Zhang, R. P. Giddings, M. Wang, J. M. Tang, "RSOA Intensity Modulator Frequency Chirp-Enhanced Optical OFDM PON Performance," *IEEE Photonics J.*, vol. 7, no. 3, ASN. 7101711, 2015.

[16] J. L. Wei, N. Eiselt, H. Griesser, K. Grobe, M. Eiselt, J. J. Vegas-Olmos, I. T. Monroy, and J. Elbers, "First Demonstration of Real-Time End-to-End 40 Gb/s PAM-4 System using 10-G Transmitter for Next Generation Access Applications," in *European Conference on Optical Communication (ECOC)*, Valencia, 2015.

[17] V. Houtsma, D. Veen, and E. Harstead, "Recent Progress on Standardization of Next-Generation 25, 50, and 100G EPON," *J. Lightw. Technol.*, vol. 35, no. 6, pp. 1228-1234, 2017.

[18] R. W. Chang, "Synthesis of band-limited orthogonal signals for multichannel data transmission," *Bell Syst. Technol. J.*, vol. 45, pp. 1775–1796, 1966.

[19] J. Heiskala and J. Terry, *OFDM Wireless LANs: A Theoretical and Practical Guide*, Sams, 2002.

[20] A. Temtam, D. C. Popescu, O. Popescu, "Using OFDM Pilot Tone Information to Detect Active 4G LTE Transmissions," in *10th International Conference on Communications (COMM)*, Bucharest, 2014, pp. 1-4.

[21] R. E. Ziemer, W. H. Tranter, *Principles of Communications, Fifth Edition*, John Wiley & Sons, Inc., 2002.

[22] W. Y. Chen, G. H. Im, and J. J. Werner, "Design of digital carrierless AM/PM transceivers," *AT&T and Bellcore contribution to ANSI T1E1.4/92-149*, (1992).

[23] L. Tao, Y. Wang, Y. Gao, A. P. T. Lan, N. Chi, and C. Lu, "Experimental demonstration of 10 Gb/s multilevel carrier-less amplitude and phase modulation for short range optical communication systems," *Opt. Exp.*, vol. 21, no. 5, pp. 6459–6465, 2013.

[24] ONF White Paper "Software-Defined Networking: The New Norm for Networks", April 13, 2012.

[25] M. Casado, "Architectural Support for Security Management in Enterprise Networks," Doctoral, Stanford University, Stanford, CA, USA, 2007.

[26] P. Dutta, "Internet Object Caching," in 7*th IEEE Intelligent Network Workshop*, 1998, pp. 95-118.

[27] ONF TR-504 "SDN Architecture Overview", Version 1.1, November, 2014.

[28] N. Cvijetic, A. Tanaka, P. N. Ji, K. Sethuraman, S. Murakami, T. Wang, "SDN and OpenFlow for Dynamic Flex-Grid Optical Access and Aggregation Networks," *J. Lightw. Technol.*, vol. 32, no. 4, pp. 864-870, Jan. 2014.

[29] M. S. Moreolo, L. Nadal, J. M. Fàbrega, "SDN-enabled optical transmission systems: Programmability and advanced features," in *18th Italian National Conference on Photonic Technologies (Fotonica 2016)*, Rome, 2016, pp. 1-4.

[30] P. J. Winzer, R. Essiambre, "Advanced Modulation Formats for High-Capacity Optical Transport Networks," *J. Lightw. Technol.*, vol. 24, no. 12, pp. 4711-4727, Dec. 2006.

[31] I. Morita, "Advanced Modulation Format for 100-Gbit/s Transmission," in *IEEE/LEOS Summer Topical Meetings*, Portland, 2007, paper TuE3.3 (Invited).

[32] J. L. Wei, Q. X. Cheng, R. V. Penty, I. H. White, and D. G. Cunningham, "400 Gigabit Ethernet Using Advanced Modulation Formats: Performance, Complexity, and Power Dissipation," *IEEE Communications Magazine*, pp. 182-189, Feb. 2015.

[33] B. B. Zhang, Z. G. Zhang, Y. X. Chen, "Bitrate Flexible Transceivers Based on IMDD Half-Cycle Subcarrier M-QAM for Software-defined Optical Access Networks," in *15th International Conference on Optical Communications and Networks (ICOCN)*, Hangzhou, 2016.

[34] N. Eiselt, H. Griesser, M. Eiselt, W. Kaiser, S. Aramideh, J. J. V. Olmos, I. Tafur Monroy, J. P. Elbers, "Real-time 200 Gb/s (4×56.25 Gb/s) PAM-4 transmission over 80 km SSMF using quantum-dot laser and silicon ring-modulator," in *Optical Fiber Communication Conference (OFC)*, Los Angeles, 2017, paper W4D.3.

[35] M. Kim, S. H. Bae, H. Kim, Y. C. Chung, "Transmission of 56-Gb/s PAM-4 signal over 20 km of SSMF using a 1.55-μm directly-modulated laser," in *Optical Fiber Communication Conference (OFC)*, Los Angeles, 2017, paper Tu2D.6.

[36] F. Halabi, L. Chen, S. Parre, S. Barthomeuf, R. P. Giddings, C. A. Berthelemot, A. Hamie, and J. M. Tang, "Subcarrier Index-Power Modulated Optical OFDM and Its Performance in IMDD PON Systems," *J. Lightw. Technol.*, vol. 34, no. 9, pp. 2228-2234, 2016.

[37] F. Halabi, L. Chen, R. P. Giddings, A. Hamié, J. M. Tang, "Multilevel Subcarrier Index-Power Modulated Optical OFDM With Adaptive Bit Loading for IMDD PON Systems," *IEEE Photonics Journal*., vol. 8, no. 6, 7907114, 2016.

[38] L. Chen, F. Halabi, R. P. Giddings, J. M. Tang, "Subcarrier Index-Power Modulated Optical OFDM With Superposition Multiplexing for IMDD Transmission Systems," *J. Lightw. Technol.*, vol. 34, no. 22, pp. 5284-5292, 2016.

[39] A. Dupas, P. Layec, E. Dutisseuil, S. Belotti, S. Bigo, E. H. Salas, G. Zervas, and D. Simeonidou, "Elastic Optical Interface With Variable Baudrate: Architecture and Proof-of-Concept," *J. Opt. Commun. Netw.*, vol. 9, no. 2, pp. A170-A175, 2017.

[40] L. Nadal, J. M. Fàbrega, J. A. Altabás, D. Izquierdo, F. J. Vílchez, M. S. Moreolo, J. A. Lázaro, I. Garcés, "Transparent Service Delivery in Elastic Metro/Access Networks with Cost-Effective Programmable Transceivers," in *19th International Conference on Transparent Optical Networks (ICTON)*, Girona, 2017, paper Tu.C2.5.

[41] M. S. Moreolo, L. Nadal, J. M. Fàbrega, "SDN-enabled optical transmission systems: Programmability and advanced features," in *18th Italian National Conference on Photonic Technologies (Fotonica 2016)*, Rome, 2016.

[42] M. S. Moreolo, J. M. Fabrega, L. Nadal, F. J. Vílchez, A. Mayoral, R. Vilalta, R. Muñoz, R. Casellas, R. Martínez, M. Nishihara, T. Tanaka, T. Takahara, J. C. Rasmussen, C. Kottke, M. Schlosser, R. Freund, F. Meng, S. Yan; G. Zervas, D. Simeonidou, Y. Yoshida, K. Kitayama, "SDN-Enabled Sliceable BVT Based on Multicarrier Technology for Multiflow Rate/Distance and Grid Adaptation," *J. Lightw. Technol*., vol. 34, no. 6, pp. 1516-1522, 2016.

[43] S. Yan, Y. Yan, B. R. Rofoee, Y. Shu, E. Hugues-Salas, G. Zervas, D. Simeonidou, "Demonstration of Real-Time Ethernet to Reconfigurable Superchannel Data Transport over Elastic Optical Network," in *European Conference on Optical Communication (ECOC)*, Cannes, 2014.

[44] R. P. Giddings, X. Q. Jin, E. Hugues-Salas, E. Giacoumidis, J. L. Wei, and J. M. Tang, "Experimental demonstration of a record high 11.25Gb/s real-time optical OFDM transceiver supporting 25km SMF end-to-end transmission in simple IMDD systems" *Opt. Express*, vol.18, no.6, pp. 5541–5555, March 2010.

[45] M. Nazarathy, A. Tolmachev and S. B. Ezra, "Sub-Banding DSP for Flexible Optical Transceivers," in *14th International Conference on Transparent Optical Networks (ICTON)*, Coventry, 2012, paper Tu.C1.2.

[46] E. Matarazzo, R. Corsini, A. Peracchi, T. Foggi, G. Meloni, L. Poti, R. Magre, E. Ciaramella, "Blind and Low Complexity CD Compensation and Estimation Method in DSP based Coherent Optical Systems," in *Asia Communications and Photonics Conference (ACP)*, Guangzhou, 2012, paper AS4C.2.

[47] J.N. Zhang, X.G. Yuan, Y.A. Zhang, M.L. Zhang ,X.G. Zhang, "A High-speed Adaptive PMD Compensation Scheme Based on DSP Using DPSO Algorithm," in *OptoElectronics and Communications Conference (OECC)*, Hong Kong, 2009, paper ThQ5.

[48] W.Z. Yan, B. Liu, L. Li, Z.N. Tao, T. Takahara and J.C. Rasmussen, "Nonlinear Distortion and DSP-based Compensation in Metro and Access Networks using Discrete Multi-tone," in *European Conference on Optical Communication (ECOC)*, Amsterdam, 2012, paper Mo.1.B.2.

[49] M. Forzatia, J. Martenssona, H.M. China, M. Mussolina, D. Rafiqueb, F. Guiomarc, "Non-linear compensation techniques for coherent fibre transmission," in *Asia Communications and Photonics Conference (ACP)*, Shanghai, 2011.

[50] Y.X. Dong, E.A. Rawachy, R.P. Giddings, W. Jin, D. Nesset, and J.M. Tang, "Multiple Channel Interference Cancellation of Digital Filter Multiple Access PONs," *J. Lightw. Technol*., vol. 35, no. 1, pp. 34-44, 2017.

[51] Z. Li, M.S. Erkılınç, R. Bouziane, R. Maher, L. Galdino, K. Shi, B.C. Thomsen, P. Bayvel, and R.I. Killey, "Simplified DSP-Based Signal-Signal Beat Interference Mitigation for Direct-Detection Subcarrier Modulation," in *Optical Fiber Communication Conference (OFC)*, Anaheim, 2016, paper W1A.3.

[52] K. Kanonakis and I. Tomkos, "Energy-Efficient OFDMA-PON Exploiting Modular OLT/ONU Digital Signal Processing," in *Optical Fiber Communication Conference (OFC)*, Anaheim, 2013, paper OTh3A.4.

[53] L. Lundberg, C. Fougstedt, P.L. Edefors, P.A. Andrekson and M. Karlsson, "Power Consumption of a Minimal-DSP Coherent Link with a Polarization Multiplexed Pilot-Tone," in *European Conference on Optical Communication (ECOC)*, Düsseldorf, 2016, pp. 1190-1192.

[54] R. P. Giddings, "Real-time Digital Signal Processing for Optical OFDM-Based Future Optical Access Networks (Invited Tutorial)," *J. Lightw. Technol*., vol. 32, no. 4, pp. 553-570, 2014.

[55] S. Straullu, P. Savio, A. Nespola, V. Ferrero, R. Gaudino, S. Abrate, "Demonstration of Upstream WDM+FDMA Reflective PON and Real-Time Implementation on an FPGA Platform," *J. Lightw. Technol.*, vol. 34, no. 8, pp. 2020-2026, 2016.

[56] C. Kim, T. W. Yoo, Y. Kwon, B. T. Kim, "Design and Implementation of an EPON Master Bridge Function in an ASIC," in *11th IEEE Symposium on Computers and Communications (ISCC'06)*, Sardinia, pp. 572-577, 2006.

[57] C. Cox, E. Ackerman, R. Helkey, and G. E. Betts, "Techniques and performance of intensity-modulation direct-detection analog optical links," *IEEE Trans. Mircowave Theory Tech.*, vol. 45, no. 8, pp. 1375–1383, Aug 1997.

[58] A. Villafranca, J. Lasobras, and I. Garces, "Precise characterization of ´ the frequency chirp in directly modulated DFB lasers," in *Spanish Conf. Electron. Devices*, 2007, pp. 173–176.

[59] M. Muller and M. C. Amann, "State-of-the-art and perspectives for long- ¨ wavelength high speed VCSELs," in 13th *Int. Conf. Transp. Opt. Netw.*, Stockholm, Sweden, 2011, pp. 1–4, Paper Mo.C5.2.

[60] M.L. Deng, N. Jiang, X. Duan, R.P. Giddings, X.W. Yi, B.Y. Cao, S. Mansoor, K. Qiu, and J.M. Tang, "Robust and tunable 16.375Gb/s dual-band optical OFDM transmissions over directly modulated VCSEL-based 200m OM2 MMFs" *Opt. Express*, vol.23, no.1, pp. 373–383, 2015.

[61] N. Cvijetic, "OFDM for next-generation optical access networks," *J. Lightw. Technol.*, vol. 30, no. 4, pp. 384–398, Feb. 2012.

[62] W. Shieh and I. Djordjevic, *Orthogonal Frequency Division Multiplexing for Optical Communications*, Academic Press, Inc., 2010.

[63] J. Heiskala and J. Terry, *OFDM Wireless LANs: A Theoretical and Practical Guide*, Sams, 2002.

[64] X. Q. Jin, R. P. Giddings, J. M. Tang, "Real-time transmission of 3Gb/s 16-QAM encoded optical OFDM signals over 75km SMFs with negative power penalties," *Opt. Express*, vol. 17, no. 17, pp. 14574-14585, 2009.

[65] X. Q. Jin, R. P. Giddings, E. Hugues-Salas, and J. M. Tang, "Real-time experimental demonstration of optical OFDM symbol synchronization in directly modulated DFB laser-based 25 km SMF IMDD systems," *Opt. Exp*., vol. 18, no. 20, pp. 21100–21110, Sep. 2010.

[66] D. K. Kim, S. H. Do, H. B. Cho, H. J. Chol, K. B. Kim, "A new joint algorithm of symbol timing recovery and sampling clock adjustment for OFDM systems," *Trans. Consumer Electronics*, vol. 44, no. 3, pp. 1142-1149, 1998.

[67] S. Johansson, "Transport Network Involving a Reconfigurable WDM Network Layer-A European Demonstration," *J. Lightw. Technol*., vol. 14, no. 6, pp. 1341-1348, 1996.

[68] J. Wagener, T. Strasser, "Characterization of the economic impact of stranded bandwidth in fixed OADM relative to ROADM networks," in *Optical Fiber Communication Conference and the National Fiber Optic Engineers Conference (OFC/NFOEC)*, Anaheim, 2006, paper OThM6.

[69] S. Gringeri, B. Basch, V. Shukla, R. Egorov, and T. J. Xia, "Flexible Architectures for Optical Transport Nodes and Networks," *IEEE Communications Magazine*, vol. 48, no. 7, pp. 40-50, 2010.

[70] K. Suzuki, K. Seno, Y. Ikuma, "Application of Waveguide/Free-Space Optics Hybrid to ROADM Device," *J. Lightw. Technol*., vol. 35, no. 4, pp. 596-606, 2017.

[71] H. N. Yang, B. Robertson, P. Wilkinson, D. P. Chu, "Low-Cost CDC ROADM Architecture Based on Stacked Wavelength Selective Switches," *J. Opt. Commun. Netw*., vol. 9, no. 5, pp. 375-384, 2017.

[72] R. Itoh, T. Konishi, K. Itoh, "Arbitrary Wavelength- and Time-Selective Reconfigurable Optical Add/Drop Multiplexer (ROADM) Using a Time-Space Conversion and a MEMS Optical Switch," in *European Conference on Optical Communication (ECOC)*, Cannes, 2006.

[73] T. Watanabe, K. Suzuki, T. Goh, K. Hattori, A. Mori, T. Takahashi, T. Sakamoto, "Compact PLC-based Transponder Aggregator for Colorless and Directionless ROADM," in *Optical Fiber Communication Conference and Exposition and the*

National Fiber Optic Engineers Conference (OFC/NFOEC), Los Angeles, 2011, paper OTuD3.

[74] S. Takashina, Y. Mori, H. Hasegawa, K. I. Sato, T. Watanabe, "Wavelength-Tunable Filters Utilizing Arrayed Waveguide Gratings for Colorless/Directionless/Contentionless Optical Signal Drop in ROADMs," *IEEE Photonics Journal*., vol.7, no. 1, 7100511, 2015.

[75] L. J. Zong, H. Zhao, Z. Y. Feng, Y. F. Yan, "Low-cost, Degree-expandable and Contention-free ROADM Architecture Based on M × N WSS," in *Optical Fiber Communication Conference (OFC)*, Anaheim, 2016, paper M3E.3.

[76] M. Niwa, Y. Mori, H. Hasegawa, K. Sato, "MxM WSS Based ROADM Architecture with Topology- Insensitive Routing Performance," in *European Conference on Optical Communication (ECOC)*, Düsseldorf, 2016, pp. 824-826.

[77] M. Garrich, E. Magalhães, H. Carvalho, N. G. Gonzalez, G. Zervas, D. Simeonidou, and J. R. F. Oliveira, "Experimental Demonstration of Function Programmable Add/Drop Architecture for ROADMs [Invited]," *J. Opt. Commun. Netw*., vol. 7, no. 2, pp. A335-A343, 2015.

[78] J. M. Simmons, A. A. M. Saleh, "Wavelength-Selective CDC ROADM Designs Using Reduced-Sized Optical Cross-Connects," *IEEE Photonic. Tech. Lett.*, vol. 27, no. 20, pp. 2174-2177, 2015.

3. Software Reconfigurable Optical Transceivers Utilizing DSP-based Digital Orthogonal Filters

Contents

3.1 Introduction

Having outlined the key requirements of reconfigurable optical transceivers in section 2.5.2.2, this chapter presents an initial investigation of newly proposed software reconfigurable adaptive optical transceivers as they are one of the fundamental building blocks for implementing future CANs in the physical layer.

Recently, a novel signal multiplexing technique using digital orthogonal filters has been proposed [1], which can multiplex multiple variable bandwidth and independent channels at the physical layer to enable reconfigurable network connectivity. Digital orthogonal filters embedded in DSP logic are employed to multiplex/demultiplex multiple channels to/from a single optical signal.

In this chapter, numerical investigations are firstly undertaken to investigate the standard single-mode fibre (SSMF) link transmission performance of the proposed digital orthogonal filtering-based reconfigurable optical transceivers utilising two channels supporting OFDM modulated signals. The impacts of digital filter tap count on transmission performance using different subcarrier modulation formats are also explored based on which the optimum filter tap count is identified.

Secondly, real-time experimental demonstrations of on-line software reconfigurable adaptive digital orthogonal filtering-based transceivers are undertaken, where two real-valued digital orthogonal filtering-based channels are multiplexed/demultiplexed utilizing field programmable gate array (FPGA)-based 32-tap digital orthogonal filters in the digital domain without involving any sophisticated signal conversion in the RF domain and/or IQ modulation in the optical domain. To demonstrate operation with advanced modulation formats, the two multiplexed channels both employ OFDM modulation. The transmission performance and channel reconfigurability of the transceivers are experimentally examined in simple 25km SSMF IMDD systems, over which experimental explorations are also undertaken of the inherent transceiver adaptability enabled by adaptive OFDM bit loading. The experimental work rigorously verifies the proposed digital orthogonal filtering-based channel multiplexing technique, and more importantly, confirms the feasibility of practically implementing DSP-based software reconfigurable adaptive digital orthogonal filtering-based transceivers for future CANs.

3.2 Digital Orthogonal Filtering-based Channel Multiplexing Principles

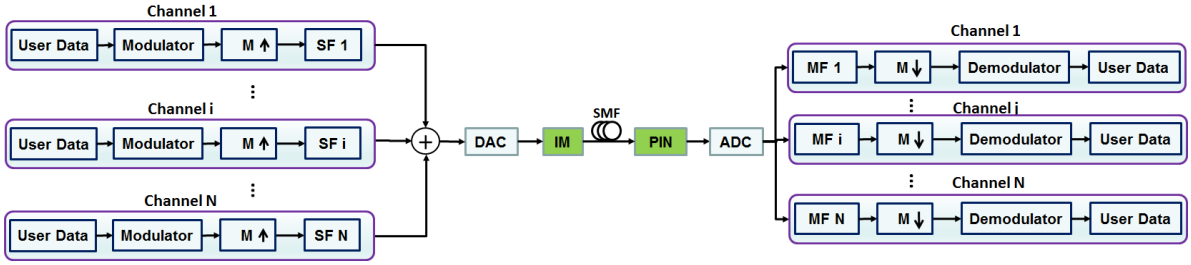

Fig. 3.1 Schematic diagram of software reconfigurable transceivers for multiplexing/demultiplexing digital orthogonal filtering-based channels.
SF: shaping filter, DAC: digital to analogue converter, IM: intensity modulator, ADC: analogue to digital converter, MF: matching filter

The block diagram of the proposed digital orthogonal filtering-based channel multiplexing technique used for software reconfigurable transceivers is depicted in Fig. 3.1, where N bandwidth-variable channels are multiplexed/demultiplexed using digital orthogonal filters that can be embedded in digital logic integrated circuits (ICs). For each channel, an independent signal is first up-sampled (M↑) by a factor M by inserting M-1 zeros between two consecutive samples, and subsequently passes through a digital shaping filter (SF). As a result, a digital orthogonal filtering-based channel is generated at the output of the shaping filter. All the generated digital orthogonal filtering-based channels are added together in the digital domain and input to a single DAC. The resulting analogue electrical digital orthogonal filtering-based signal is then fed to an optical intensity modulator (IM), and the optical signal is launched into an IMDD SSMF system. After transmitting through the SSMF, the optical signal is detected by a photo detector (PD), and the detected signal, after digitising by an ADC, is fed to different receivers, where each digital signal is first filtered by a suitable matching filter (MF) to demultiplex the corresponding digital orthogonal filtering-based channel, which is then subsequently down-sampled (M↓) by a factor of M by selecting every M-*th* sample. Finally, the received binary data is recovered after demodulation.

The heart of the software reconfigurable transceiver is the use of digital orthogonal filters to combine and separate different digital channels. In the transmitter, different parallel shaping filters with orthogonal impulse responses, $s_i(t)$, where i represents the shaping filter in i-*th*

channel, are adopted. The sum of all the digital orthogonal filtering-based channels indicated in Fig. 3.1 can be expressed as:

$$x(t) = \sum_{i=1}^{N} a_i(t) \otimes s_i(t) \tag{3.1}$$

where $a_i(t)$ is the up-sampled input signal to the i-*th* filter in the continuous time domain. Assuming that the resulting multiplexed signal, *x*(*t*), propagates through an ideal transmission system, the output signal emerging from the j-*th* matching filter in the receiver can be written as:

$$a_j(t) = [\sum_{i=1}^{N} a_i(t) \otimes s_i(t)] \otimes m_j(t) \tag{3.2}$$

It can be easily seen from Eq. 3.2 that to recover the signal conveyed by each digital orthogonal filtering-based channel without suffering unwanted interferences, the shaping and matching filter impulse responses must satisfy:

$$s_i(t) \otimes m_j(t) = \begin{cases} \delta(t - t_0) & i = j \\ 0 & i \neq j \end{cases} \tag{3.3}$$

where t_0 corresponds to the time delay induced by the orthogonal filters. According to Eq. 3.3, two spectrally overlapping orthogonal (in-phase and quadrature-phase) channels can be multiplexed/demultiplexed. The filters can be designed to support an in-phase or quadrature-phase channel.

A Hilbert pair is taken as the digital orthogonal filters satisfying Eq. 3.3. The impulse responses of the employed *i*-th shaping filters are given by:

$$\begin{aligned} s_i^I(t) &= g(t)\cos(2\pi f_c t) \\ s_i^Q(t) &= g(t)\sin(2\pi f_c t) \end{aligned} \tag{3.4}$$

where f_c is the central frequency of the corresponding sub-band and $g(t)$ is the baseband pulse whose impulse and frequency response are illustrated in Fig. 3.2. $g(t)$ has a square-root raised-cosine form expressed as [2]:

$$g(t) = \frac{\sin[\pi(1-\alpha)t'] + 4\alpha t' \cos[\pi(1+\alpha)t']}{\pi t'[1-(4\alpha t')^2]}, \quad t' = \frac{t}{T} \tag{3.5}$$

where T is the sample period (prior to up-sampling), and the α parameter controls the excess of bandwidth with respect to the minimum bandwidth determined by the sample period $(1/T)$ as shown in Fig. 3.2. Here T is chosen to be 1ns.

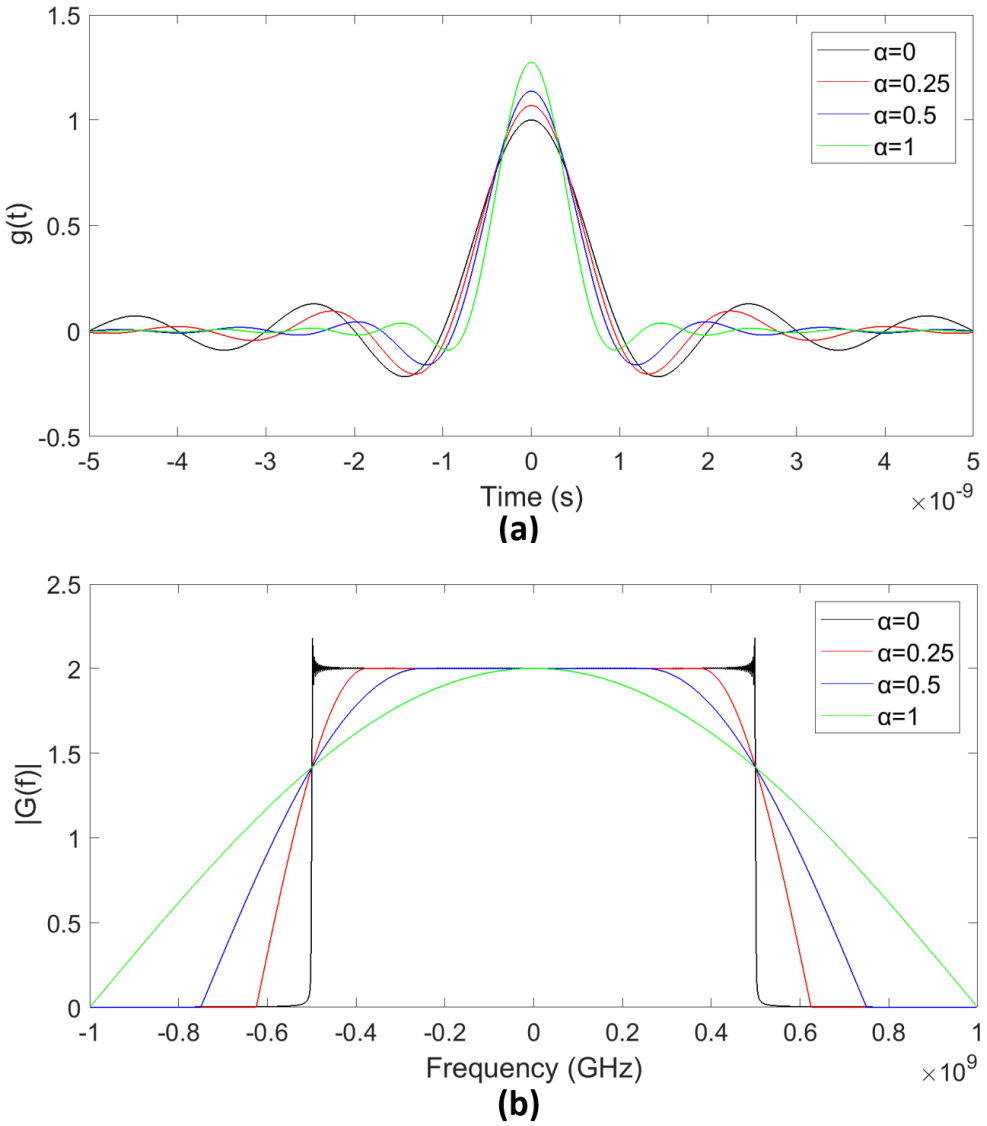

Fig. 3.2 (a) Impulse and (b) frequency response of the baseband pulse $g(t)$

f_c must be larger than the highest frequency of $g(t)$ in order to avoid the aliasing effect. For the Hilbert pair considered, the corresponding matching filters are given by [3, 4]:

$$\begin{aligned} m_i^I(t) &= s_i^I(-t) \\ m_i^Q(t) &= s_i^Q(-t) \end{aligned} \tag{3.6}$$

Based on Eq. 3.5, for a fixed DAC/ADC sampling rate, the total bandwidth of each digital orthogonal filtering-based channel, W, can be written as:

$$W = \frac{1}{T}(1+\alpha) \tag{3.7}$$

To avoid the aliasing effect in the generation/detection of the digital orthogonal filtering-based channel, the following condition should also be fulfilled:

$$W \leq \frac{M}{NT} \tag{3.8}$$

where N is the number of channels. In the filter design, the α parameter can vary in a range of $0 \leq \alpha \leq 1$. When $\alpha = 1$ the signal has its maximum bandwidth so the minimum oversampling factor should be $M = 4$, which is regarded as an optimum parameter value for the performance-complexity trade-off in conventional 2-D CAP systems [5]. On the other hand, when $\alpha = 0$ the signal has its minimum bandwidth so the oversampling factor can be reduced to $M = 2$, thus bandwidth utilisation can be maximised.

To clarify the principle of utilising Hilbert-pair digital orthogonal filters, an example of the ideal frequency and phase response of I and Q components of the Hilbert-pair are shown in Fig. 3.3. The key difference between I and Q filters is that there is a π/2 difference in the phase response so that they are therefore orthogonal to each other.

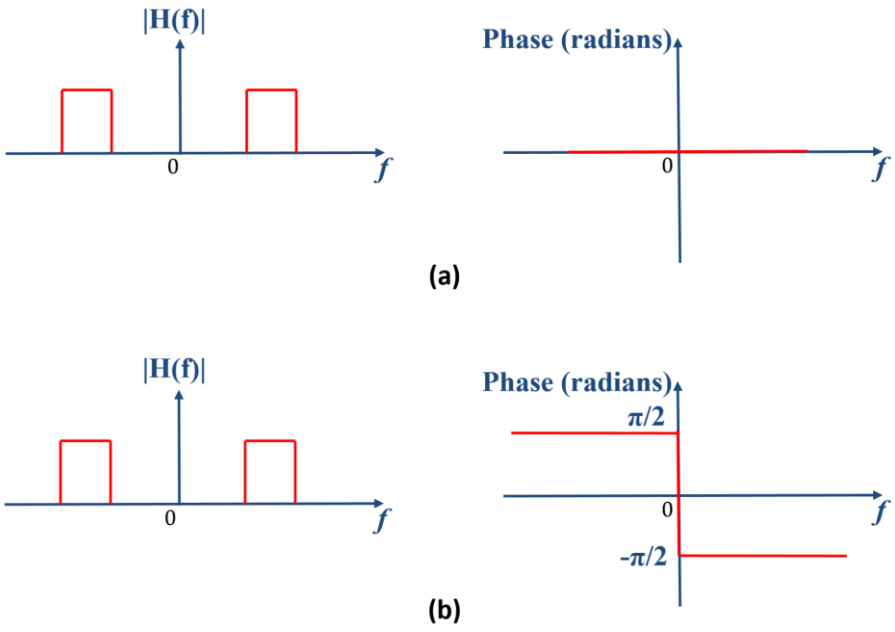

Fig. 3.3 Example of frequency and phase response of (a) I and (b) Q component of Hilbert-pair digital orthogonbal filters

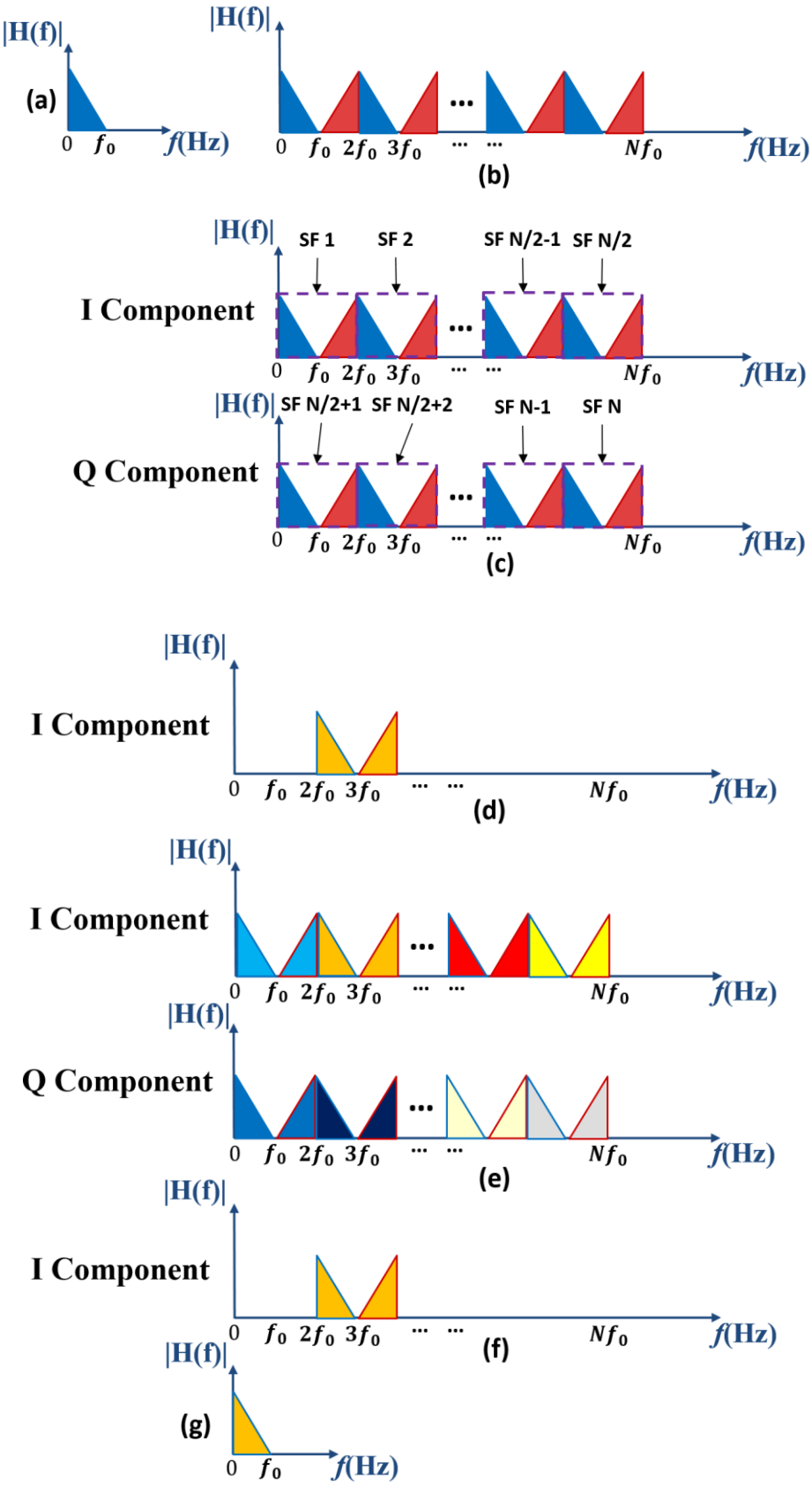
|H(f)|
(a)
0
f_0
f(Hz)
|H(f)|
0
f_0 $2f_0$ $3f_0$ ... ... Nf_0
f(Hz)
(b)
|H(f)|
SF 1
SF 2
SF N/2-1
SF N/2
I Component
0
f_0 $2f_0$ $3f_0$ ... ... Nf_0
f(Hz)
|H(f)|
SF N/2+1
SF N/2+2
SF N-1
SF N
Q Component
0
f_0 $2f_0$ $3f_0$ ... ... Nf_0
f(Hz)
(c)
|H(f)|
I Component
0
f_0 $2f_0$ $3f_0$ ... ... Nf_0
f(Hz)
(d)
|H(f)|
I Component
0
f_0 $2f_0$ $3f_0$ ... ... Nf_0
f(Hz)
|H(f)|
Q Component
0
f_0 $2f_0$ $3f_0$ ... ... Nf_0
f(Hz)
(e)
|H(f)|
I Component
0
f_0 $2f_0$ $3f_0$ ... ... Nf_0
f(Hz)
(f)
|H(f)|
(g)
0
f_0
f(Hz)

Fig. 3.4 Spectrum of original data signal (a) before up-sampling and (b) after up-sampling of N times, (c) shaping filter frequency response.(d) after SF 2, (e) combined of multiple channels, (f) after MF 2, (g) after down-sampling.

To further illustrate the digital orthogonal filtering technique an example of the signal spectrum before and after up-sampling of N times and the corresponding shaping filter frequency response of each channel in the transmitter are illustrated in Fig. 3.4 (a), (b) and (c). f_0 is the original signal bandwidth before up-sampling. Each pair of blue and red spectra illustrates the mirrored spectra containing upper and lower sidebands due to the up-sampling effect. The up-sampling also generates multiple spectral images within the Nyquist frequency band. The dashed lines show the example frequency responses of shaping filters 1 to N present in Fig. 3.1. A filter selects one of the images (including upper and lower sidebands) according to the desired spectral location of the signal. According to Eq. 3.4, each pair of orthogonal shaping filters has an I and Q component, and it can be seen from Fig. 3.4 that filters such as SF 1 and SF N/2+1 occupy the same frequency but their phase response is 90 degrees different so that the I and Q component are generated respectively.

Fig. 3.4(d) shows an example output spectrum of a shaping filter if its coefficients are set for SF 2, Fig. 3.4 (e) shows the combined spectrum of multiple channels (each color represents one channel), Fig. 3.4 (f) shows the spectrum after filering by the corresponding MF 2 where MF 2 filters out all the other channels so extracting the desired channel, and finally Fig. 3.4 (g) shows the spectrum of the recovered channel after down-sampling.

3.3 Software Reconfigurable Optical Transceivers Theoretical Performance

Table 3.1. Simulation system parameters

Parameter	Value
Total number of IFFT/FFT points per channel	32
Data-carrying subcarriers per channel	15

n-th subcarrier frequency	n×31.25MHz
Adaptive modulation formats on all subcarriers	16-QAM, 32-QAM, 64-QAM
Up-sampling factor	2
DAC & ADC sample rate	2GS/s
DAC & ADC resolution	8 bits
Symbol rate	50MHz
Samples per symbol (IFFT)	32 samples (16ns) #
Cyclic prefix	8 samples (4ns) #
Total samples per symbol	40 samples (20ns) #
PIN detector bandwidth	12.5GHz
PIN detector sensitivity	-19dBm*
Fiber dispersion parameter	17 ps/nm/km
Fiber dispersion slope	0.07 ps/nm^2/km
Fiber loss	0.2 dB/km
Fiber Kerr coefficient	2.35×10-20 m^2/W

Before up-sampling and after down-sampling
* Corresponding to 10 Gb/s non-return-to-zero data at a BER of 1.0×10^{-9}

In this section, to demonstrate the key characteristics of the proposed software reconfigurable transceiver, numerical simulations are undertaken to explore the transmission performance of a digital orthogonal filtering-based reconfigurable transceiver which multiplexes two channels in a single point-to-point SSMF link.

To sufficiently minimise the digital filtering DSP complexity and power consumption with the acceptable system performance still being satisfied, it is necessary to find a suitable filter tap count that achieves a good balance between these requirements. It is therefore essential to explore the impacts of the digital filter tap count on the system BER performance. Due to the up-sampling and down-sampling not all taps need to be physically implemented however the number of digital multipliers required will be proportional to the tap count. For this investigation a 2 channel system employing an oversampling factor M = 2 is considered to maximise bandwidth utilisation [1].

Throughout this section, OFDM signal generation and recovery is performed using the DSP functions as described in section 2.6.3, and all simulation parameters are given in table 3.1. It should be noted that before OFDM modulation the bit pattern test sequence is generated using the MATLAB "randn" function to ensure equal probability of 1s and 0s. The sampling rate of the DAC/ADC considered is $f_{DAC/ADC}$ = 2 GS/s and all the digital filters also operate at this rate, thus the data samples prior to up-sampling are generated at a speed of $f_{data} = f_{DAC/ADC}/M$ =1GS/s. The signal line rate of each digital orthogonal filtering-based channel can be calculated by:

$$R_b = \frac{f_{DAC}\sum_{k=1}^{N_S} n_{kb}}{2(N_S+1)(1+C_p)M} \tag{3.9}$$

where n_{kb} is the number of binary bits conveyed by the *k*th subcarrier within one symbol period, N_S is the number of data-bearing subcarriers and C_p is the overhead parameter associated with the cyclic prefix. Here C_p = 0.25 is utilized. It should be noted that, in comparison with the conventional OFDM system [6], the signal line rate given by Eq. 3.9 is reduced by a factor of *M*. However there is no net loss in total transmission capacity due to the fact that there are M channels, thus the total bit rate is maintained compared to conventional OFDM. The filter tap counts evaluated are 16, 32 and 64. To highlight the key aspects of interest, for optical signal modulation/detection an ideal intensity modulator is employed together with a PIN having a quantum efficiency of 0.8 and a sensitivity of –19 dBm.

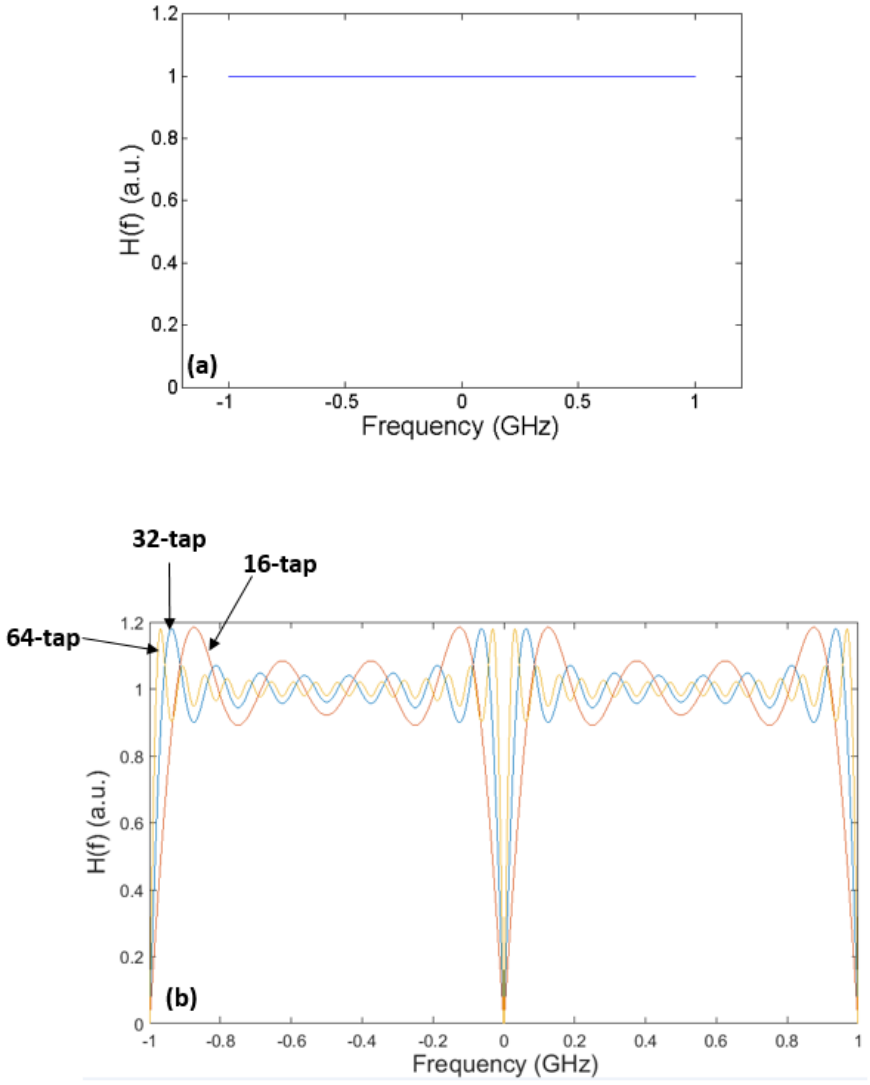

Fig. 3.5 Frequency response of the shaping and matching filter for (a) channel 1 and (b) channel 2.

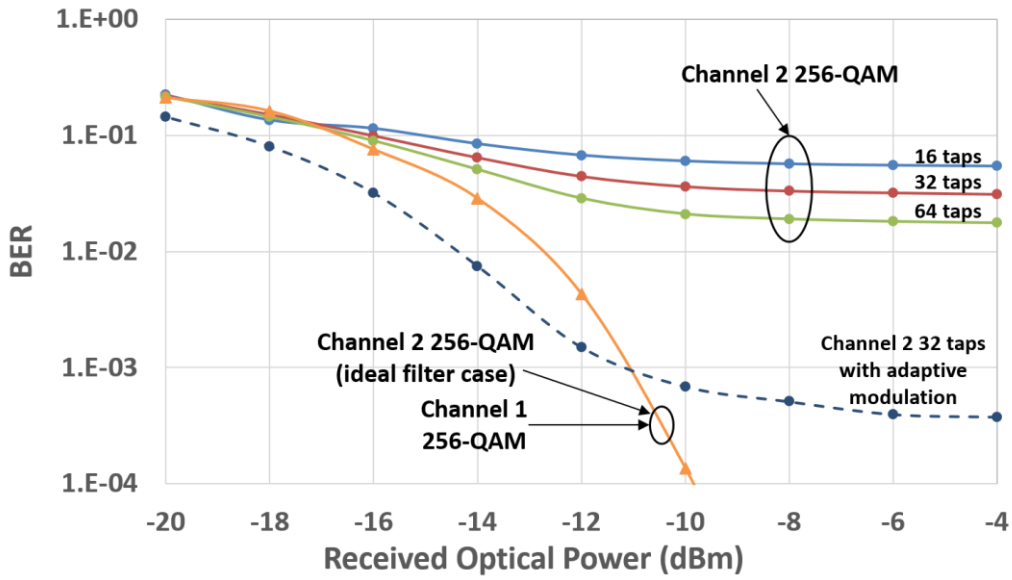

Fig. 3.6 BER performance versus received optical power for both channels using different number of digital filter taps when 256-QAM is used for all subcarriers. Adaptive modulation applied to channel 2 is highlighted using a dashed line.

When an oversampling factor of M =2 is used, the central frequencies of the filters are set to at $f_c = f_{DAC/ADC}/4 = 0.5$ GHz, and the excess of bandwidth is set to $\alpha = 0$. The shaping filter amplitude frequency responses with 16-taps, 32-taps and 64-taps for both channels are represented in Fig. 3.5 (a) and (b). Channel 1 corresponds to $s_1^I(t)$ in Eq. (3.26) and is known as the cosine channel and channel 2 corresponds to $s_1^Q(t)$ and is known as the sine channel. As shown in Fig. 3.5 (a) and (b), the channel 1 frequency response is perfectly flat for all tap counts and the channel 2 frequency response has an oscillating structure, whose amplitude variation range reduces with increasing the number of taps. This is because the frequency response of channel 1 has only one non-zero coefficient, so it is effectively just a delay. The amplitude responses of the matching filters are identical to those of their corresponding shaping filters, as the matching filters' impulse responses are just the time reverse of those corresponding to the shaping filters. Therefore the cosine (sine) matching filter will have a phase shift of 0 (180) degrees relative to the cosine (sine) shaping filter due to its symmetric (asymmetric) impulse response.

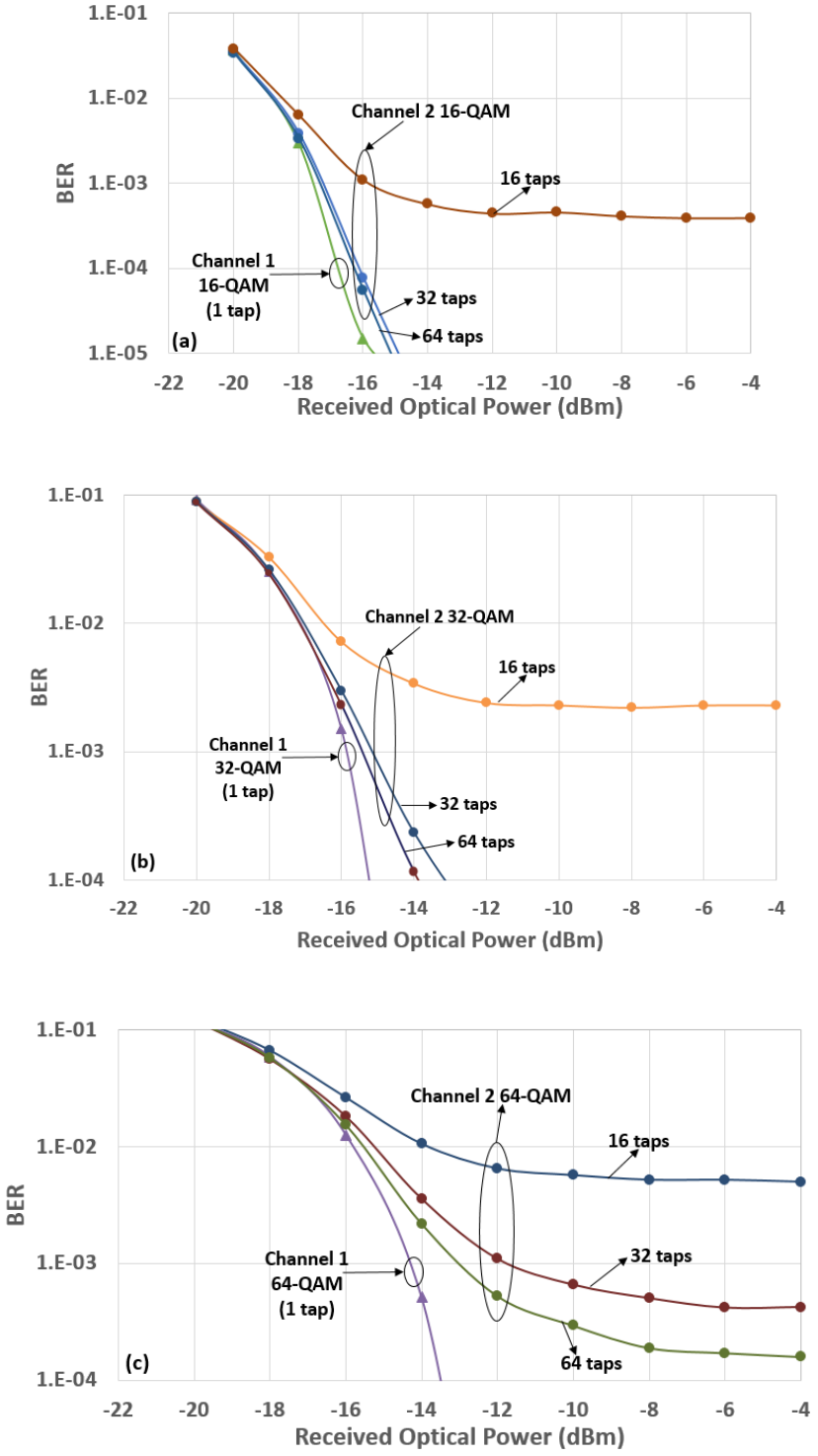

Fig. 3.7 BER performance versus received optical power for both channels using different number of digital filter taps when (a) 16-QAM, (b) 32-QAM, (c) 64-QAM is used for all subcarriers

The system BER performances in 25km IMDD SSMF configurations are investigated in Fig. 3.6 and 3.7, where the BER of each individual digital orthogonal filtering-based channel as a function of received optical power is plotted for the various tap counts used. As expected

from Fig. 3.5 (a), Fig. 3.6 shows that the BER performance of channel 1 is independent of the digital filter tap count, and that a fixed filter design supports all signal modulation formats as high as 256-QAM.Whilst for channel 2's performance, the BER floor develops, which decreases with increasing number of the filter taps because of the large tap count-induced flatness of the channel 2 frequency response, as illustrated in Fig. 3.5 (b). However, channel 2 BERs of $<1.0 \times 10^{-3}$ are still not obtainable even for the case of including 64 filter taps. Here it should be mentioned that if channel 2 also uses ideal filter as channel 1, their BER performance are expected to be the same (as the performance of channel 1 indicated in Fig. 3.6) In sharp contrast, the use of adaptive bit loading across channel 2 subcarriers significantly improves its' BER performance, and BERs far below 1.0×10^{-3} are easily achievable even when 32 filter taps are used, as shown in Fig. 3.6. The corresponding reduction in capacity due to the adaptive bit loading is only 15%. Therefore, it is concluded from Fig. 3.6 that, in comparison with the conventional CAP systems, the proposed digital orthogonal filtering-based channel multiplexing technique utilising OFDM modulation not only significantly relaxes the requirements on digital filter tap counts, but also allows a range of signal modulation formats to be adaptively selected according to the channel OSNRs.

To further explore the impact of digital filter tap count on system transmission performance using different modulation formats, and thus determine a suitable tap count for practical implementation, Fig. 3.7 shows BER performances of both channels for different digital filter tap counts and different modulation formats. Here the 1st subcarrier of channel 2 is dropped due to excessive errors induced by the associated high attenuation in the sine filter frequency response. It can be seen that 32-taps provide a good trade-off between system transmission performance and digital filter DSP design complexity. It reduces DSP complexity by half compared to 64-tap filters for only a small reduction in performance for modulation formats up to 64-QAM on all subcarriers, and adaptive bit loading can allow modulation formats up to 256-QAM. Therefore, 32-tap filters are adopted in the experimental demonstrations which are discussed in the next section.

3.4 Real-time Experimental Demonstrations of Software Reconfigurable Transceivers for Point-to-Point SDN PONs

3.4.1 Real-time DSP Platform

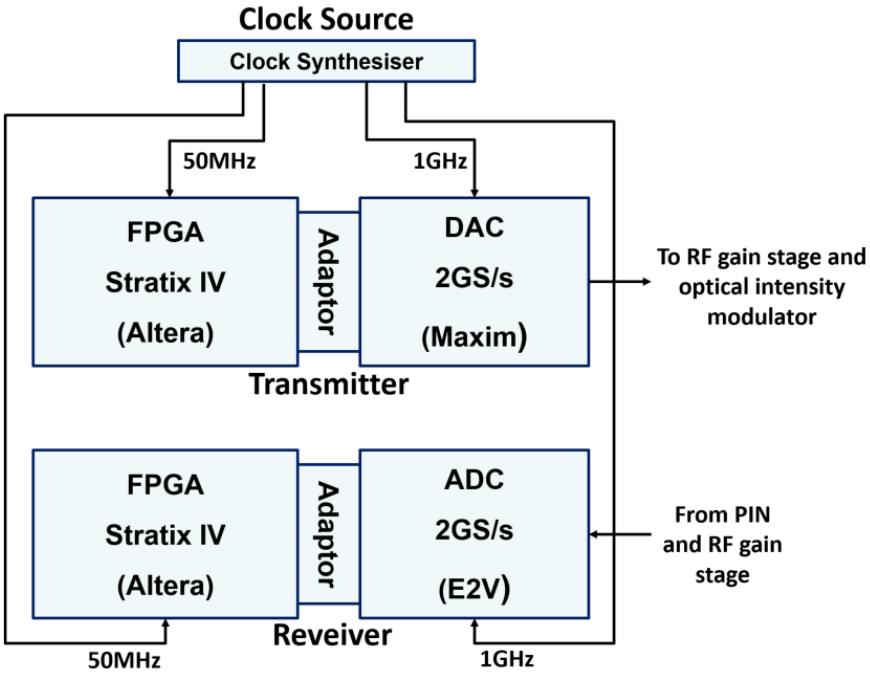

Fig. 3.8 Real-time transceiver DSP platform basic architecture.

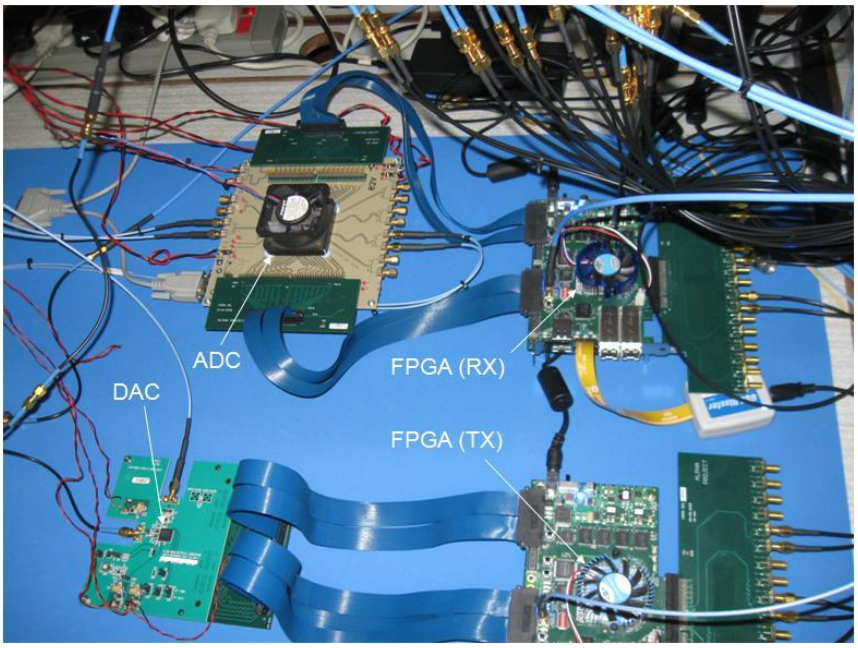

Fig. 3.9 Real-time transceiver DSP platform

Fig. 3.8 shows the real-time transceiver DSP platform including FPGAs, interface adaptors, DAC/ADC and clock source, and Fig. 3.9 shows a photograph of the real-time transceiver platform. The key component specifications are listed in Table 3.2:

Table 3.2. System Components specifications

Component	Type	Key Parameters
FPGA	Altera: Stratix IV GX EP4SGX230KF40C2	• 228k logic elements (LEs) • 1288 18×18 multipliers • 0.6 Gbps-6.5 Gbps high-speed transceivers • Up to 17,133 Kb of total memory
DAC	Maxim: MAX5881	• Resolution: 12-bit • Sample rate: 4.3GS/s • Output voltage: $660V_{pp}$ • 4×8-bit LVDS ports
ADC	E2V: EV8AQ160	• Resolution: 8-bit • ENOB: 7.1 bits@5GS/s • Sample rate: 5GS/s • Output voltage: $600Mv_{pp}$ • 4×8-bit LVDS ports
Clock Source	Centallax: TG1C1A Clock Synthesiser	• Frequency Range: 0.5 – 13.5 GHz • Accuracy: ±3.0 ppm • 6 differential output channels • Sub-rate trigger output: (Clock/N)

3.4.2 DSP Design Environment

MATLAB™ and Simulink™ provide a comprehensive DSP system modelling and simulation environment with graphical user interface (GUI) for building hierarchical system models. Models are constructed from component toolboxes which are comprehensive libraries of fundamental building blocks. Simulink supports modelling and simulation in discreet-time for compatibility with digitally sampled logic. Multi-rate systems are also supported such as in the case of a multiple clock logic system. The environment allows rapid evaluation of different designs and model verification can be performed at different levels. Altera's DSP Builder™ is a design toolbox that integrates with Simulink™ to provide a library of circuit elements from which designs can be directly compiled into a hardware description language (HDL) such as Verilog or VHDL, VHDL is employed in this case.

Individual functions are first designed in Simulink with DSP Builder™ library elements. Initial design verification is then performed by addition of suitable test circuitry for test pattern generation and output data analysis and display, for example Vector Scopes can be used to view constellation diagrams. The Simulink™ design is simulated to verify operation and can be rapidly modified to evaluate alternative logic designs. Once the design is verified in Simulink™ a version, without the additional test circuitry, is compiled to generate a VHDL representation of the design. It should be noted that VHDL generation from DSP Builder™ models does not result in highly optimised logic, in terms of silicon area or power consumption, compared to direct coding in VHDL. However, for the proof-of-concept purpose logic optimisation is not critical unless required for enhancing processing performance.

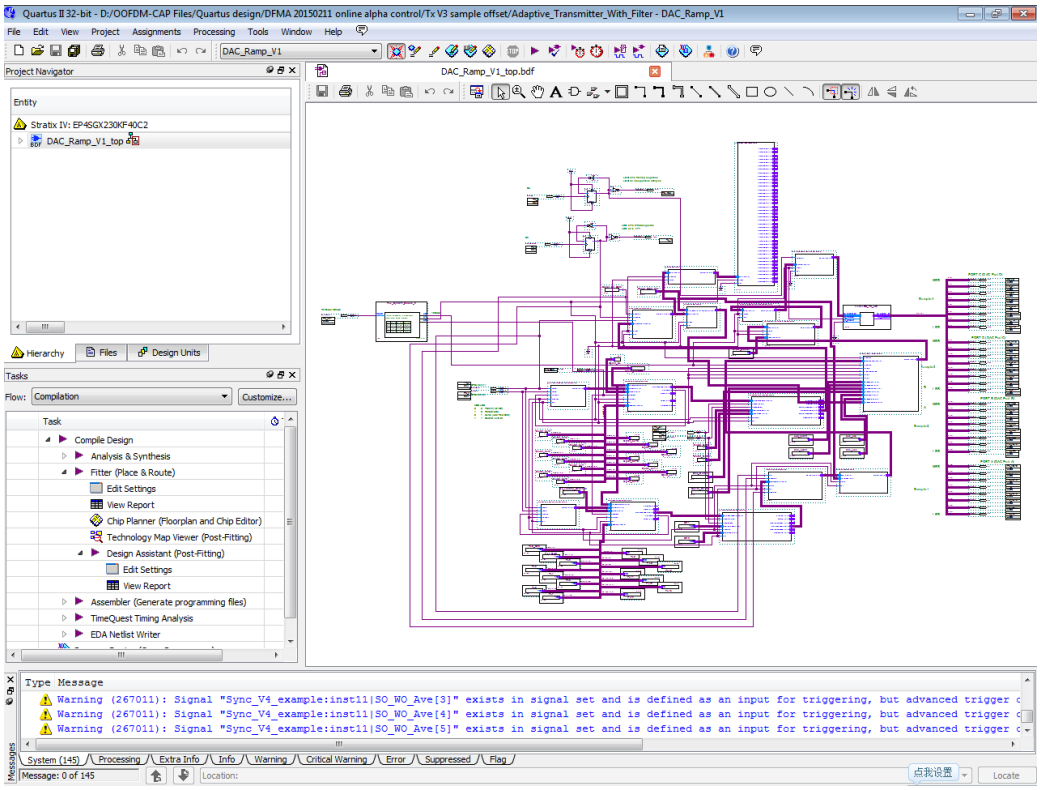

Fig. 3.10 Quartus II Design Environment

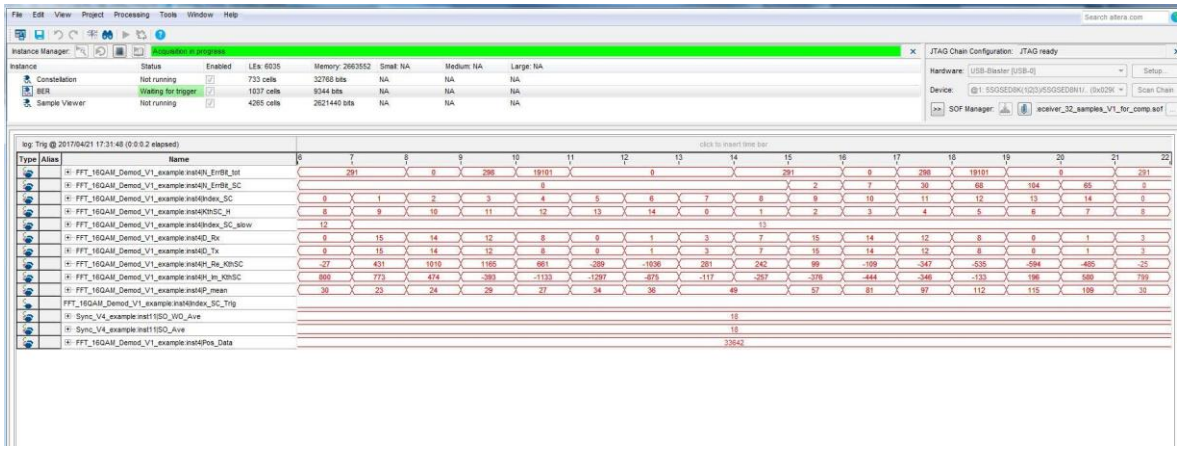

Fig. 3.11 Performance monitoring with Signal Tap II Embedded Logic Analyser

Quartus II™ is Altera's FPGA design software which provides a comprehensive FPGA design environment, which is shown in Fig. 3.10. System designs are constructed by integrating multiple VHDL-based functional blocks, in this case created in Simulink™ with DSP Builder™. The complete design is then synthesised to generate a netlist based on primitive logic gates. The netlist is then fitted to the FPGA's logic array and fixed logic functions and the FPGA programming file generated. The Quartus II™ software incorporates an embedded logic analyser, SignalTap II™, which allows the state of predefined nodes to be probed during operation, this is used for design debugging purposes and to extract key system performance parameters during operation such as bit error counts and channel response. An example SignalTap II™ output is shown in Fig. 3.11. The Stratix IV GX FPGA also has embedded memory which can be incorporated into the design to store system parameters which can then be updated in real-time via the Memory Content Editor within Quartus II™. This feature is fully exploited to enable the rapid online optimisation of various system parameters which directly impact system performance. In addition, it is also used to change the filter coefficients in real-time to select the received channel, thus this feature is used to make the transceiver real-time reconfigurable.

3.4.3 Overall DSP architecture for reconfigurable transceiver

Figure 3.12 shows the FPGA-based digital orthogonal filter DSP architectures incorporated in the real-time transmitter (top) and the real-time receiver (bottom). In the transmitter FPGA, two independent digital OFDM channels with adaptive transmission performance are generated using two separate OFDM DSP sub-systems identical to those previously published in [7, 8]. The OFDM generation procedure consists of the following major

functions: 96-bit word pseudo-random binary sequence (PRBS) test data generation, pilot-tone insertion, bit and/or power loading-enabled on-line adaptive modulation of 15 data-carrying subcarriers with modulation formats selected from 16-QAM, 32-QAM or 64-QAM, 32-point inverse fast Fourier transform (IFFT) for producing real-valued OFDM time-domain symbols, on-line adaptive signal clipping, 8-bit sample quantization and addition of 25% cyclic prefix to each symbol. 40×8-bit parallel OFDM samples contained within each individual OFDM symbol are produced at a rate of 25M symbols/s per digital OFDM channel. The OFDM sub-systems thus operate in a 25MHz clock domain, as indicated in Fig. 3.12.

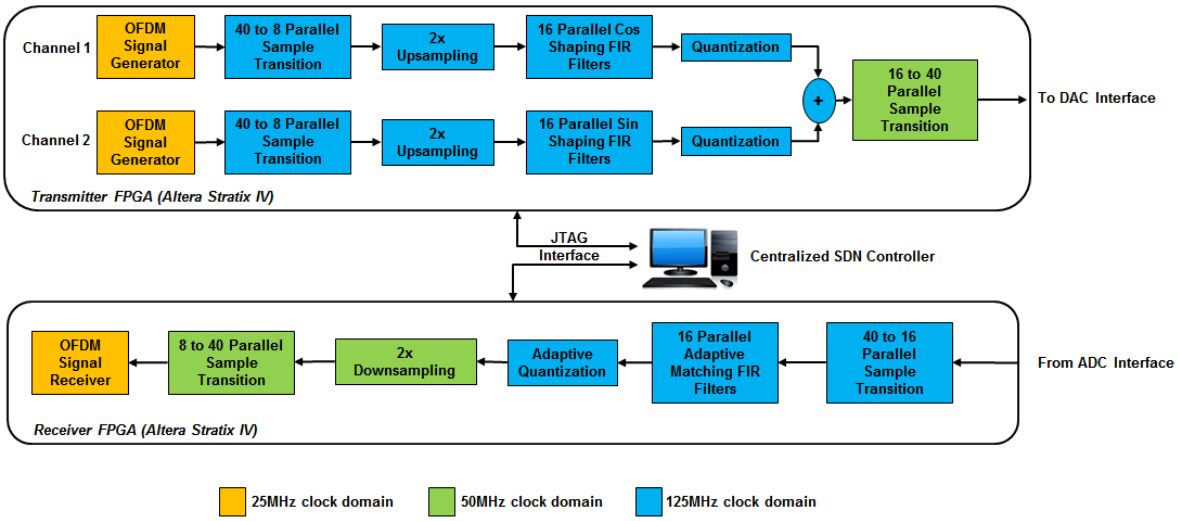

Fig. 3.12 FPGA-based real-time software reconfigurable digital orthogonal filter DSP architectures implemented in the transmitter and receiver.

To significantly reduce the FPGA logic resource usage for the digital filtering, each digital OFDM symbol is transformed from 40 parallel samples clocked at 25MHz to 8 parallel samples clocked at 125MHz, as shown in Fig. 3.12. The digital filters thus operate in a 125MHz clock domain. To achieve the channel multiplexing, each OFDM channel is first up-sampled by a factor of M=2 by inserting a zero-valued sample between two successive samples, thus doubling the samples per symbol and sample rate to 80 and 2GS/s, respectively. The oversampled channel then passes through a bank of parallel 32-tap finite impulse response (FIR) digital shaping filters, where filter coefficients are signed 8-bit values, as illustrated in Fig. 3.13. Here parallel filters are needed as the FPGA cannot run at 2GHz. The generation of 16 parallel samples at 125MHz thus achieves the required sample throughput of 2GS/s. For the two-channel case considered here the zero-valued samples are

not actually inserted in the logic design before the FIR filters, as the FIR filters operate on parallel samples it is unnecessary to include tap coefficient multipliers for the zero-valued input samples. Also, due to the employed filter coefficients, a feature of the filter output signal, unique to the 2 channel case, is that every other output sample is zero-valued, thus only 8 parallel FIRs are required to generate the 16 parallel output samples. The zero-valued samples are therefore inserted at the output of the filters. After applying 8-bit quantization to each filtered channel, the two digitally filtered channels are then directly summed. Subsequently a 16 to 40 parallel sample transformation is performed and the clock rate is converted from the 125MHz clock domain to a 50 MHz clock domain, as shown in Fig. 3.12. The summed channels are then sent to the DAC interface which feeds an 8-bit DAC operating at 2GS/s, finally a 1GHz bandwidth analogue signal is generated.

Based on the continuous time filter responses defined in Eq. 3.4 the two discrete impulse responses are:

$$\begin{matrix} s_1(k)=g(k)\cos(2\pi f_c k T_s) \\ s_2(k)=g(k)\sin(2\pi f_c k T_s) \end{matrix} \tag{3.10}$$

where k = 0, 1, 2, …, 31, f_c = 500MHz is the central frequency of the filter pair, and T_s = 500ps is the sampling time interval. Based on Eq. 3.5, here $g(k)$ is the discrete and causal baseband pulse expressed as:

$$g(k) = \frac{\sin[\pi(1-\alpha)k'] + 4\alpha k' \cos[\pi(1+\alpha)k']}{\pi k'[1-(4\alpha k')^2]} \qquad , k' = \frac{k-16}{M} \tag{3.11}$$

Here α = 0 is adopted to maximize the aggregated signal transmission capacity, and the up-sampling factor M = 2. The discrete impulse responses and associated discrete frequency responses for these two shaping filters are shown in Fig. 3.13. Throughout this section, the in-phase channel, $s_1(k)$, is termed Channel 1 and the quadrature-phase channel, $s_2(k)$, is referred to as Channel 2.

The properties of the digital shaping filters worth highlighting are listed below:

- The 2× up-sampling generates a mirrored signal spectrum within the Nyquist band, such that the n-*th* subcarrier generates two images at n × f_c and (32-n) × f_c, where f_c =31.25MHz is the subcarrier spacing.

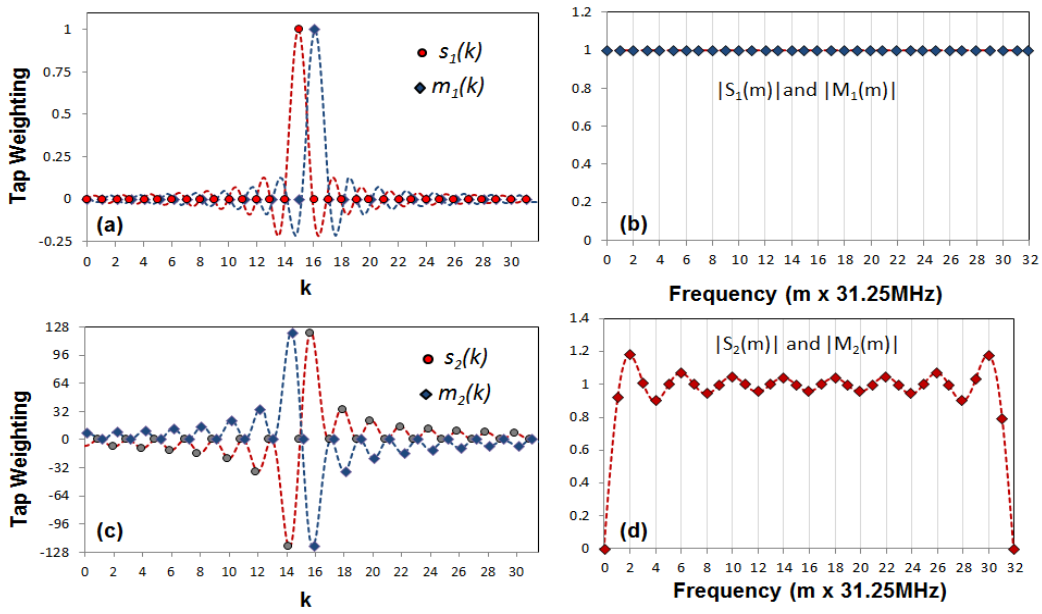

Fig. 3.13. Discrete impulse and frequency responses of the shaping and matching filters. (a) Impulse responses of Channel 1. (b) Frequency responses of Channel 1. (c) Impulse responses of Channel 2. (d) Frequency responses of Channel 2. Figures (b) and (d) are plotted at frequency intervals equal to the subcarrier spacing, m represents the discrete frequency index. Equivalent continuous responses are also shown as dotted lines.

- Only 8 parallel FIR filters clocked at 125MHz are used to generate 16 parallel samples, as every other output sample is 0.
- The in-phase FIR shaping filter has one non-zero co-efficient of 1 only and does not require rescaling or quantization, whereas the quadrature-phase FIR filter has signed 8-bit coefficients and thus requires sample re-quantization to signed 8-bit values.

In the receiver FPGA, to extract a desired channel, the 40 parallel samples at 50MHz, from the ADC interface, are first transformed to 16 parallel samples at 125MHz and then fed into the software controlled digital matching filter. The resulting 16 parallel samples are then down-sampled by a factor of 2 by selecting every other sample. The resulting 8 parallel samples are then transformed to 40 parallel samples. Similar sample bus width conversions and clock domains, as used in the transmitter, are also employed but with the signal flow in the opposite direction. The coefficients of the matching filter are dynamically configured to implement one filter from a Hilbert-pair. Based on Eq. 3.6, the discrete impulse responses of the selectable matching filters are written as:

$$\begin{matrix} m_1(k)=s_1(31-k) \\ m_2(k)=s_2(31-k) \end{matrix} \quad (3.12)$$

satisfying Eq. 3.3 as:

$$s_i(k) \otimes m_j(k) = \begin{cases} \delta(k-k_0) & i=j \\ 0 & i \neq j \end{cases} \quad (3.13)$$

where k_0 corresponds to the total discrete time delay induced by both filters. The matching filters' impulse responses and frequency responses are also presented in Fig. 3.13. To extract Channel 1 and Channel 2, the taps are configured for $m_1(k)$ and $m_2(k)$, respectively. Also as the filter tap selection effects the output signal scaling, the quantization block's parameters are also set appropriately for the selected filter. Therefore, online adaptation of the FIR tap values of these shaping and matching filters can enable software-controllable channel add/drop without requiring extra discreet hardware.

After the matching filter and 8-bit sample quantization in the 125MHz clock domain, 8 to 40 parallel sample transformation to a 25MHz clock domain allows the channel to then be processed by the receiver OFDM DSP functions similar to those reported in section 2.3.1.2. The functions include: detection of pilot-subcarriers and channel estimation, automatic symbol alignment and cyclic prefix removal, 32-point FFT for generating complex-valued frequency domain subcarriers from the received real-valued time domain symbols, channel equalization, on-line adaptive demodulation of 15 data-carrying subcarriers and bit error rate (BER) analysis of total channel BERs and individual subcarrier BERs.

3.4.4 DSP Design and Implementation for Digital Orthogonal Filters

Fig. 3.14 shows the basic structure of a FIR filter. "Finite" indicates there is no internal feedback so the FIR filter's impulse response must be of a finite time duration. It is in contrast to the infinite impulse response (IIR) filter. In Fig. 3.11 $C(n)$ $(n = 1,2,3 \dots N)$ represents the *n*-th coefficient of the filter and the coefficients are derived from the desired filter impulse response. The filter has N taps requiring N multipliers. Fewer taps can therefore reduce filter design complexity but limiting to a finite number of taps can also affect the filter frequency response characteristics. Therefore there is an optimum number of taps to minimise complexity whilst still achieving suitable filter performance. If $x(n)$ are

input samples and $y(n)$ are output samples, each value of the output samples is a weighted sum of the most recent input values expressed as:

$$y(n) = \sum_{i=1}^{N} C(i)x(n-i+1) \tag{3.14}$$

Eq. 3.14 shows that $y(n)$ is the convolution of $x(n)$ and $C(n)$.

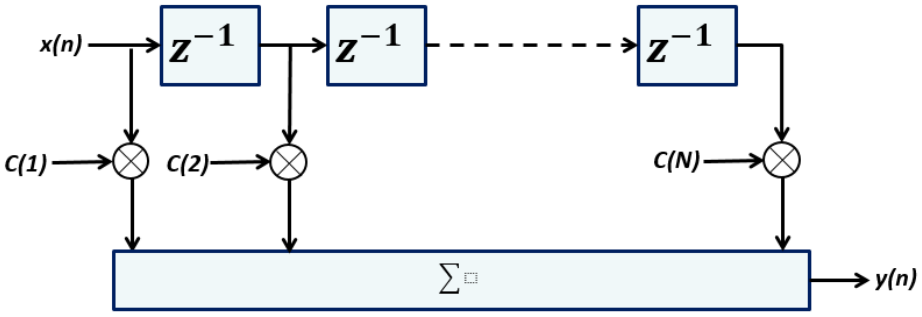

Fig. 3.14 FIR filter structure

As seen in section 3.4.3, the biggest technical challenge in software reconfigurable transceiver DSP design is the implementation of high-speed parallel digital orthogonal filters supporting GS/s throughputs due to the limitation of FPGA operating clock frequencies. There are two implementation methods for FIR filters: time-domain and frequency-domain. Generally speaking, frequency-domain implementation is more computationally complex than a time-domain FIR filters for small filter order, whilst for higher filter order (>60) the frequency-domain implementation becomes computationally more efficient than the time-domain implementation [9]. Therefore, considering the low filter order digital filter utilised in the dissertation research, time-domain implementation is chosen for the filter design throughout the thesis. Fig 3.15 illustrates the 32-tap FIR filter employing a parallel architecture. It has two main stages: i) sample delay stage and ii) parallel FIR filtering stage. The design also includes a 32-tap filter coefficients selection block which allows on-line selection of different pre-set filter coefficients.

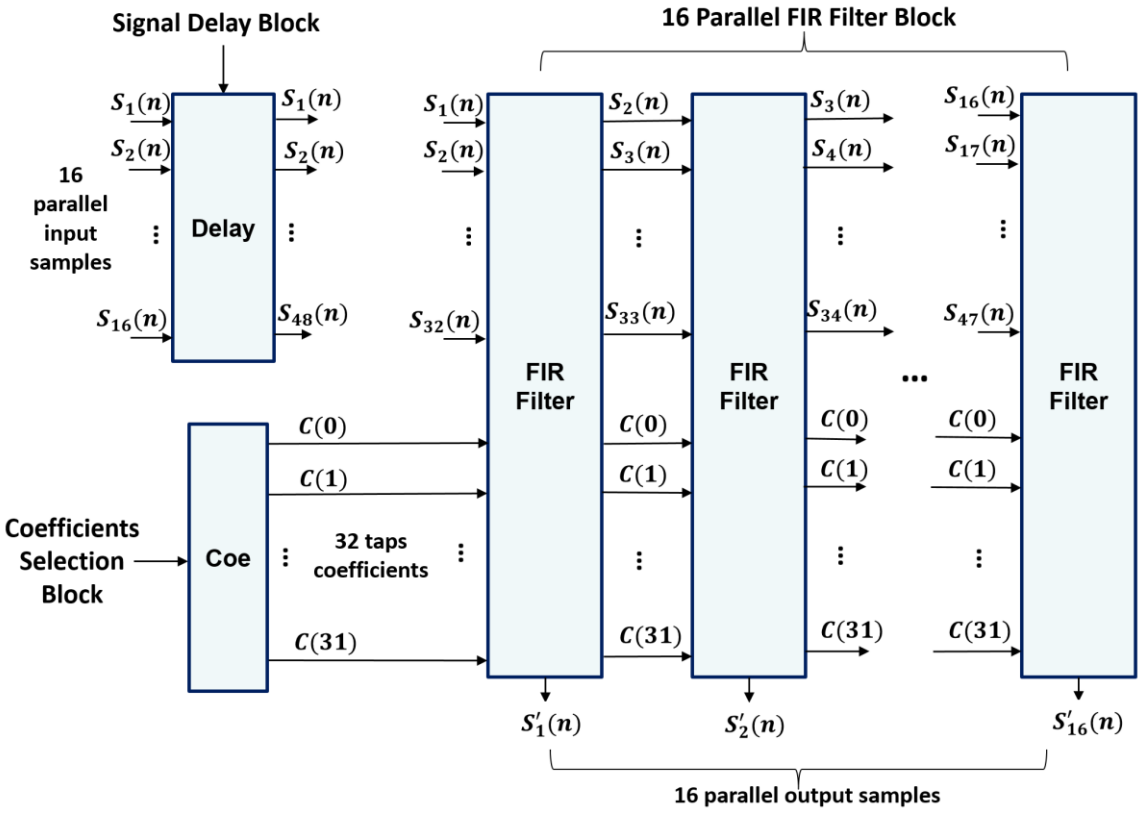

Fig. 3.15 32-tap parallel FIR filter block

The first stage is shown in Fig. 3.16. There are two delay blocks each giving one sample delay to the parallel input samples, so the total number of output parallel samples from the signal delay stage is 48. The reason to generate 48 parallel samples after the signal delay stage is that the input parallel 16 samples in Fig. 3.15 need to be fed to 16 parallel 32-tap digital filters, so each digital filter deals with 32 parallel input samples, there is one sample delay needed between each group of 32 parallel input samples for each filter, therefore there are 16+32=48 parallel samples needed in total for the 16 parallel digital filters. These parallel samples are then fed to the second stage. The output of the *p*-th parallel FIR filter in the *n*-th group of parallel output samples is given by:

$$S'_p(n) = \sum_{i=0}^{31} S_{p+i}(n)C(31-i), \quad p = 1,2,3,\ldots,16 \tag{3.15}$$

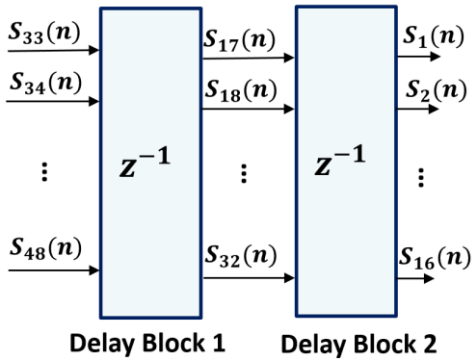

Fig. 3.16 Signal delay block

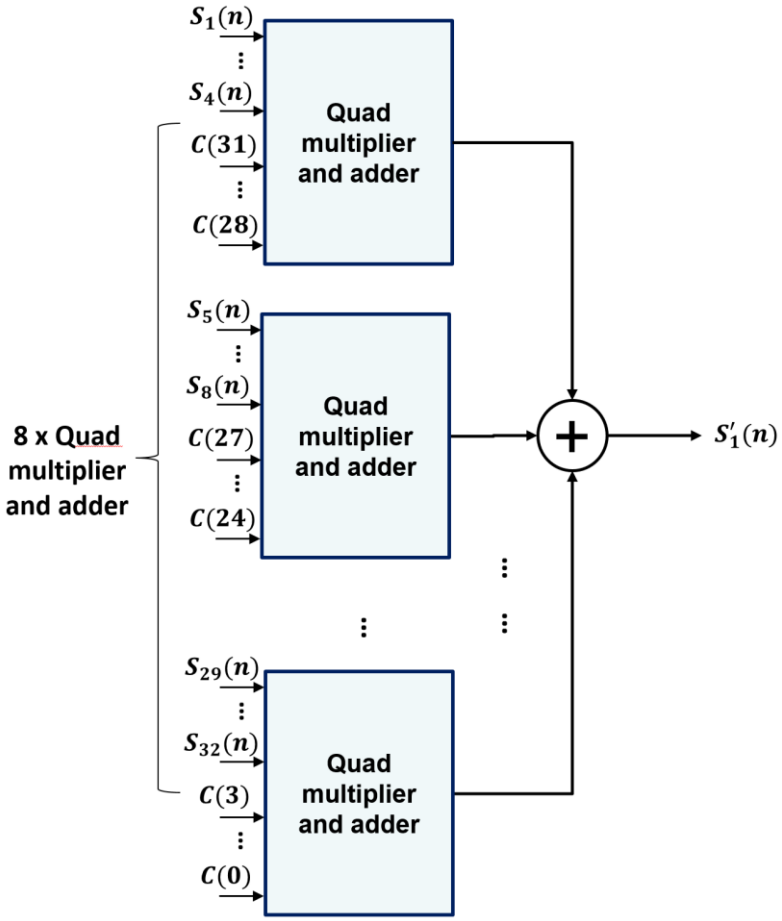

Fig. 3.17 FIR filtering block

The second stage consists of 16 parallel filter blocks, and the detailed structure of each block is presented in Fig. 3.17. Here the 1-st parallel FIR filter utilising 8 quad multiplier and adder blocks is shown in the figure as an example without loss of generality. According to the FIR filter theory and Eq. 3.15, the convolution is performed of 4 parallel input samples with 4 coefficients by multiplying the samples with the coefficients and summing the products in

each quad multiplier and adder. After that the outputs of the 8 quad multiplier and adder blocks are finally summed to produce the output of one FIR filter block.

Here it is worth pointing out that, in a practical implementation the filter design complexity can be reduced if there are zero valued coefficients and the fact that up-sampling introduces zero valued samples, thus multipliers can be eliminated when one input is zero. In addition, as the impulse responses of filters are symmetric, further reduction in multiplier count can be achieved by adding/subtracting input samples that employ the same coefficient value and using a single multiplier.

3.4.5 Real-Time Experimental System Setup

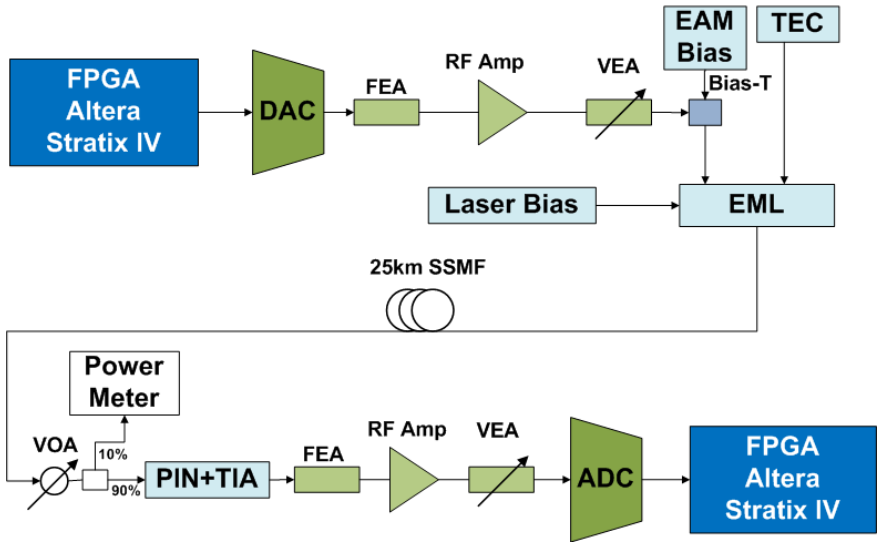

Fig. 3.18. Real-time experimental system setup.
FEA: fixed electrical attenuator, EML: electro-absorption modulated laser, VOA: variable optical attenuator, PIN+TIA: photodetector with integrated transimpedance amplifier.

Table 3.3 Experimental transceiver and system parameters

Parameter	Value
Total number of IFFT/FFT points per channel	32
Data-carrying subcarriers per channel	15

n-th subcarrier frequency	n×31.25MHz
Adaptive modulation formats on all subcarriers	16-QAM, 32-QAM, 64-QAM
DAC & ADC sample rate	2GS/s
DAC & ADC resolution	8 bits
Symbol rate	50MHz
Samples per symbol (IFFT)	32 samples (16ns) #
Cyclic prefix	8 samples (4ns) #
Total samples per symbol	40 samples (20ns) #
Error count period	88,500 symbols (7965000bits)
EML laser wavelength	1550nm
3-dB EML modulation bandwidth	10GHz
Laser bias current	124mA
EAM bias voltage	-0.7V
EML driving voltage	320mVpp
PIN detector bandwidth	12.4GHz
PIN detector sensitivity	-19dBm*

Before up-sampling and after down-sampling

* Corresponding to 10 Gb/s non-return-to-zero data at a BER of 1.0×10^{-9}

Figure 3.18 shows the complete real-time experimental system setup with key system parameters listed in Table 3.3. In the transmitter, the DAC converts the 8-bit digital samples at 2GS/s to a 1GHz bandwidth analogue signal. An RF amplifier and a variable electrical attenuator (VEA) set the optimum RF signal voltage to $320mV_{pp}$ for combination, via a bias-T, with an optimum DC bias of -0.7V. The resultant RF signal intensity modulates a 10 GHz electro-absorption modulator (EAM) within an EML. The 1550nm DFB laser in the EML is driven with a 124 mA bias current. The EML's optical output is launched at an optical power of 2.5 dBm into a 25km SSMF IMDD system.

At the receiver, the received optical signal first passes through a variable optical attenuator (VOA) for control of the received optical power (ROP) level, then a 12.4GHz PIN+TIA performs the optical-electrical conversion of the received optical signal. The analogue electrical signal level is always optimized to occupy the full-scale input range of the 8-bit ADC operating at 2GS/s. A RF delay line (not shown in Fig. 3.18) is also utilised before the ADC to adjust the receiver sample timing. The digitized samples are processed by the ADC interface in the receiver FPGA to generate sequences of 40 parallel samples.

On-line performance monitoring of the receiver-measured BERs, system frequency responses and subcarrier constellations is achieved through the FPGA's embedded logic analyzer function. This allows instant analysis of the system transmission performance which, combined with the on-line control of the transmitter DSP parameters, RF gain, EML operating conditions and optical launch power, provides rapid optimization of the overall system performance. Here it is also worth emphasizing the following two aspects:

- Both channels could be recovered simultaneously in the same FPGA by implementing separate instances of the two matching filters and using two OFDM receiver functions;
- System synchronization and equalization are performed using the approaches reported in [7, 8].

3.4.6 Experimental Results

For both the in-phase channel, Channel 1, and the quadrature-phase channel, Channel 2, their effective frequency responses measured from the transmitter IFFT input to the receiver FFT output and normalized to the corresponding first subcarrier powers for the considered 25km SSMF IMDD system are plotted in Fig. 3.19, where, in comparison with those reported in [7], significantly flattened effective frequency response are observed. The considerable reductions in channel frequency response roll-off are mainly attributed by the up-sampling-induced spectral mirroring effect, which causes the signal conveying both channels to occupy two equal 0.5GHz spectral regions with respect to the half of the Nyquist frequency of 1 GHz, as seen in Fig. 3.20. As a direct result, uniform subcarrier power loading profiles are adopted in all the experimental measurements presented throughout the chapter.

As theoretically predicted in [1], Fig. 3.19 shows that the low tap count-induced frequency response ripples of the quadrature-phase channel, Channel 2, are much higher than those corresponding to the in-phase channel, Channel 1, and that for each channel, compared to high frequency subcarriers, the ripples for low frequency subcarriers are more pronounced. Together with the strong unwanted intermixing frequency products generated upon square-law photon detection in the receiver, the large ripples seen by the low frequency subcarriers play an important role in determining the occurrence of excessive errors on these subcarriers. As a consequence the first 5 subcarriers of Channel 2 must be dropped to allow acceptable BER levels to be obtained. This also results in the adaptation of low signal modulation formats on low frequency subcarriers of Channel 1, when adaptive bit loading is applied, as shown in Fig. 3.21. Compared to the frequency response of the in-phase channel, the up-shifted frequency gain response of the quadrature-phase channel in Fig. 3.19 is a direct result of the normalization operation, as a relatively low power for the first subcarrier occurs in the quadrature-phase channel, as seen in Fig. 3.13(d).

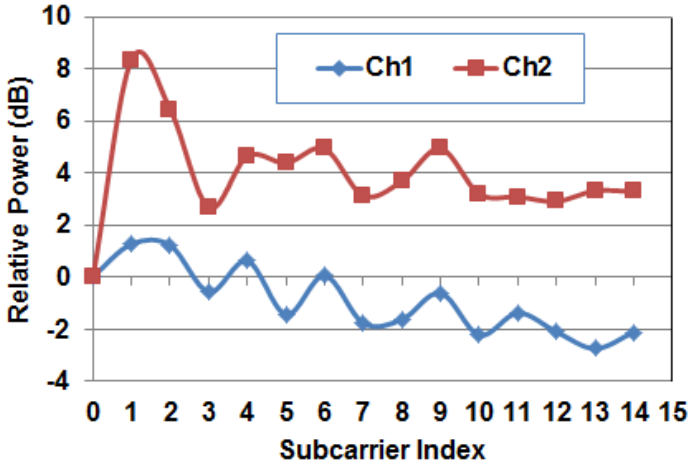

Fig. 3.19. Channel frequency responses for both the in-phase channel, Channel 1 and the quadrature-phase channel, Channel 2. The responses are normalized to the first subcarrier power of each corresponding channel and measurements are undertaken from the transmitter IFFT input to the receiver FFT output after transmitting through the 25km SSMF IMDD system.

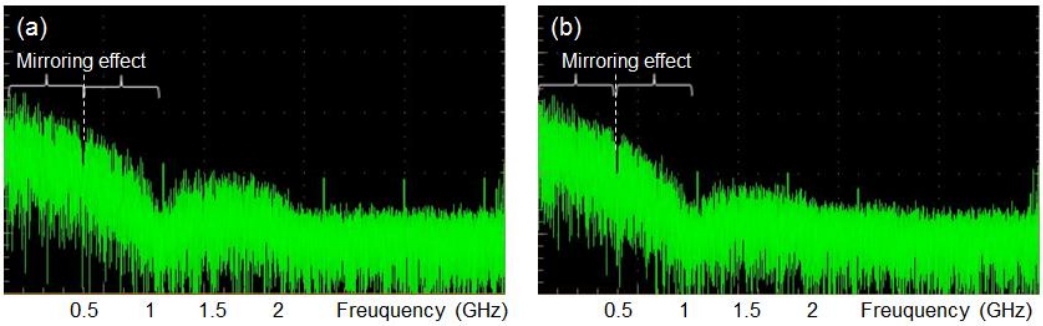

Fig. 3.20. Spectra of the electrical signal conveying both the in-phase and quadrature-phase channels. (a) Measured after DAC in the transmitter. (b) Measured before ADC in the receiver.

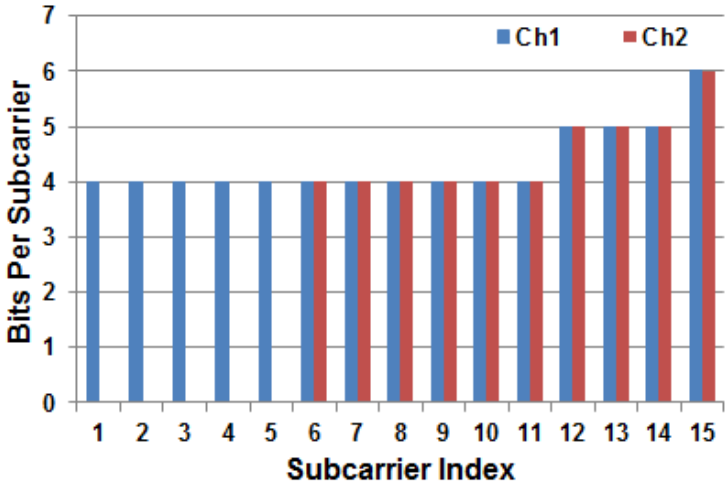

Fig. 3.21. Optimum bit loading profiles for both in-phase and quadrature-phase channels. Their corresponding subcarrier power loading profiles are uniform.

With all the employed subcarriers of each channel set at 16-QAM and reduced frequency response roll-off-enabled uniform subcarrier power loading profiles, the optimum transceiver and system parameters presented in Section 3.4.5 result in a raw line rate of 1.875Gb/s for the in-phase channel, Channel 1, and 1.25Gb/s for the quadrature-phase channel, Channel 2, thus the transmissions of an aggregate raw signal line rate of 3.125Gb/s is achievable over the 25km SSMF IMDD system. Under the simultaneous presence of both channels, the BER performances against received optical power (ROP) for both optical back-to-back (OBTB) and 25km SSMF are plotted in Fig. 3.22 (a), where similar BER performances are shown for both channels. At the forward error correction (FEC) limit of 1.0×10^{-3} (this is selected as a low FEC overhead is preferred. Generally speaking, a higher FEC limit will increase the FEC overhead.), for both channels considered here, the adopted low digital filter tap count plays a dominant role in determining the occurrence of the 0.6 dB power penalties observed in Fig. 3.22 (a), which can, however, be reduced when use is made of adaptive bit loading, as indicated in Fig. 3.22 (b). In addition, in comparison with the quadrature-phase channel, for the in-phase channel, both the higher transmission capacity and its' corresponding lower ROP at the adopted FEC limit is due to the fact that the in-phase channel has an intrinsic flat frequency response, as shown in Fig. 3.13 (b). In addition, it is noted that, comparing with the simulation results in section 3.3, the ROP at FEC limit of 1×10^{-3} after 25km SSMF transmission for both channels are higher in the experiment than those in the simulation. This is attributed by the following effects that are neglected in the simulation however are non-negligible in the experiment: i) EML nonlinearity , ii) channel frequency response roll-off, iii) RF component distortions and noise, and iv) non-ideal sample timing.

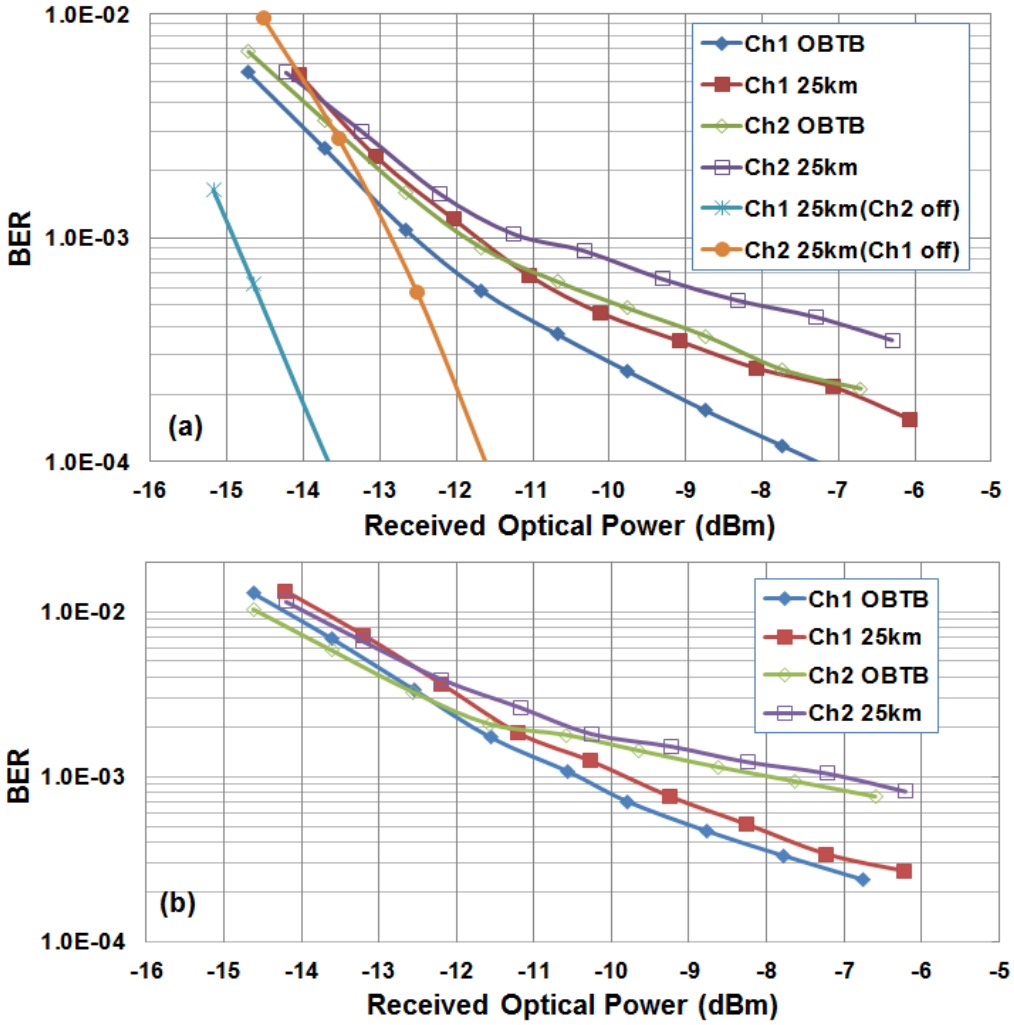

Fig. 3.22. BER performances as a function of received optical power. (a) Identical signal modulation formats of 16-QAM are taken on all the subcarriers of each channel. (b) Adaptive bit loading is applied for the subcarriers of each channel. The optimum bit loading profile is shown in Fig. 3.20. Uniform power loading profiles are adopted for all the cases.

To explore the transceiver's channel reconfigurability and its' relevant impacts on system BERs performance, Fig. 3.22(a) also presents the 25km SSMF system BER performance of each channel with the other channel switched off in the digital domain whilst all other transceiver/system parameter settings are unchanged. It is shown in Fig. 3.22(a) that, at the adopted FEC limit, the channel multiplexing/demultiplexing operation imposes an approximately 3dB (2dB) ROP variation for the in-phase (quadrature-phase) channel. Such a channel ROP variation can almost be eliminated when adaptive bit loading is adopted. The adaptive bit loading-induced elimination in ROP variation, however, brings about approximately 25% reductions in the maximum achievable channel transmission capacities. Furthermore, in comparison with the cases where two channels are present simultaneously,

the transmission of a single channel gives rise to sharp BER developing curves, as shown in Fig. 3.22(a). This implies that the cross-talk effect between these two channels is the major physical mechanism underlying the minimum achievable BERs of the systems.

Under the condition of both channels being present simultaneously, the adaptive bit loading-induced transceiver adaptability is experimentally explored in Fig. 3.22(b), where the BER versus ROP performance of each individual channel is plotted, in obtaining which the transceiver and system operating conditions identical to those adopted in Fig. 3.22(a) are considered, except that adaptive bit loading is applied on all the subcarriers of each channel. In carrying out adaptive bit loading, the highest possible signal modulation format is always selected first on the highest possible frequency subcarriers (as they exhibit better SNR performance than the lower frequency ones) to ensure a maximum total transmission capacity achieved under the condition that the total BER is still below the FEC limit of 1×10^{-3}. As the discussions of the channel multiplexing/demultiplexing operation-induced ROP variations have already been made in Fig. 3.22(a), in Fig. 3.22(b) special attention is, therefore, focused on the use of adaptive bit loading to further improve the channel transmission capacity and simultaneously reduce the associated power penalty. The optimum bit loading profiles are illustrated in Fig. 3.21, which gives rise to 2.03Gb/s for the in-phase channel, 1.41Gb/s for the quadrature-phase channel and an aggregated signal capacity of 3.44Gb/s for the entire 25km SSMF IMDD transmission system. It is shown in Fig. 3.22(b) that, compared to Fig. 3.22(a), adaptive bit loading can not only increase the aggregated transmission capacity by approximately 10%, but also considerably reduce the corresponding power penalty for each channel. This indicates that it is feasible to employ adaptive modulation to combat the impairments associated with low-complexity digital filter DSP designs.

After 25km SSMF IMDD transmissions and for the minimum BERs shown in Fig. 3.22(b), example constellations of 16-QAM, 32-QAM and 64-QAM-encoded subcarriers of both channels are presented in Fig. 3.23, which are recorded prior to performing channel equalization in the receiver. The existence of the clean constellations of higher modulation formats on higher frequency subcarriers indicates that, for the adopted synchronization and equalization approaches, both the IMDD system frequency response roll-off and the symbol timing offset/jitter are not the major physical factors limiting the maximum achievable system transmission performance for the adopted experimental conditions. This verifies the

theoretical predications in section 3.3. Furthermore, in comparison with the signal modulation format-dependent traditional CAP systems [1], the feasibility of utilizing various signal modulation formats for a fixed digital filter DSP design is also demonstrated in Fig. 3.23. This implies that the transceivers can be made transparent to underlying modulation technologies.

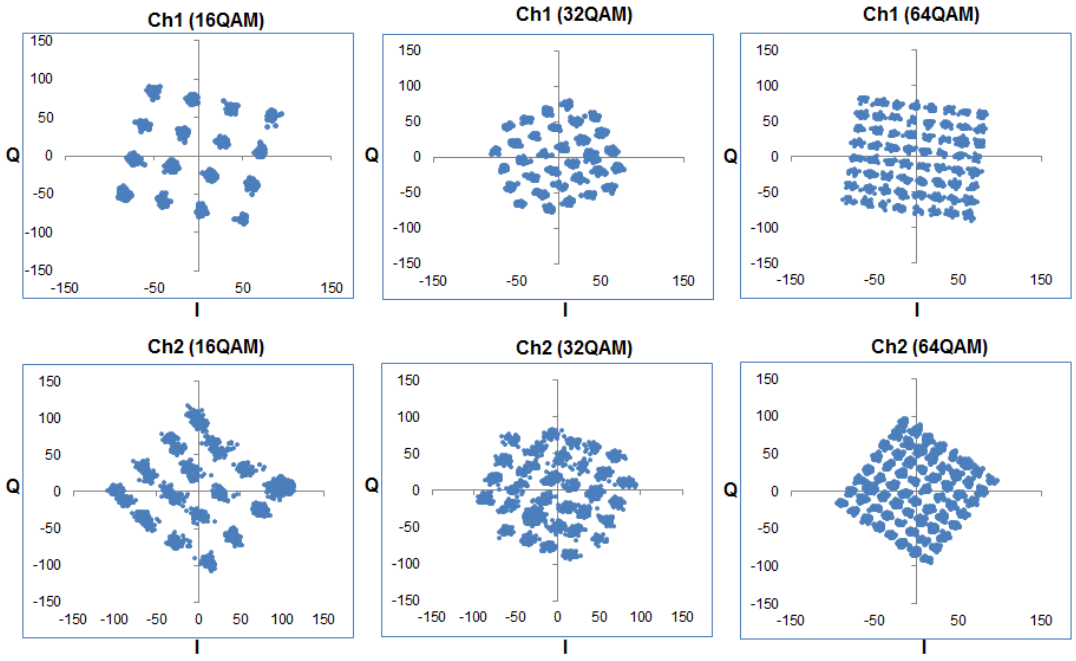

Fig. 3.23. Example received subcarrier constellations before channel equalization in the receiver for both channels.

3.5 Conclusion

Software reconfigurable optical transceivers utilising digital orthogonal filters are firstly theoretically investigated. Impacts of major transceiver design aspects including the number of digital filter taps and different modulation formats on the transmission performance are explored in an IMDD SSMF system consisting two digital orthogonal filtering-based channels using OFDM modulation. Numerical simulation results show that 32 taps achieve a good trade-off between performance and DSP complexity and it was demonstrated that different modulation formats ranging from 16-QAM to 256-QAM can be supported. Secondly, real-time reconfigurable transceivers with on-line software-controllable channel reconfigurability and transmission performance adaptability are also experimentally

demonstrated utilizing Hilbert-pair-based 32-tap digital orthogonal filters implemented in FPGAs. By making use of a 2GS/s@8-bit DAC/ADC, an oversampling factor of 2 and an EML intensity modulator, the demonstrated RF conversion-free transceiver supports end-to-end real-time simultaneous adaptive transmissions, within a 1GHz signal spectrum region, of a 2.03Gb/s in-phase OOFDM channel and a 1.41Gb/s quadrature-phase OOFDM channel over a 25km SSMF IMDD system. In addition, experimental explorations have also been undertaken of the key physical mechanisms limiting the maximum achievable transmission performance, impacts of transceiver's channel multiplexing/demultiplexing operations on the system BER performance, and the feasibility of utilizing adaptive modulation to combat impairments associated with low-complexity digital filter DSP designs. Furthermore, experimental results have also indicated that the transceiver incorporating a fixed digital orthogonal filter architecture can be made transparent to various signal modulation formats of up to 64-QAM.

References

[1] M. Bolea, R. P. Giddings, and J. M. Tang, “Digital orthogonal filter-enabled optical OFDM channel multiplexing for software-reconfigurable elastic PONs,” *J. Lightwave. Technol.,* vol. 32, no. 6, pp. 1200-1206, 2014.

[2] G. H. Im, D. D. Harman, G. Huang, A. V. Mandzik, M. H. Nguyen, and J. J. Werner, “51.84 Mb/s 16-CAP ATM LAN standard,” *IEEE J. Select. Areas Commun*., vol. 13, no. 4, pp. 620–632, May 1995.

[3] M. I. Olmedo, T. J. Zuo, J. B. Jensen, Q. W. Zhong, X. G. Xu, I. T. Monroy, “Towards 400GBASE 4-lane Solution Using Direct Detection of MultiCAP Signal in 14 GHz Bandwidth per Lane,” in *Optical Fiber Communication Conference (OFC),* Anaheim, 2013, paper PDP5C.10.

[4] J. L. Wei, J. D. Ingham, R. V. Penty, and I. H. White, "Update on performance studies of 100 gigabit ethernet enabled by advanced modulation formats," *presented at IEEE Next Generation 100G Optical Ethernet Study Group, Geneva, Switzerland*, Sept. 2012.

[5] R. Rodes, M. Wieckowski, T. T. Pham, J. B. Jensen, J. Turkiewicz, J. Siuzdak, and I. T. Monroy, “Carrierless amplitude phase modulation of VCSEL with 4 bit/s/Hz spectral efficiency for use in WDM-PON,” *Opt. Exp* vol. 19, no. 27, pp. 26551-26556, 2011.

[6] J. M. Tang and K. A. Shore, “30-Gb/s signal transmission over 40-km directly modulated DFB-laser-based single-mode-fiber links without optical amplification and dispersion compensation,” *J. Lightw. Tech.,* vol. 24, no. 6, pp. 2318–2327, Jun. 2006.

[7] R. P. Giddings, E. Hugues-Salas, and J. M. Tang, “Experimental demonstration of record high 19.125 Gb/s real-time end-to-end dual-band optical OFDM transmission over 25 km SMF in a simple EML-based IMDD system,” *Opt. Express.,* vol. 20, no. 18, pp. 20666–20679, 2012.

[8] X. Q. Jin, J. L. Wei, R. P. Giddings, T. Quinlan, S. Walker, and J. M. Tang, "Experimental demonstrations and extensive comparisons of end-to-end real-time optical OFDM transceivers with adaptive bit and/or power loading," *IEEE Photonics Journal*., vol.3, no. 3, pp. 500–511, 2011.

[9] H. Johansson and O. Gustafsson, "On Frequency-Domain Implementation of Digital FIR Filters," in *IEEE International Conference on Digital Signal Processing (DSP)*, Singapore, 2015, pp. 315-318.

4. DSP-Enabled Flexible ROADMs

Contents

4.1 Introduction

In the previous chapter, we have proposed and investigated a novel software reconfigurable optical transceiver. Meanwhile, as one of the most important networking devices offering fast connectivity between an expanded number of individual optical networks, cost-effective reconfigurable optical add/drop multiplexers (ROADMs) with simplified architectures and more flexible functionalities will play a vital role in cost-sensitive CANs, via a technical strategy of significantly reducing both the capital expenditure (CAPEX) and the operating expenditure (OPEX) [1, 2]. Recently, a number of new ROADM architectures, mainly for long-haul optical backbone networks, have considerably advanced conventional ROADM operation functionalities in terms of colorlessness, directionlessness, contentionlessness and WDM-gridlessness [3-8]. However, due to their hard-wired switching element–induced operation limitations, those existing ROADMs can just operate at the wavelength level only. As such, their upgradability, flexibility and adaptability and switching granularity levels are significantly restricted for practical application in the CANs [9, 10]. On the other hand, given the great importance of dynamic operations of the CANs, SDN-controllable ROADMs are also highly desirable at wavelength, sub-wavelength and sub-band levels.

To cost-effectively deliver the abovementioned challenging ROADM operation features required by the CANs, by making use of Hilbert-pair-based orthogonal digital filtering, intensity modulation and passive optical coupling, we have recently proposed an optical-electrical-optical (O-E-O) conversion-free, software-switched ROADM capable of providing DSP-enabled dynamic and flexible add/drop operations at wavelength, sub-wavelength and orthogonal sub-band levels in simple IMDD-based optical network nodes [11]. To simplify the proposed ROADM architecture, the “drop-and-continue” feature [12, 13] is adopted. More recently a further simplified DSP-enabled novel ROADM architecture excluding both OTBPFs and O-E-O conversions has also been reported [14], in which all the unique ROADM operation features outlined in [11] are still maintained.

In this chapter theoretical simulations are first performed to explore and verify the technical feasibility of add and drop operations in the proposed ROADMs. After that, the ROADM experimental demonstrations are undertaken utilizing commercially-available, low-cost electrical/optical components. In addition, detailed experimental investigations are also

conducted of the ROADM add performance robustness to variations in differential optical power dynamic range and the ROADM drop performance robustness to drop RF signal power in IMDD-based optical network nodes. It is shown that the add and drop operation performances are independent of the sub-band signal spectral location, and that the maximum ROADM-introduced power penalties are just 1.8dB for the add operation and 1.2dB for the drop operation. In addition, for a fixed total received optical power as low as -12dBm after the add operation, the add operation can still tolerate a differential optical power dynamic range of >2dB. Whilst for the drop operation, an optical power penalty as low as 2dB is observed over a broad drop RF signal power variation range as large as 7.1dB. These experimental results suggest that the proposed ROADM has excellent performance robustness to major network operation parameter variations possibly encountered in practical network application scenarios.

4.2 Flexible ROADMs Operating Principle

Fig. 4.1 shows the schematic diagram of the proposed ROADM architecture fully supporting the SDN solution, the involved add and drop function elements are also illustrated in Fig 4.1. In the proposed ROADM, the input and output optical signals of each wavelength (in both east and west bounds) consist of multiple sub-wavelength bands at different RF frequencies. Each individual sub-wavelength band can have either two digital filtering-enabled spectrally-overlapped orthogonal sub-bands (an in-phase sub-band "I" and a quadrature-phase sub-band "Q") or a single sub-band (I or Q). For a specific optical carrier frequency, f_o, the optical signal containing n sub-wavelength bands can be expressed as:

$$s(t) = \sum_{i=1}^{n} \sum_{w=\{I,Q\}} y_i^w(t) e^{j2\pi f_o t} \tag{4.1}$$

where $y_i^w(t), (w = I \text{ or } Q)$ is the sub-band signal that is up-sampled and subsequently filtered by the corresponding I or Q component of the i-th orthogonal digital filters in the terminal equipment transceivers (TETs). The digital filters' central frequencies are located at f_{ci} (i=1, 2, 3, 4, …. n).

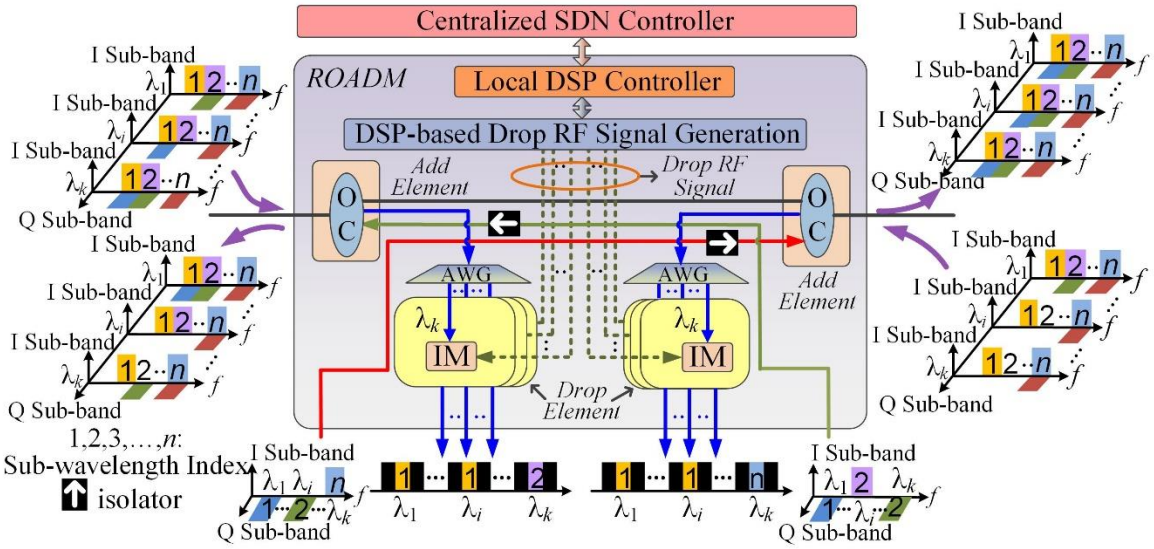

Fig. 4.1. Operating principles of the add and drop operations of the proposed ROADM. OC: optical coupler. 1, 2, 3,…n: sub-wavelength index.

As shown in Fig. 4.1, to drop a targeted sub-band signal conveyed by a sub-wavelength band of a selected wavelength, the wavelength containing the targeted sub-band is directly input to an IM driven by a SDN-controllable drop RF signal having a sinusoidal waveform, as seen in Fig. 4.1. The drop RF signal for the *w*-th sub-band and *i*-th sub-wavelength can be expressed as:

$$RF_i^w(t) = \begin{cases} Re\left\{\frac{1+ke^{j2\pi f_{ci}t}}{1+k}\right\} & ,\mathrm{w} = \mathrm{I} \\ Re\left\{\frac{1+ke^{j\left(2\pi f_{ci}t+\frac{\pi}{2}\right)}}{1+k}\right\} & ,\mathrm{w} = \mathrm{Q} \end{cases} \tag{4.2}$$

where k ($0<k<1$) is introduced to ensure that the drop RF signal amplitude varies within a dynamic range from 0 to 1. As the I and Q component of the *w*-th sub-band are orthogonal they effectively have a phase difference of $\pi/2$, this $\pi/2$ phase shift should be applied to the drop RF signal to select either the I or Q component in the drop operation as shown in Eq. (4.2). When both the frequency and phase of the drop RF signal match the targeted sub-band signal, the drop operation shifts the targeted sub-band to the baseband spectral region. At the IM output, the dropped sub-band with a reversed spectrum is shifted to the baseband spectral region, while all other sub-bands of the same wavelength are ruined and unrecoverable. As detailed in Section 4.3.2, after the direct detection of the dropped optical signal in a TET, a simple baseband digital low-pass filter suitable for use in all the drop operations can be utilized to separate the dropped signal from the ruined and unrecoverable sub-bands. A

relatively large k in Eq. (4.2) increases the optical signal power of the dropped sub-band [14].

As indicated in Eq. (4.2), by simultaneously using I and Q drop RF signals in two parallel drop function elements, the drop operation can also be conducted at sub-wavelength level. Moreover, to perform the drop operation at an entire wavelength level, k=0 can be taken to enable the IM to simply act as an optical passway.

Here it is worth addressing that, an alternative approach for the ROADM drop operation could involve splitting part of the signal power from the required optical wavelength, direct detection and A-D conversion of the entire band of channels and finally digital demultiplexing and frequency down-conversion of the targeted channel. To compare these two approaches, an IM is not needed in the alternative approach, however the big advantage of the IM-based approach over the alternative one is that the TET only needs to be working at the bandwidth of the dropped sub-band which is usually only between 1/100 to 1/10 of the aggregated wavelength channel in CANs. This means cheaper optical and electrical components with low-bandwidth can be used (particularly ADCs with lower sampling rate) in the TETs to significantly reduce the overall cost of the CANs.

On the other hand, in the add function element, similar to the procedure reported in [14], the add operation at a specific wavelength can be performed by passive optical coupling in an OC, as illustrated in Fig. 4.1. Such an operation can be expressed as:

$$|s_{out}(\mathrm{t})|^2 = |s_{in}(t)|^2 + |s_{add}(t)|^2 \tag{4.3}$$

where $S_{in}(t)$ and $S_{out}(t)$ are the input and output optical signals of the add function element, and $S_{add}(t)$ is the optical sub-band/sub-wavelength signal to be added. In the sub-wavelength-level add operation, a sufficient spacing (specified in section 4.4) between the wavelengths of the two channels should be considered to avoid the optical beat interference (OBI) effect within the bandwidth of the receiver. In Eq. 4.3 it is assumed that there is no OBI effect present. In the sub-wavelength and sub-band level add operation, to achieve the contention-free add operation, $S_{add}(t)$ has to be located in a free location within the digital filtering space. This can be easily realized by selecting a free digital filter type (I and/or Q) for a given central RF frequency and/or shifting the central RF frequency of a digital filter

having a specific type in the digital domain prior to performing the E-O conversion in the corresponding TET [15].

As shown in Fig. 4.1, the ROADM operations described above are fully controlled by a ROADM-embedded DSP controller, which automatically produces a set of dynamic operating parameters through periodically communicating with the centralised SDN controller via extended OpenFlow [16, 17]. The dynamic parameter set may include digital filter characteristics employed by the targeted sub-bands/sub-wavelengths, drop RF signal characteristics when the drop operation is required, and free filters in the digital filtering space when the add operation is required. As the parameter set can be dynamically generated and finely adjusted using DSP algorithms according to the prevailing tasks, traffic status and network characteristics, the operations of the proposed ROADMs are thus flexible, scalable, adaptive and physical-layer network characteristic-transparent.

Here it is worth mentioning the following two aspects: i) for a given wavelength in a network node, the dropped signals at specific sub-wavelengths and/or sub-bands are not erased from the original input wavelength before the add operation, as shown in Fig. 4.1. As such, when the add operation is performed at the same wavelength, this may result in possible contention, whose probability is, however, very low due to the existence of a relatively large digital filtering space; ii) directionless operations can be achievable when the proposed ROADM is equipped with a typical CDC structure.

4.3 Flexible ROADMs Add/Drop Theoretical Performance

In this section, numerical simulations are performed to investigate the add and drop operation characteristics of the proposed ROADMs. Here for each sub-wavelength, use is made of Hilbert-pair-based digital filtering as described in section 3.2 to generate two spectrally-overlapped orthogonal sub-band signals capable of supporting signal encoding using different modulation formats. For simplicity but without loss of generality, OFDM modulation is considered throughout this chapter.

4.3.1 Add Operation Performance

4.3.1.1 Spectrally-overlapped Orthogonal Sub-band Level

First, numerical simulation is undertaken for the add operation at orthogonal sub-band level, as shown in Fig. 4.2. The simulation system setup is illustrated in Fig. 4.3. To generate two spectrally-overlapped orthogonal OFDM sub-bands, each electrical OFDM sub-band with 15 data-carrying subcarriers is generated using 16-QAM, a cyclic prefix of 25% is applied. The signal up-sampling factor, *M*, is fixed at 2. The digital filter tap count of 32 and the excess bandwidth factor α = 0 are also considered. Here the choice of α = 0 is to reduce the overlapping regions between the frequency responses of the same type filters (I or Q) when multiple sub-bands are employed, thus resulting in a reduced add operation penalty. The digital filter central frequencies are maintained at $f_c = f_{DAC/ADC}/4$. The DAC/ADC operates at 2GS/s with a resolution of 8-bits. The electrical OFDM signal clipping level is fixed at 14dB.

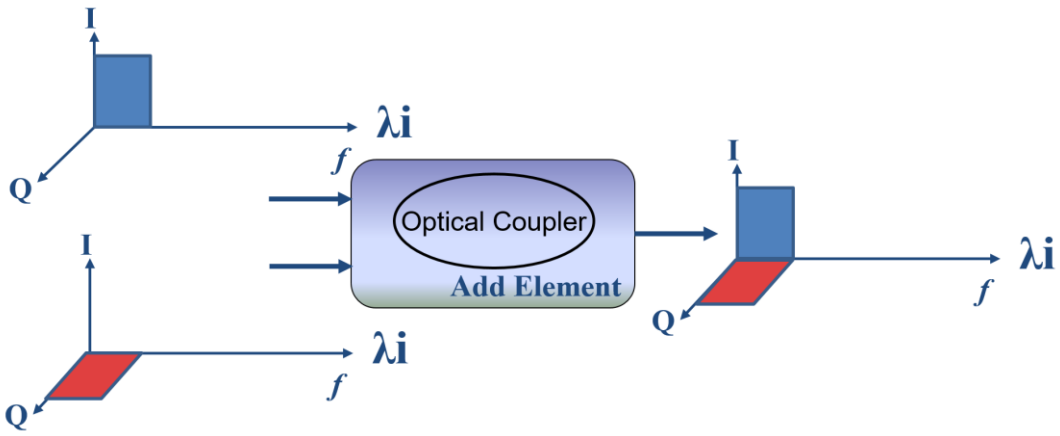

Fig. 4.2. Add operation at spectrally-overlapped orthogonal sub-band level.

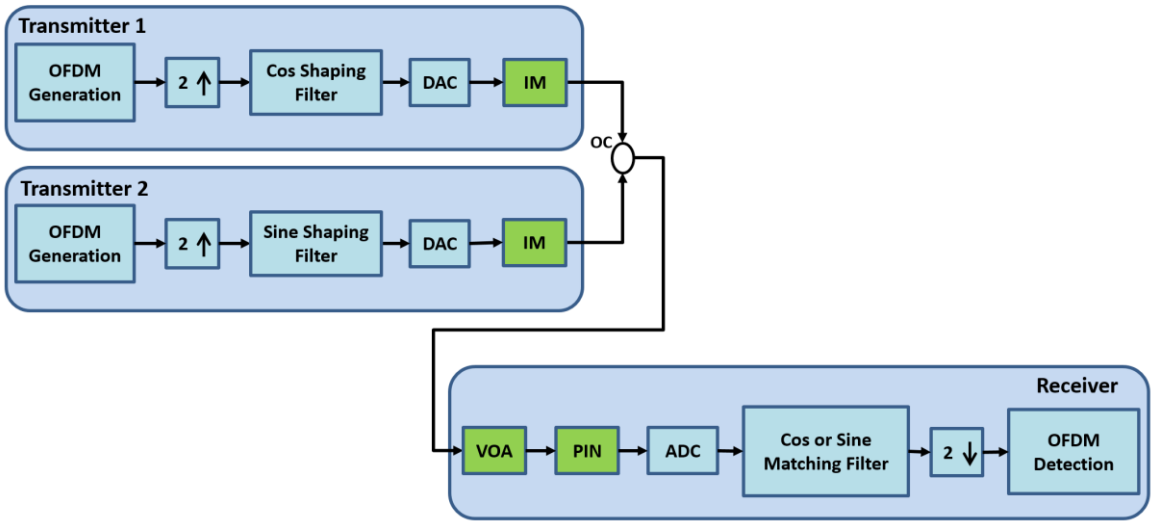

Fig. 4.3. Simulation system setup for add operation at spectrally-overlapped orthogonal sub-band level.

To highlight the impact of the add/drop operation on the signal quality, ideal intensity modulators are considered. As an example of illustrating the ROADM performance characteristics, a representative 1550nm optical carrier is used here to convey sub-wavelength/sub-band signals. The total optical launch power of each transmitter is fixed at 4 dBm. To directly detect an optical signal in a TET, a PIN is employed with a quantum efficiency of 0.8 and a power sensitivity of -19dBm.

Fig. 4.4 shows the optical spectrum of each sub-band before add operation and the combined sub-bands after the add operation. Fig. 4.5 shows the BERs curves corresponding to the cases of before and after the add operation. In Fig. 4.5, very similar BER performances for both sub-bands before and after the add operation are observed. More importantly, there is virtually no power penalty brought by the add operation, indicating that the cross-talk effect between two orthogonal sub-bands is negligible.

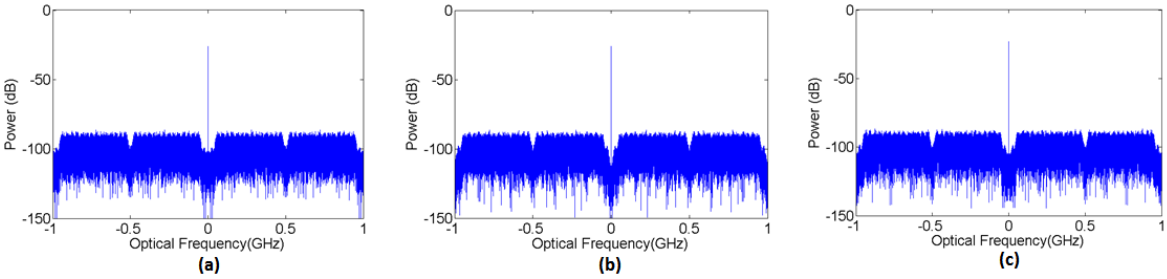

Fig. 4.4. In-phase "I" and quadrature-phase "Q" spectra of OFDM sub-bands. 0 GHz is relative to the optical carrier frequency. (a) I sub-band before add operation. (b) Q sub-band before add operation. (c) Combined two OFDM sub-bands after add operation.

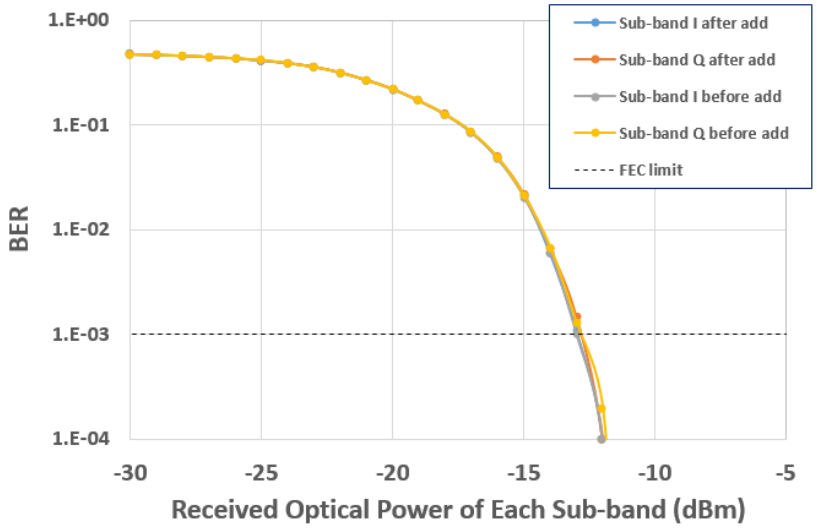

Fig. 4.5. BER versus received optical power of each orthogonal OFDM sub-band before and after performing the add operation at sub-band level.

4.3.1.2 Sub-wavelength level

To numerically investigate the add operation at the sub-wavelength level, as shown in Fig. 4.6, similar parameters are adopted to generate the electrical OFDM sub-band, only the DAC/ADC sampling speed is changed to 12GS/s. To considerably simplify numerical simulations without loss of generality, throughout the chapter, the signal up-sampling factor, M, is changed to 12, and three digital filters with central frequencies at 3.5 GHz, 4.5 GHz, 5.5 GHz are adopted. For a given optical wavelength and after intensity modulation, this results in three sub-wavelengths, each of which has two orthogonal OFDM sub-bands (I and Q). For the considered transmission system consisting of six data-conveying sub-bands and six empty sub-bands in the baseband region, according to [18] the minimum up-sampling value is 12, the selection of such an up-sampling factor not only maximizes the aggregated signal transmission capacity but also improves the spectral efficiency when the DAC/ADC sampling speeds are fixed. For such a transmission system, a further increase in up-sampling factor introduces spectral gaps between sub-wavelengths, thus lowering the maximum achievable aggregated transmission capacity, but it also reduces the channel cross-talk effect, which potentially results in a decreased add operation penalty.

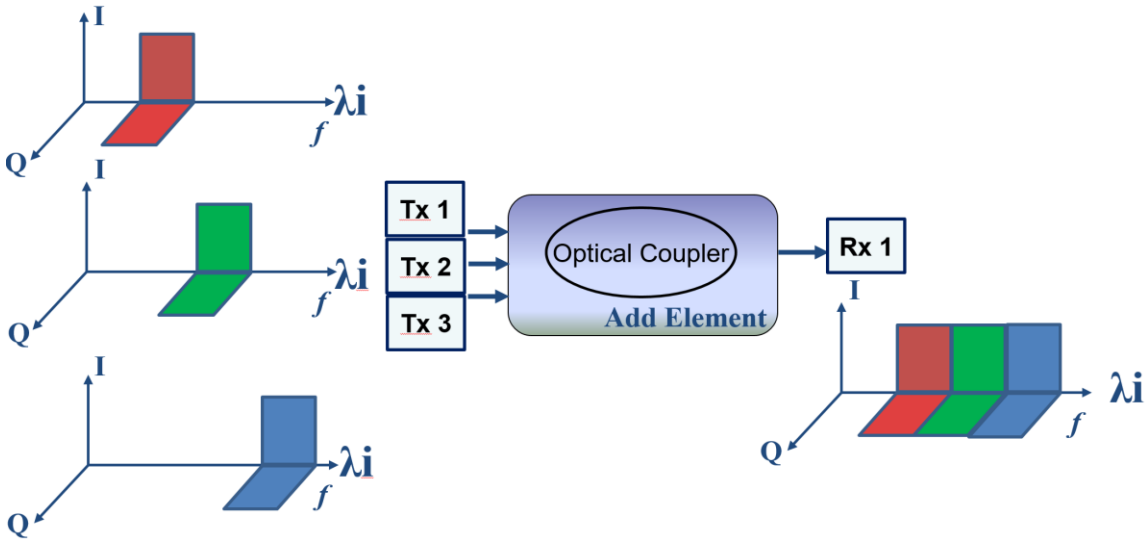

Fig. 4.6. Add operation diagram at subwavelength level The transmitters and receiver are as in 4.3.1.1.

Before performing the add operation, each individual optical carrier of the same wavelength is assumed to contain only one of the three OFDM sub-wavelength bands, and each individual sub-wavelength band is allocated at a free location of the digital filtering space assigned to the wavelength, as illustrated in Fig. 4.7 (a)-(c). Having performed the add operation, the combined signal spectra of the passively combined sub-wavelength bands are shown in Fig. 4.7 (d). After the square-law detection of the combined optical signals in a TET, making use of the DSP procedure presented in section 3.3, the bit error rate (BER) performances of these six OFDM sub-bands are calculated individually, which are plotted as a function of received sub-band optical power in Fig. 4.8. To identify the ROADM add operation impairments, for each sub-band, Fig. 4.8 shows two BER curves corresponding to the cases of before and after the add operation.

As shown in Fig. 4.8, similar to the case of add operation at the orthogonal sub-band level, here the add operation gives rise to nearly identical BER performances for all the six OFDM sub-bands before and after the add operation. This indicates that the add operation performance is independent of the sub-band's location in the digital filtering space. In addition, negligible optical power penalties are introduced as these three sub-wavelengths are located in different frequency bands therefore no additional cross-channel interference is generated.

4.3.2 Drop Operation Performance

In numerically simulating the drop operation performance of the proposed ROADM, the same system parameters and conditions are adopted as in the sub-wavelength level add operation such that an input optical signal of a representative wavelength is assumed to consist of six individual OFDM sub-bands distributed at three RF frequencies identical to those in section 4.3.1.2. To select which channel is dropped, six different drop RF signals are utilised, which have 3 different RF frequencies each with 2 different phases to determine if the I or Q signal is dropped. An optimised *k* parameter of 0.99 is employed. As already

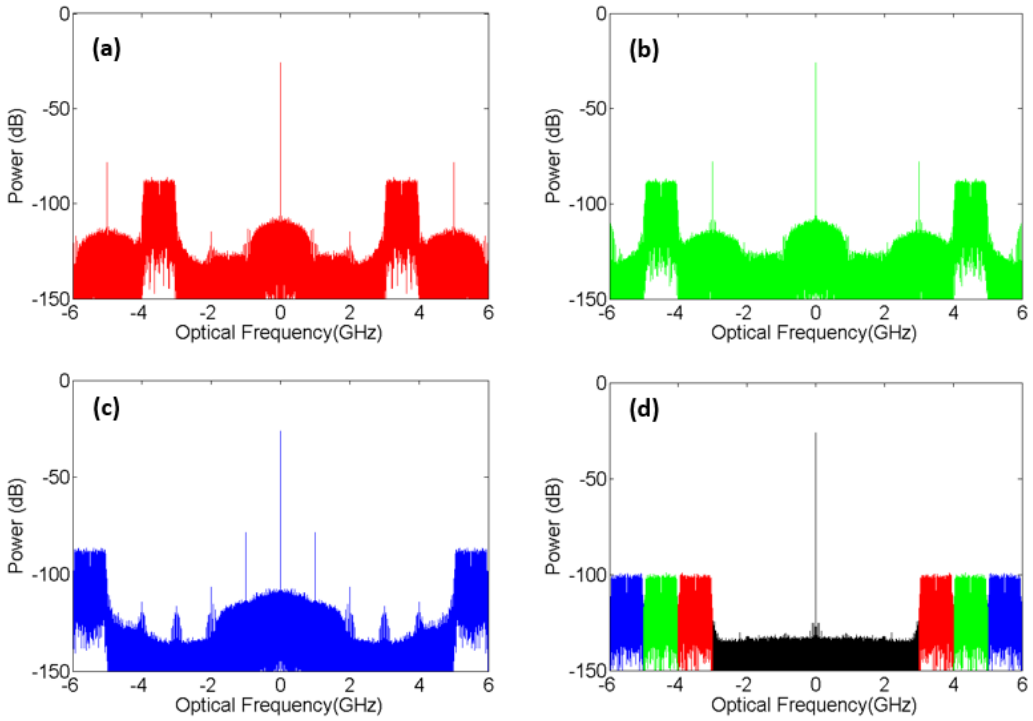

Fig. 4.7. In-phase "I" and quadrature-phase "Q" spectra of OFDM sub-bands. 0 GHz is relative to the optical carrier frequency
(a) Overlapped I and Q sub-band spectra before the add operation for sub-wavelength 1.
(b) Overlapped I and Q sub-band spectra before the add operation for sub-wavelength 2.
(c) Overlapped I and Q sub-band spectra before the add operation for sub-wavelength 3.
(d) Combined six OFDM sub-band spectra after the add operation.

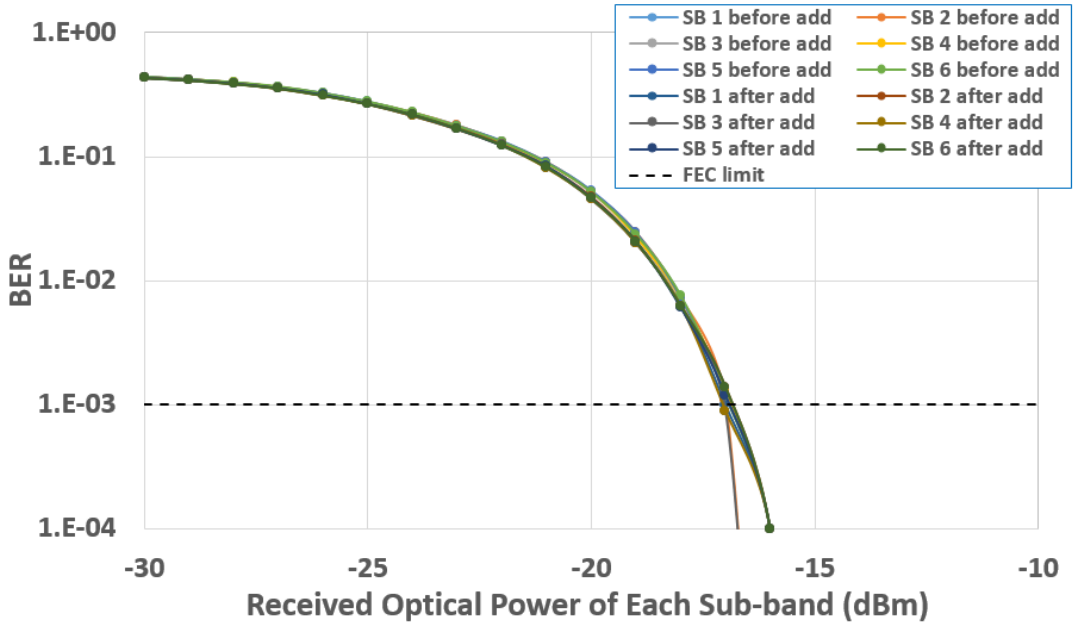

Fig. 4.8. BER versus received optical power of each OFDM sub-band before and after performing the add operation at sub-wavelength level. SB: sub-band.
SB1 (SB2)=Sub-wavelength 1 sub-band I (Q), SB3 (SB4)=Sub-wavelength 2 sub-band I (Q), SB5(SB6)=Sub-wavelength 3 sub-band I (Q)

stated in Section 4.2, the drop operations undertaken in six parallel ideal IMs produce six dropped optical signals at the same wavelengths, as shown in Fig. 4.9 (a)-(f). In performing the drop operation for each sub-band, the drop operation shifts the targeted sub-band to the baseband spectral region, and simultaneously ruins all other sub-bands contained in the same wavelength, thus making those ruined sub-bands unrecoverable.

After the direct detection of the dropped optical signal in a TET, a simple low-pass baseband digital filter having a form, $h(t) = p(t)$ due to symmetry which can be employed in the digital domain to separate the dropped signal from all the ruined and unrecoverable sub-bands. This implies that, in the TET end, a universal baseband digital filter is capable of recovering all dropped sub-bands, regardless of their locations in the digital filtering space prior to the drop operation. In addition, the feature of automatically locating the dropped sub-band at the baseband spectral region can also relax significantly the requirement on high-speed ADCs in the TET end as the bandwidth of the wanted signal is now reduced and an analogue filter can be used to remove unwanted out-of-band signals. These abovementioned two ROADM features are valuable for cost-sensitive application scenarios such as optical network units (ONUs), since these features simplify significantly the TET architecture,

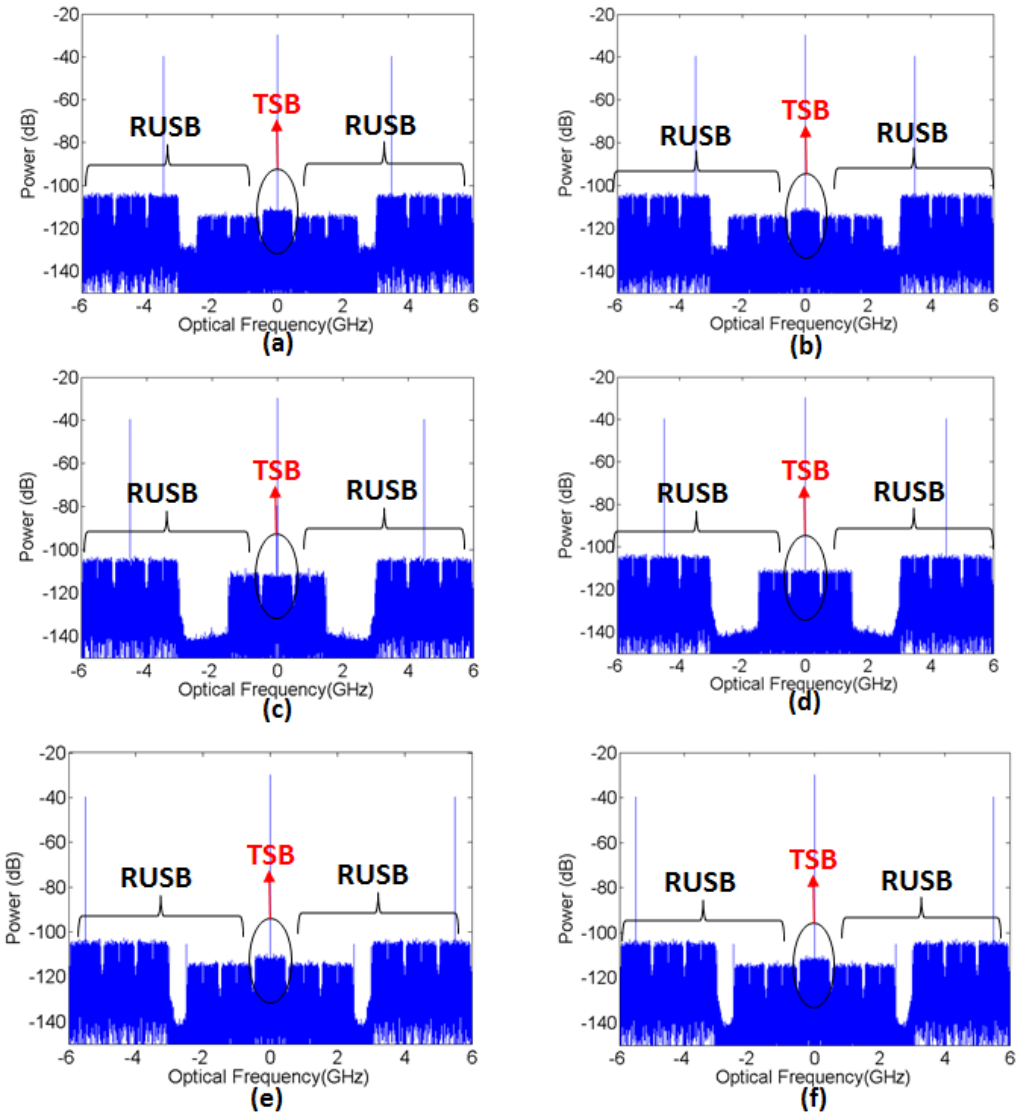

Fig. 4.9. Sub-band signal spectra after the drop operation. (a)-(f): Dropped sub-band 1,2,3,4,5,6. TSB: targeted sub-band, which is shifted to the baseband spectral region after the drop operation. RUSB: ruined and unrecovereable sub-bands of the same wavelength after the drop opeartion.

reduce the digital filter DSP complexity, and subsequently lower the TET cost and power consumption. Here it is worth mentioning that, to recover each sub-band for the before drop case, corresponding matching filters plus subsequent down-sampling, and conventional OFDM demodulation processes are applied to the received digital signal.

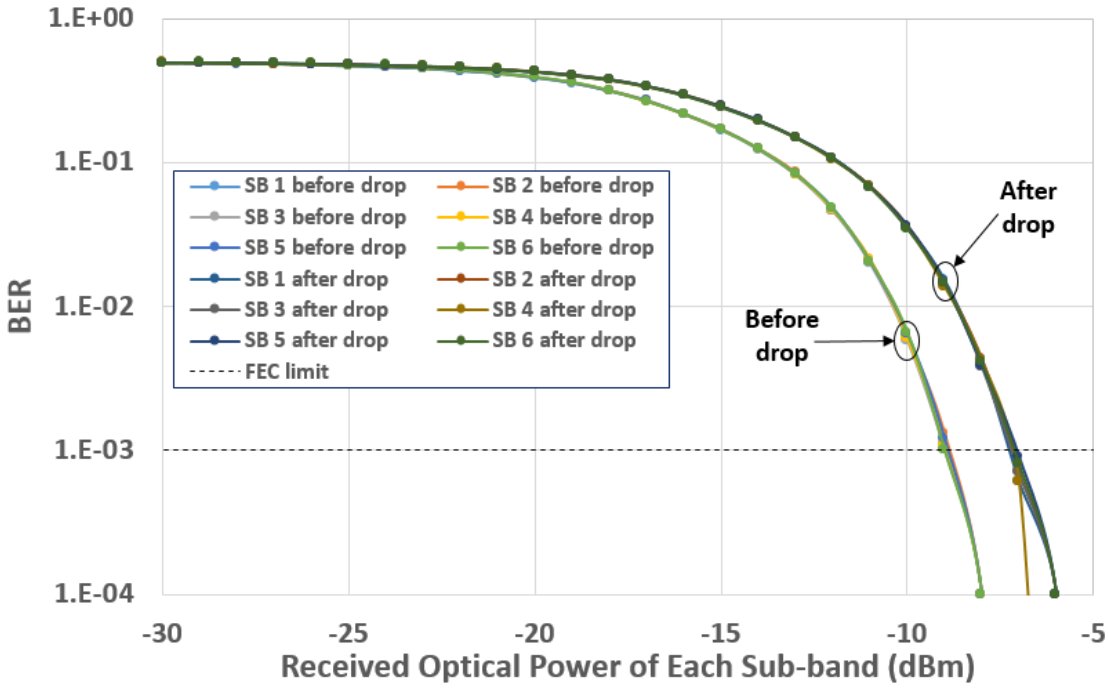

Fig. 4.10. BER versus received optical power of each OFDM sub-band before and after the drop operation. SB: sub-band.

The drop operation performance of the proposed ROADM is examined in Fig. 4.10, where the BER performances of each OFDM sub-band before and after performing the drop operation are plotted against received sub-band optical power. For the before drop case the signal is recovered using a suitable matching filter and down-sampling in the receiver. In Fig. 4.10, for the case of including or excluding the drop operation, very similar BER developing trends are observed, indicating, once again, the sub-band digital filtering space location-independent ROADM operation. It is also very interesting to note that the drop operation only gives rise to 1.6 dB power sensitivity degradations at a FEC limit of 1×10^{-3}. The aforementioned power penalty is attributed to the imperfect digital filter design associated with the finite tap count adopted in the digital filters in the transmitter.

4.4 Experimental Demonstration and Performance Evaluation of Flexible ROADMs

4.4.1 Experimental System Setup

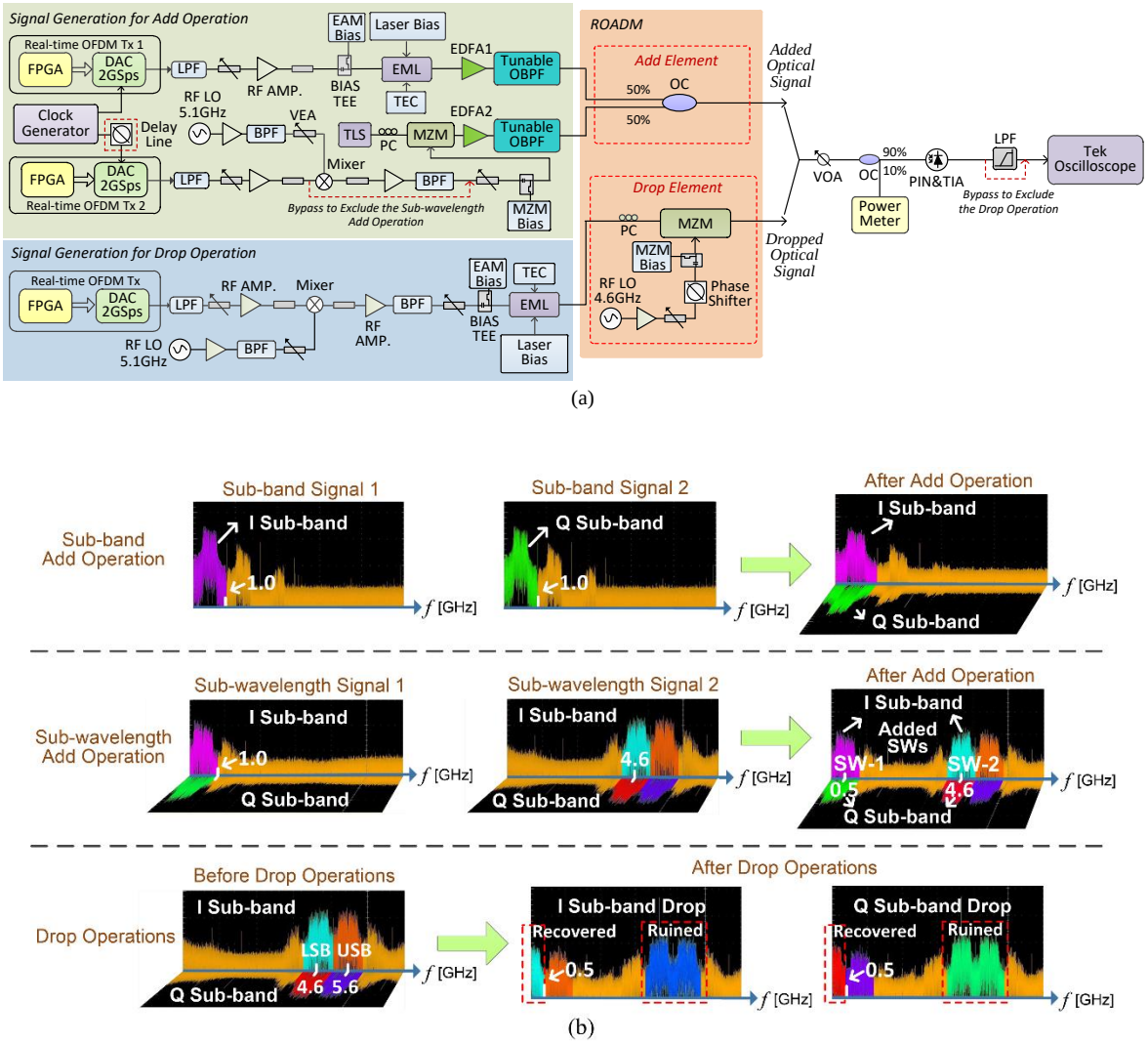

Fig. 4.11. (a) Experimental system setup for demonstrating the add and drop operations of the proposed ROADM. (b) Representative sub-band/sub-wavelength signal spectra measured before and after the ROADM operations.
LPF: low-pass filter; BPF: band-pass filter; LO: local oscillator; VEA: variable electrical attenuator; EML: electro-absorption modulated laser; EAM: Electron-absorption modulator; TEC: thermo-electric controller; MZM: Mach-Zehnder modulator; VOA: variable optical attenuator; OBPF: optical bandpass filter; TLS: tunable laser source; PC: polarization controller; OC: optical coupler; PIN+TIA: photodetector with integrated transimpedance amplifier; EDFA: erbium doped fiber amplifier; LSB: lower sideband; USB: upper sideband; SW: sub-wavelength.

The entire experimental system setup employed for demonstrating the add and drop operations of the proposed ROADM is illustrated in Fig. 4.11(a), where the core add/drop

elements are highlighted in the orange-shaded area. In Fig. 4.11(b), different representative sub-band/sub-wavelength signal spectra measured before and after the ROADM operations are inserted with their corresponding RF frequencies indicated. The adopted key device/system parameter values are listed in Table 4.1. As seen in Fig. 4.11, for both the add and drop operations, real-time software reconfigurable OOFDM transmitters are utilized to produce spectrally overlapped orthogonal sub-bands/sub-wavelengths. In the real-time OOFDM transmitter, after having digitally generated each individual OFDM signal in the FPGA, the digital signal is first up-sampled by a factor of 2 by inserting a zero-valued sample between two successive samples and then passes through a bank of 16 parallel 32-tap finite impulse response (FIR) digital shaping filters. Detailed descriptions of the real-time digital shaping filter design in the FPGA can be found in the last chapter of section 3.4, where two shaping filters (one for the I sub-band and the other for the Q sub-band) are employed. The discrete impulse responses of these two shaping filters form a Hilbert-pair, each of which possesses a square-root raised-cosine baseband pulse profile, a zero excess of bandwidth and a filter-pair central frequency of 500MHz. By setting a control parameter in the FPGA software interface, the FPGA can either generate only one digitally filtered OFDM signal (I or Q sub-band), representing an individual sub-band, or sum two digitally filtered OFDM signals (both the I and Q sub-bands), representing an individual sub-wavelength. Finally, the 2GS/s@8-bit digital-to-analogue converter (DAC) converts the generated digital sub-bands/sub-wavelengths to analogue signals with 1GHz bandwidths. It should be noted that the adopted 2×up-sampling process generates a mirrored signal spectrum, thus the bandwidths of the OFDM sub-bands/sub-wavelengths, before up-sampling, are 500MHz each.

The upper green-shaded area of Fig. 4.11 depicts the whole system setup for add operation demonstrations. For simplicity but without losing generality, here two sub-band (sub-wavelength) signals are considered for demonstrating the ROADM add operations at the sub-band (sub-wavelength) level. As shown in Fig. 4.11, at the transmitter side, independent digital and RF electronics are employed to simultaneously produce each individual sub-band/sub-wavelength signal. For sub-band add operations, the I and Q sub-band signals occupying the same spectral region (0-1GHz) are first generated by Tx 1 and Tx 2, respectively. After appropriately adjusting its power via the electrical attenuators and amplifier, the I sub-band signal is combined with an optimum DC bias voltage in a bias-T to drive a 10 GHz electro-absorption modulator (EAM) within an electro-absorption modulated

laser (EML). On the other hand, after passing through another RF gain-control stage, the Q sub-band signal is utilized to drive a 20GHz Mach-Zehnder modulator (MZM) biased at its quadrature operating point. A tunable laser source (TLS) followed by a polarization controller provides the MZM modulator with an input light source. The procedures described above lead to the generation of two optical sub-band signals. Erbium doped fiber amplifiers (EDFAs) followed by 0.8nm optical band-pass filters (OBPFs) are employed to adjust the optical power of each individual optical sub-band signal. In the add element, these two optical sub-band signals are combined using a 3-dB OC, and the combined optical signal is detected in a destination TET. Here it should be mentioned that the LPF after the PIN is bypassed for the add operation. The architecture of the experimental setup for sub-wavelength add operations is almost identical to the sub-band operations, except that the sub-wavelength signal is generated by the real-time transmitter and two sub-wavelength signals occupying different spectral regions are employed to drive the IMs. The first sub-wavelength signal is directly produced by Tx 1 and located in the baseband. Whilst the second one locating in the passband is produced by amplifying the sub-wavelength signal generated from Tx 2, up-converting with a 5.1GHz RF carrier via a double-balance mixer to generate a double-sideband (DSB) sub-wavelength signal, and then passband filtering to attenuate unwanted out-of-band spectral components.

It is also worth pointing out the following six aspects: i) to optimize the sample timing offset between the I and Q sub-band signals in sub-band add operations, an electrical RF delay line is introduced in Tx 2. However, this delay line can be omitted for the sub-wavelength add operations as the samples of the I and Q sub-bands are inherently aligned to each other when generating the digital sub-wavelength signal in FPGA; ii) the above-mentioned two optical sub-band/sub-wavelength signals are locating at different central optical wavelengths with a spacing of 0.3nm. Such a wavelength spacing is sufficiently large to completely eliminate the OBI effect associated with direct detection of the added optical channels in the destination TET [19]. It should be noted that the wavelength spacing is unnecessary when coherent detection is employed in the destination TET [19]; iii) the employment of the different intensity modulators in Fig. 4.11, i.e., the EML for the first optical sub-band/sub-wavelength signal and the MZM for the second one, provides an opportunity to rigorously evaluate the ROADM performance robustness to different IM types; iv) shifting the second sub-wavelength signal to a RF carrier frequency of 5.1GHz enables the investigations of the performance of ROADM

Table 4.1 Device and System Parameters

Parameter	Value	Unit
IFFT/FFT points per sub-band	32	
Data-carrying subcarriers per sub-band for sub-band add	6 high frequency	subcarriers
Data-carrying subcarriers per sub-band for sub-wavelength add	10 high frequency	subcarriers
Data-carrying subcarriers per sub-band for drop	10 high frequency	subcarriers
Subcarrier modulation format	16-QAM	
DAC sample rate	2	GS/s
DAC resolution	8	bit
DSO sample rate	25	GS/s
OFDM symbol rate	25	MHz
Samples per OFDM symbol[a]	32 (16ns)	samples
Cyclic prefix[a]	8 (4ns)	samples
Total samples per OFDM symbol[a]	40 (20ns)	samples
Raw signal rate per sub-band	0.75/1.25	Gb/s
Raw signal rate per sub-wavelength	1.5/2.5	Gb/s
Typical RF amplifier noise figure	5-6	dB
EDFA noise figure	5	dB
EML laser operating wavelength	~1550	nm
3dB EML modulation bandwidth	10	GHz
MZM Vπ@DC(20GHz)	1.5(3.5)	V
MZM modulation bandwidth	20	GHz
MZM insertion loss	4.5	dB
PIN detector bandwidth	10	GHz
PIN detector sensitivity[b]	-19	dBm
PIN noise	2.8	mV_{rms}

[a]Before up-sampling and after down-sampling.
[b]Corresponding to 10 Gb/s non-return-to-zero data (PRBS 2^{31}-1) at a BER of 1.0×10^{-9}.

operations for multiple sub-wavelength cases. As theoretically predicted in [14] and experimentally demonstrated in Section 4.4.2, the ROADM operation performance is independent of sub-band/sub-wavelength spectral location, as a direct result, different RF carrier frequencies can also be employed without considerably affecting the ROADM operation performance; v) in the experiment a RF mixer is used due to the unavailability of a high bandwidth DAC. When the digital-domain Hilbert-pair filter construction approach and high bandwidth DAC are employed to generate different sub-wavelength signals the RF mixer can be removed. This can reduce the spectral guard band between two adjacent sub-wavelength signals for practical applications [14]; vi) the noise in the experimental system in Fig. 4.11 is mostly generated by the EDFAs and RF amplifiers.

The experimental system setup for demonstrating the ROADM drop operations is illustrated in the lower blue-shaded area of Fig. 4.11, where a single optical passband DSB sub-wavelength signal is produced following procedures similar to those described above for generating the second optical sub-wavelength signal, except that an EML is utilized to perform the E-O conversion in the corresponding transmitter. For the optical passband DSB sub-wavelength signal, both the upper sideband and the lower sideband each consists of two

spectrally overlapped orthogonal sub-bands, thus either can be used to perform the drop operation in the IM-based drop element. Here a drop RF signal with a sinusoidal waveform at a frequency of 4.6GHz (= 5.1GHz-0.5GHz) is chosen to drop the lower sideband by driving a 20GHz MZM-based IM biased at its quadrature operating point. By carefully adjusting the phase of the drop RF signal with an RF delay line, the I sub-band can be dropped, a subsequent $\pi/2$ phase shift of the drop RF signal results in the dropping of the Q sub-band.

At the destination TET side, the output optical signal from the ROADM first passes through a variable optical attenuator (VOA) to control the received optical power level. Following a 90/10 OC to allow optical power measurement, the ROADM output optical signal is converted to the electrical domain by a 12GHz PIN with integrated transimpedance amplifier (TIA) via direct detection. As illustrated in Fig. 4.11, an analogue low-pass filter is omitted (included) before the capture of the added (dropped) signal using a real-time digital sampling oscilloscope (DSO), the DSO-captured signal is then digitally processed offline using MATLAB. In the TET DSP procedure, for the added signals occupying the baseband spectral regions (including both the added sub-band signal and the baseband sub-wavelength signal), corresponding digital matching filters are used to separate the two spectrally overlapped sub-bands in the baseband. Whilst for the added signal occupying the passband spectral region (the passband sub-wavelength signal only), the I and Q sub-bands in the lower sideband of the passband DSB sub-wavelength signal are shifted to the baseband separately using digital down-conversion with RF carriers at 4.6GHz with a phase difference of $\pi/2$. Finally, the spectrally separated sub-bands of the added and dropped signals are processed using conventional OFDM receiver DSP functions, which include automatic symbol synchronization, pilot-subcarrier detection, channel estimation/equalization, as well as all other DSP functions inverse to their transmitter counterparts as detailed in the last chapter of section 3.4. .

Due to the low tap count-induced enhancement of digital filter frequency response ripples experienced by the low frequency subcarriers, as seen in the last chapter, and strong unwanted intermixing frequency products generated upon square-law photon detection, within each sub-band, only 6 (10) out of possible 15 subcarriers located at the higher frequencies are activated to carry user information in each individual sub-band (sub-wavelength) signal, and 16-quaternatry amplitude modulation (QAM) is taken on all these

active subcarriers. As such, considering the system parameters presented in Table 4.1, the aggregated raw bit rates are 1.5Gb/s and 5Gb/s for the added sub-band signal and the added sub-wavelength signal, respectively.

4.4.2 Experimental Results

Having described the operating principles of the proposed ROADM in section 4.2 and the corresponding add/drop experimental system setup in section 4.4.1, extensive experimental measurements are first undertaken of bit error rate (BER) performance of the add and drop operations in section 4.4.2.1. In addition, detailed ROADM performance robustness is also experimentally explored against both differential optical power dynamic ranges and drop RF signal power variations in section 4.4.2.2 and section 4.4.2.3, respectively.

4.4.2.1 Performance of Add and Drop Operations

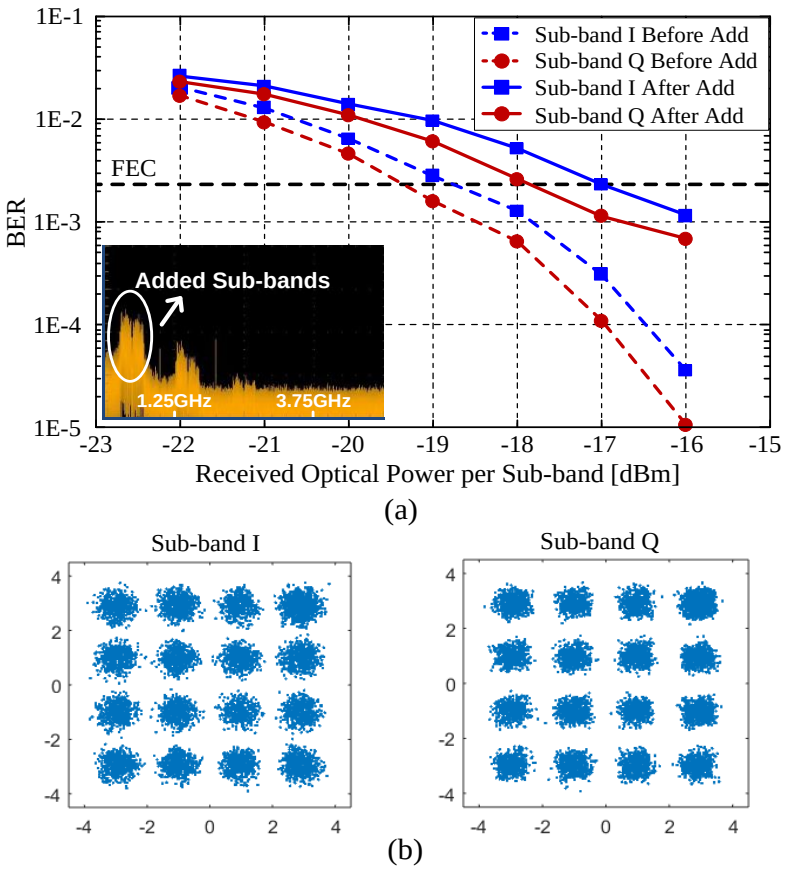

Fig. 4.12. (a) Measured BER performances of each individual OFDM sub-band before and after the sub-band add operation. The inset is the electrical spectrum after the sub-band add operation. (b) Equalized subcarrier constellations of two sub-bands after the sub-band add operation at a -16dBm ROP per sub-band.

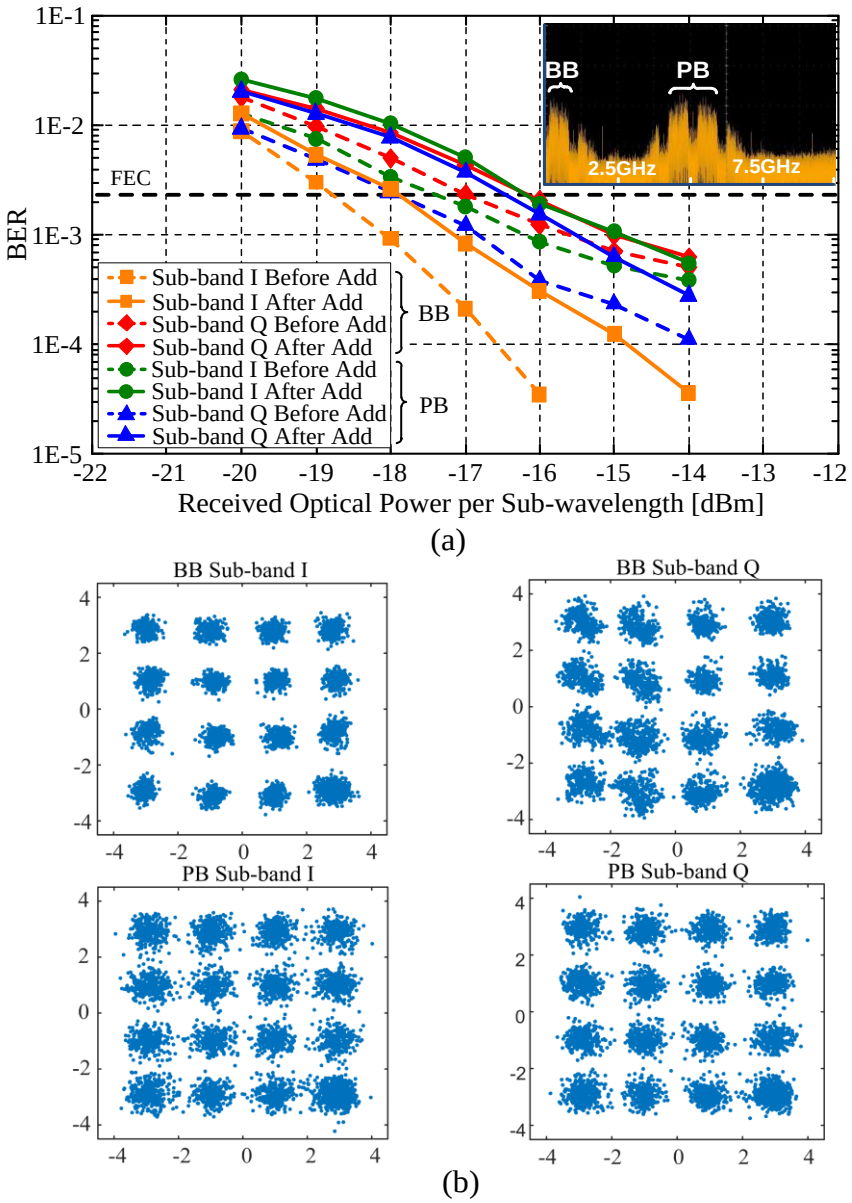

Fig. 4.13. (a) Measured BER performances of each individual OFDM sub-band before and after the sub-wavelength add operation. The inset is the electrical spectrum after the sub-wavelength add operation. (b) Equalized subcarrier constellations of all the sub-bands after the sub-wavelength add operation at a -14dBm ROP per sub-wavelength. BB: baseband; PB: passband.

The measured ROADM add operation BER performances are shown in Fig. 4.12 and Fig. 4.13, where the BER performances of each individual OFDM sub-band before and after the add operation are plotted as a function of received optical power (ROP) per sub-band/sub-wavelength. The insets illustrate the electrical spectrum of the added optical signals measured after the PIN+TIA. In obtaining both Fig. 4.12 and Fig. 4.13, the power of each optical sub-band/sub-wavelength signal input to the add element is fixed at 4dBm. In measuring the sub-band BER performances before the add operation, each individual optical

sub-band/sub-wavelength signal emerging from the OBPF is directly injected into the VOA without passing through the add element. Furthermore, for fair performance comparisons of BER versus ROP per sub-band/sub-wavelength between "before the add operation" and "after the add operation", in plotting Fig. 4.12(a) and Fig. 4.13(a), the BER curves measured after the add operation are left-shifted by 3dB, as the added optical signals contain two optical sub-band/sub-wavelength signals with equal optical powers, of which only one sub-band/sub-wavelength signal is recovered at a time.

As expected from the theoretical predictions in section 4.3, it is shown in Fig. 4.12(a) and Fig. 4.13(a) that the add operation gives rise to very similar BER developing trends for all these added sub-bands with different digital filter types and central RF frequencies. This indicates that the add operation performance is independent of not only the digital filter type but also sub-band/sub-wavelength spectral location. As also seen in Fig. 4.12(a), for the I (Q) sub-band, the sub-band add operation introduces approximately 1.8dB (1.5dB) power penalty at a forward error correction (FEC) limit of 2.3×10^{-3} (this FEC limit is used in this chapter to maintain good differential optical power dynamic range in section 4.4.2.2 however this results in an increased FEC overhead). Whilst a 0.9dB (1.4dB) power penalty caused by the sub-wavelength add operation is observed for the baseband (passband) sub-wavelength in Fig. 4.13(a). The power penalty for sub-band add operation occurs mainly due to 1) the signal leakages between two orthogonal sub-bands occupying the same spectral region and 2) the noise and distortions associated with electrical and optical components in the experiment. The signal leakage is mainly due to the DAC/ADC-induced channel frequency response roll-off. This roll-off was not present in the numerical simulation in section 4.3.1. In addition there is virtually no noise in the simulation, which can explain why no power penalty was observed. The signal leakage can be significantly diminished when use is made of a DSP-based cross-channel interference cancellation (CCIC) technique presented in [20]. The power leakage for the sub-wavelength add operation is mainly caused by cross-talk from out-of-band noise associated with a sub-wavelength at a different centre frequency due to the device-induced noise and distortions mentioned above in sub-band add operation. Again this explains the negligible power penalty for sub-wavelength add operation seen in the simulation. After performing channel equalization in the destination TET, the combined received constellations of all active subcarriers after the add operation are exemplified in Fig. 4.12(b) and Fig. 4.13(b) for each individual sub-band at a -16dBm (-14dBm) ROP per sub-band (sub-wavelength).

It should also be noted in Fig. 4.12(a) that, a ROP difference of 0.7dB (0.9dB) between the I sub-band and Q sub-band occurs before (after) the sub-band add operation. The observed ROP differences are because the high modulation extinction ratio associated with the MZM considerably increases the BER performances for the Q sub-band. Thus, this ROP difference can considerably decrease if two IMs with the similar modulation performances are utilized for the E/O conversions. Moreover, before and after the add operations, there exists ROP differences of approximately 2dB between the I sub-bands and the Q sub-bands for the baseband sub-wavelength in Fig. 4.13(a). Whilst for the passband wavelength, the corresponding ROP differences are reduced to <0.5dB. Such ROP differences between these two sub-wavelengths are also attributed to the different IMs adopted in the experiments. In comparison with the MZM-based passband sub-wavelength, the nonlinearity of the EML used in the baseband sub-wavelength considerably enhances the unwanted frequency response ripples for the Q sub-bands, thus giving rise to reduced BER performances for the Q sub-bands. Similar phenomena have also been experimentally observed in section 3.4.

For the cases of before and after the drop operation, Fig. 4.14(a) shows the measured BER performances of the two involved sub-bands. The insets illustrate the corresponding electrical spectra measured after the PIN+TIA. In measuring the sub-band BER performances before the drop operation, the optical signal emerging from the EML by-passes the following drop element, and is directly injected into the VOA. In addition, the electrical low-pass filter after the PIN is also omitted. As such, a single DSB passband signal spectrum occurs, as shown in the left inset of Fig. 4.14(a). Whilst in measuring the sub-band BER performances after the drop operations, the MZM in the drop element is biased at its quadrature operating point, and the corresponding drop RF signal power is set at 15.3dBm. The DC and AC components of the RF drop signal are finely adjusted for minimum BER. As illustrated in the right inset of Fig. 4.14(a), after the drop operation, the targeted sub-band is shifted to the baseband spectral region, and the signal occupying the passband spectral region still remains, which is, however, ruined and unrecoverable and will also be removed by the LPF.

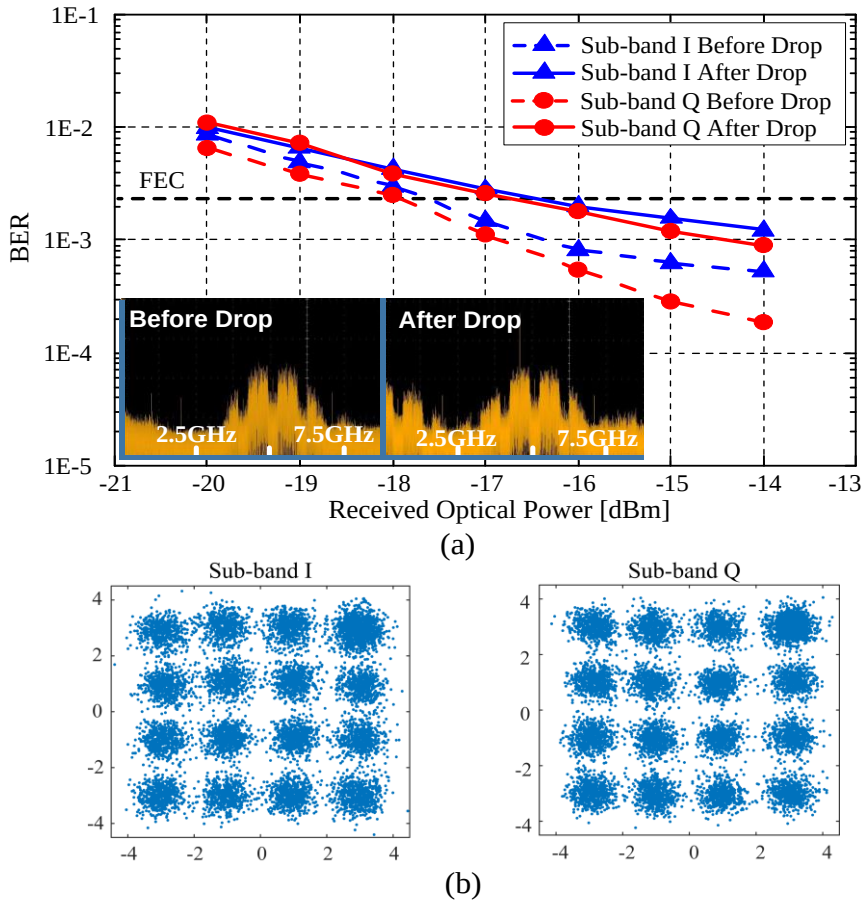

Fig. 4.14. (a) Measured BER performances of each individual OFDM sub-band before and after the drop operation. The insets are the electrical spectra before and after the drop operation. (b) Equalized subcarrier constellations of all the subcarriers for both sub-bands after the drop operation at a -14dBm ROP.

It can be seen in Fig. 4.14(a) that, before and after the drop operations, similar BER developing trends occur for both sub-bands. This agrees very well with numerically simulated results in section 4.3.2. The observed similarity in BER developing trends indicates the digital filter type-independent ROADM drop operation performance. It is also very interesting to note in Fig. 4.14(a) that the drop operation causes only 1.1dB and 1.2dB (2.5dB and 2.8dB) power penalties at a FEC limit of 2.3×10^{-3} (1×10^{-3}) for the I sub-band and Q sub-band, respectively. There are three physical mechanisms underpinning the drop operation-induced power penalty: a) the dropped sub-band spectral distortions induced by the imperfect MZM-IM transfer function, b) imperfect digital filtering associated with the limited filter tap count adopted in the transmitters detailed in section 3.4 and c) an imperfect RF drop signal. Compared to the experiment, the corresponding simulation in section 4.3.2 shows less power penalty even with more subcarriers enabled, this is because only the imperfect digital filtering effect is present in the simulation. For both simulation and

experiment, a considerable reduction in drop operation-induced power penalty is expected when the employed digital filters are further optimized. Finally, for both of the dropped sub-bands measured at a ROP of -14dBm, the equalized subcarrier constellations including all employed subcarriers are given in Fig. 4.14(b).

4.4.2.2 Add Operation Performance Robustness to Differential Optical Power Dynamic Ranges

From the practical application point of view, to improve not only the ROADM performance robustness but also component/system/network flexibility, it is greatly advantageous if the ROADM add operation can tolerate a large differential optical power dynamic range. Here the differential optical power dynamic range is defined as, for a fixed optical power received in a destination TET, the maximum allowable variation range of the optical power of a variable-power input optical sub-band/sub-wavelength signal, over which the BERs of all involved sub-bands are still less than the FEC limit after the add operation.

To explore the differential optical power dynamic range for the add operation, Fig. 4.15 and Fig. 4.16 are presented, where the BER performances of all involved sub-bands against the input optical power of an individual optical sub-band/sub-wavelength signal are plotted for a fixed total ROP of -12dBm after the add operations. In measuring both Fig. 4.15 and Fig. 4.16, the output power of the EDFA is adjusted to provide various required input powers of the variable-power optical sub-band/sub-wavelength signal, whilst the input power of the fixed-power optical sub-band/sub-wavelength signal is kept at a constant value. Here two cases are considered: Case 1- the input optical power of the I sub-band (baseband sub-wavelength) varies and the input optical power of the Q sub-band (passband sub-wavelength) is fixed at 4dBm; Case 2- the input optical power of the I sub-band(baseband sub-wavelength) is fixed at 4dBm and the input optical power of the Q sub-band(passband sub-wavelength) varies.

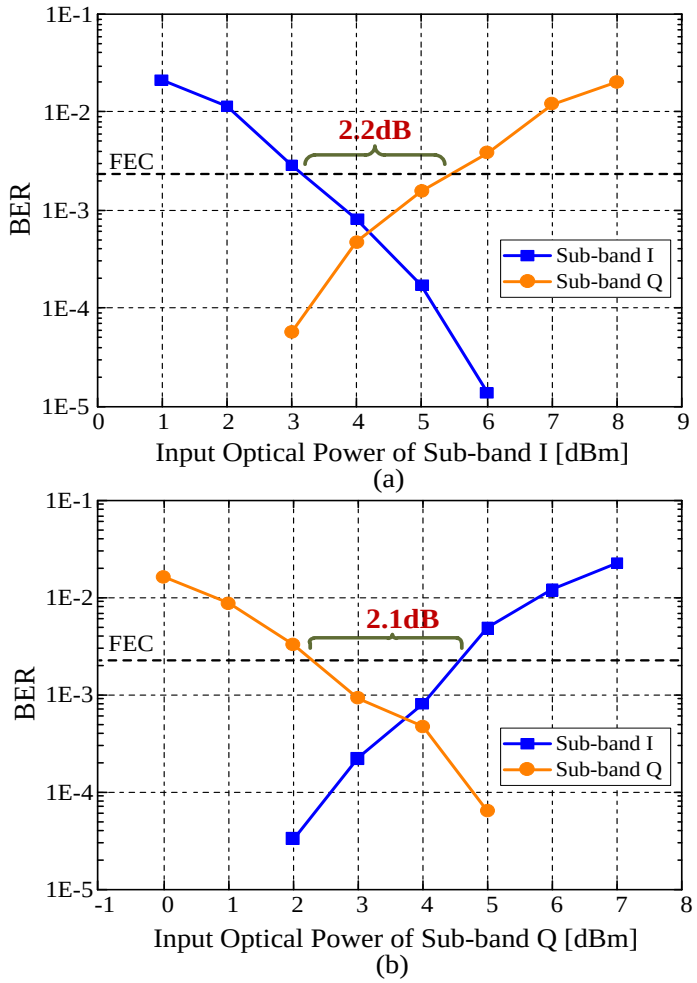

Fig. 4.15. Differential optical power dynamic ranges for the sub-band add operation at a ROP of -12dBm. (a) Case 1; (b) Case 2.

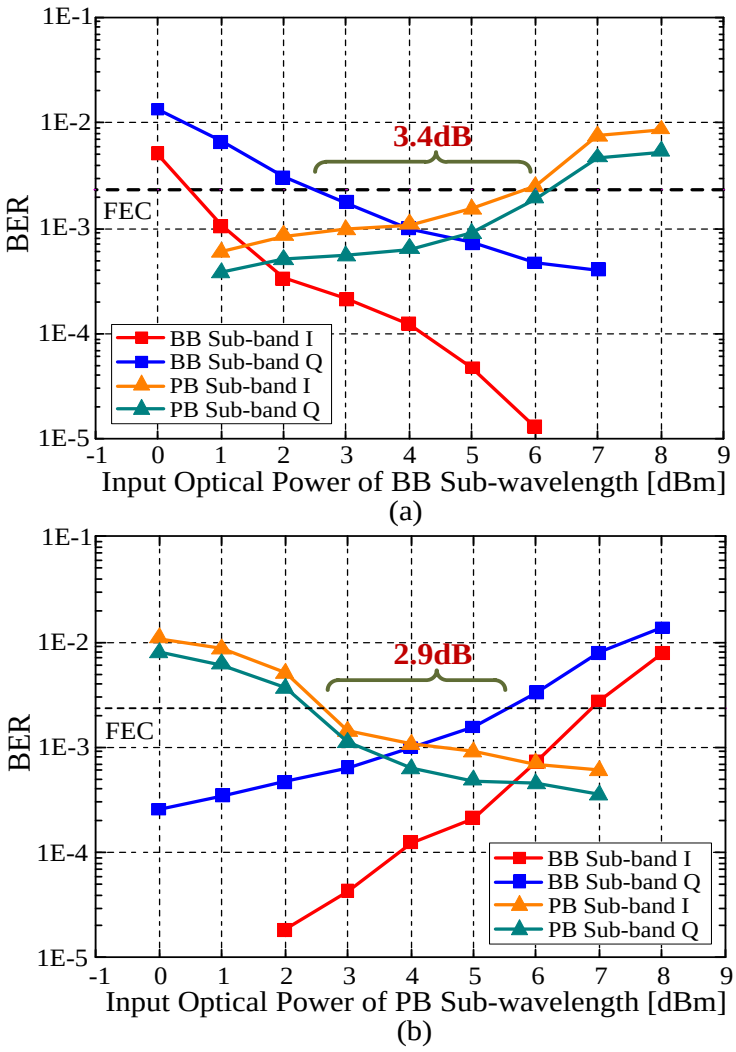

Fig. 4.16. Differential optical power dynamic ranges for the sub-wavelength add operation at a ROP of -12dBm. (a) Case 1; (b) Case 2. BB: baseband; PB: passband.

It can be seen in both Fig. 4.15 and Fig. 4.16 that, for a fixed -12dBm ROP in the destination TET, an increase in the input optical power of the variable-power optical sub-band/sub-wavelength signal improves the BER performances of the sub-bands conveyed by itself, and simultaneously degrades the sub-band BER performances of the fixed-power optical sub-band/sub-wavelength signal. This mainly results from the changes in effective optical signal to noise ratio (OSNRs) of the involved sub-bands. It can be seen in Fig. 4.15 (Fig. 4.16) that, for the sub-band (sub-wavelength) add operation, the proposed ROADM can tolerate a differential optical power dynamic range of ≥2.1dB (≥2.9dB) at a total ROP as low as -12 dBm. The upper limit of the variable input optical power is determined by the minimum sub-band OSNR allowed by the fixed-power optical sub-band/sub-wavelength signal, whilst the lower limit of the variable-power input optical power is determined by the minimum sub-

band OSNR allowed by the variable-power optical sub-band/sub-wavelength signal. This implies that the ROP at the destination TET has an important influence on the differential optical power dynamic ranges of the add operations.

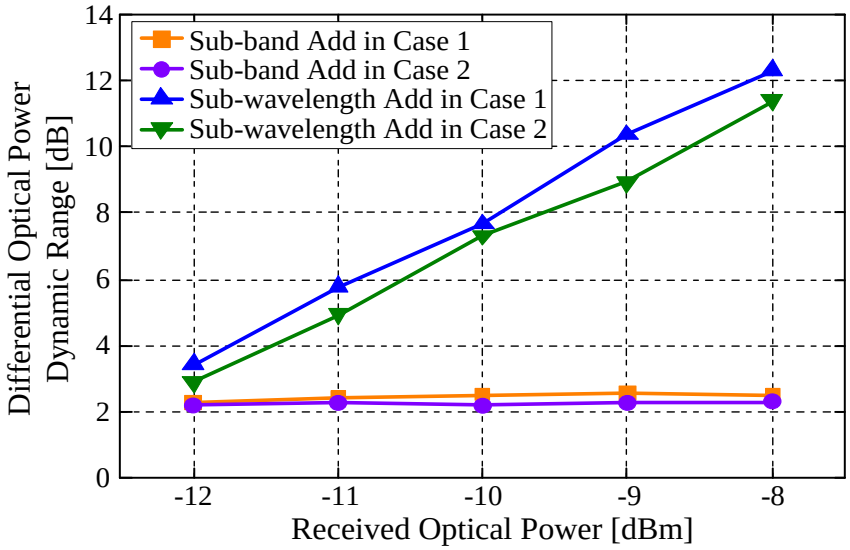

Fig. 4.17. ROP-dependent differential optical power dynamic ranges for the add operation for two different cases.

To confirm the aforementioned statement, Fig. 4.17 illustrates the measured ROP dependent-differential optical power dynamic ranges for Case 1 and Case 2. It can be observed in Fig. 4.17 that for both considered cases, the differential optical power dynamic range in dB is almost proportional to total ROP in dBm for the sub-wavelength add operation. When the total ROP is fixed at -8dBm, the achievable differential optical power dynamic ranges are as high as 12.3dB and 11.4dB for Case1 and Case 2, respectively. This indicates that excellent robustness of the add operation performance exists against optical power variations of the involved sub-wavelength signals. On the other hand, the differential optical power dynamic range is independent of the ROP for the sub-band operation. This is because the channel frequency response roll-off-induced crosstalk effect between two spectrally overlapped sub-bands is another major physical mechanism underpinning the minimum attainable sub-band BERs. Therefore, it is easily envisaged that the differential optical power dynamic ranges for the sub-band add operation can also considerably increase with the increasing ROP when the CCIC technique is used at the destination TET [20].

4.4.2.3 Drop Operation Performance Robustness to Drop RF Signal Power Variations

As the drop RF signal power plays a significant role in determining the ROADM drop operation performance [14], the main objective of this subsection is to experimentally investigate the impact of drop RF signal power on the drop operation BER performance, based on which an optimum drop RF signal power variation range can be identified.

The measured drop operation-induced power penalties at the FEC limit of 2.3×10^{-3} are shown in Fig. 4.18 as a function of drop RF signal power for both the I and Q sub-bands. The adopted experimental conditions are identical to those used in Fig. 4.14, except that the drop RF signal power varies from 8dBm to 18dBm in Fig. 4.18.

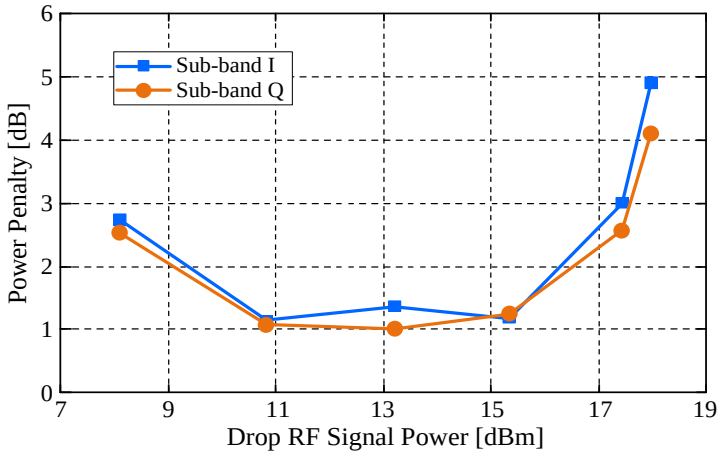

Fig. 4.18. Measured drop operation power penalty as a function of drop RF signal power for the ROADM drop operation.

It is shown in Fig. 4.18 that, when the MZM-based drop element is driven by a drop RF signal with a relatively small power of <10.8dBm, the drop operation-induced power penalty decreases with increasing drop RF signal power. This agrees very well with the theoretical simulations in section 4.3. Such power penalty reduction is because a large drop RF signal power increases the optical power of the dropped sub-band that is shifted to the baseband spectral region. Whilst when the drop RF signal power is higher than 15.3dBm, the power penalty sharply increases with increasing drop RF signal power, mainly resulting from the nonlinear intensity modulation effect. The co-existence of the abovementioned mechanisms causes the occurrence of a 7.1dB optimum drop RF signal power variation range, corresponding to which a minimum power penalty of approximately <2dB is observed. Such

a large optimum drop RF signal power variation range is useful for not only improving the robustness of the drop operation performance, but also considerably relaxing the stringent requirements on drop RF signal powers within acceptable power penalties.

4.5 Conclusion

Making use of Hilbert-pair-based digital filtering, intensity modulation and passive optical coupling, simple and flexible ROADMs free from both optical filters and O-E-O conversions have been numerically simulated and experimentally demonstrated, for the first time, to perform DSP-enabled dynamic add and drop operations at wavelength, sub-wavelength and spectrally overlapped sub-band levels. Technical feasibility of the proposed ROADMs has been confirmed in numerical simulations in terms of add and drop operation performance characteristics. Furthermore, extensive experimental investigations of physical-layer add and drop operation performances and their robustness to variations in both differential optical power dynamic range and drop RF signal power have also been conducted in IMDD-based optical network nodes. It has been shown that the ROADM performance is independent of the sub-band spectral location, and that the ROADM introduces optical power penalties of only 1.8dB for the add operation and 1.2dB for the drop operation. In addition, for a fixed total optical power as low as -12dBm after the add operation, the add operation still tolerates a differential optical power dynamic range of >2dB. Whilst for the drop operation, an optical power penalty of <2dB is observed over an optimum drop RF signal power variation range of 7.1dB. Experimental results indicate that the demonstrated ROADMs have not only excellent performance robustness but also great potential to considerably relax stringent requirements on network components.

References

[1] B. Schrenk, F. Laudenbach, R. Lieger, T. Lorünser, P. Bakopoulos, A. Poppe, M. Stierle, H. Avramopoulos, and H. Leopold, "Passive ROADM flexibility in optical access with spectral and spatial reconfigurability," *IEEE J. Sel. Areas Commun.*, vol. 33, no. 12, pp. 2837-2846, Dec. 2015.

[2] S. Gringeri, B. Basch, V. Shukla, R. Egorov, and T. J. Xia, "Flexible architectures for optical transport nodes and networks," *IEEE Commun. Mag.*, vol. 48, no. 7, pp. 40-50, Jul. 2010

[3] J. M. Simmons and A. M. Saleh, "Wavelength-selective CDC ROADM designs using reduced-sized optical cross-connects," *IEEE Photon. Technol. Lett.*, vol. 27, no. 20, pp. 2174-2177, Oct. 2015.

[4] S. Takashina, Y. Mori, H. Hasegawa, K. Sato, T. Watanabe, "Wavelength-tunable filters utilizing arrayed waveguide gratings for colorless/directionless/contentionless optical signal drop in ROADMs," *IEEE Photon. Journal.*, vol. 7, no. 1, pp. 7100511, Feb. 2015.

[5] W. I. Way, P. N. Ji, and A. N. Patel, "Wavelength contention-free via optical bypass within a colorless and directionless ROADM," *J. Opt. Commun. Netw.*, vol. 5, no. 10, pp. A220-A229, Oct. 2013.

[6] Z. Shen, H. Hasegawa, K. Sato, T. Tanaka, and A. Hirano, "A novel semi-flexible grid optical path network that utilizes aligned frequency slot arrangement," in *European Conference and Exhibition on Optical Communication (ECOC)*, London, 2013, Paper We.2.E.2.

[7] Y. Sakamaki, T. Kawai, M. Fukutoku, T. Kataoka, and K. Suzuki, "Experimental demonstration of arrayed optical amplifiers with a shared pump laser for realizing colorless, directionless, contentionless ROADM," *Opt. Express*, vol. 20, no. 26, pp. B131-B140, Dec. 2012.

[8] K. Suzuki, K. Seno. Y. Ikuma, "Application of Waveguide/free-space optics hybrid to ROADM Device," *J. Lightw. Technol.*, vol. 35, no. 4, pp. 596-606, Feb. 2017

[9] A. Muhammad, G. Zervas, G. Saridis, E. H. Salas, D. Simeonidou, and R. Forchheimer, "Flexible and synthetic SDM networks with multi-core-fibers implemented by programmable ROADMs," in *European Conference and Exhibition on Optical Communication (ECOC)*, Cannes, 2014, Paper P.6.6.

[10] M. Nooruzzaman and E. Halima, "Low-cost hybrid ROADM architectures for scalable C/DWDM metro networks," *IEEE Communication Magazine*, vol. 54, no. 8, pp. 153-161, Aug. 2016.

[11] W. Jin, X. Duan, M. Bolea, R. P. Giddings, N. Jing, C. F. Zhang, K. Qiu, and J. M. Tang, "New ROADMs with DSP-enabled dynamic and flexible operations for elastic optical networks," in *Optical Fiber Communication Conference (OFC)*, Los Angeles, 2015, Paper Th2A.50.

[12] J. D. Allen and P. Kubat, "Reliable video broadcasts via protected steiner trees," *IEEE Communication Magazine*, vol. 48, no. 2, pp. 70-76, Feb. 2010.

[13] M. Furdek, A. Muhammad, G. Zervas, N. Alloune, C. Tremblay, and L. Wosinska, "Programmable filterless network architecture based on optical white boxes," in *International Conference on Optical Network Design and Modeling (ONDM)*, Cartagena, Spain, 2016, Pages 1-6.

[14] W. Jin, X. Duan, Y. Dong, B. Cao, R. P. Giddings, C. F. Zhang, K. Qiu, and J. M. Tang, "DSP-enabled flexible ROADMs without optical filters and O-E-O conversions," *J. Lightw. Technol*., vol. 33, no. 19, pp. 4124-4131, Oct. 2015.

[15] M. Bolea, R. P. Giddings, M. Bouich, C. Aupetit-Berthelemot, and J. M. Tang, "Digital filter multiple access PONs with DSP-enabled software reconfigurability," *J. Opt. Commun. Netw*., vol. 7, no. 4, pp. 215-222, Apr. 2015.

[16] N. Cvijetic, "Software-defined optical access networks for multiple broadband access solutions," in *Opto-Electronics and Communications Conference (OECC)*, 2013, paper TuP2-1.

[17] N. Cvijetic, A. Tanaka, P. N. Ji, S. Murakami, K. Sethuraman, and T. Wang, "First OpenFlow-based software-defined λ-Flow architecture for flex-grid OFDMA mobile

backhaul over passive optical networks with filterless direct detection ONUs," in *Optical Fiber Communication Conference (OFC)*, 2013, paper PDP5B.2.

[18] M. Bolea, R. P. Giddings, and J. M. Tang, "Digital orthogonal filter-enabled optical OFDM channel multiplexing for software-reconfigurable elastic PONs," *J. Lightwave. Technol.*, vol. 32, no. 6, pp. 1200-1206, 2014.

[19] X. Q. Jin and J. M. Tang, "Experimental investigation of wavelength spacing and colorlessness of RSOA-based ONUs in real-time optical OFDMA PONs," *J. Lightw. Technol.*, vol. 30, no. 16, pp. 2603-2609, 2012.

[20] E. Al-Rawachy, R. P. Giddings, J. M. Tang, "Experimental demonstration of a DSP-based cross-channel interference cancellation technique for application in digital filter multiple access PONs," *Opt. Express*, vol. 25, no. 4, pp. 3850-3862, 2017.

5. DFMA PONs with DSP-Enabled Software Reconfigurability

Contents

5.1 Introduction

As described in Chapter 2, CANs provide an integrated platform containing converged metro, access and mobile front/backhaul networks, so having investigated the software reconfigurable optical transceivers and ROADMs at the networking device level in the previous chapters, this chapter deals with a novel multiple access PON technique which is at the networking architecture level, designated as digital filter multiple access (DFMA) PON [1]. In a DFMA PON use is made of centralized SDN controller-managed and transceiver-embedded digital orthogonal filters to enable various ONUs to adaptively and dynamically access and share a common fibre transmission medium. It has been shown [1] that the proposed DFMA PONs have a number of salient advantages as listed below:

- Significantly expanded and improved network operation functionalities and reconfigurability in both the electrical and optical domains, along with considerably extended SDN network virtualization and abstraction capabilities added to the physical layer of CANs;
- Excellent network operation transparency to underlying signal modulation/detection technique, signal bandwidth, wavelength grid, multiple access technique and network topology. This feature offers a solid platform for equipping the access network segment of CANs with sufficient network flexibility, adaptability and elasticity. The feature also provides highly desirable backwards compatibility with all existing PONs. In addition, this feature also greatly simplifies the development of universal ONU transceivers in a cost-effective manner;
- The ability to realize the CANs when utilising the flexible ROADMs as described in Chapter 4 capable of performing DFMA-based channel add/drop functions;
- Improved physical layer data security as dynamic digital filter parameters must be known for receiving data;
- Network implementation using a “pay as you grow” operation model, as new DFMA channels can be added to CANs on-line as required.

To explore major DFMA PON aspects related to their practical implementation, in this chapter, experimental demonstrations of multipoint-to-point upstream OOFDM signal transmission in IMDD-based DFMA PONs incorporating real-time digital orthogonal

filtering-enabled reconfigurable ONUs are first undertaken. Given the fact that the DFMA PON downstream transmission performance is very similar to that corresponding to a digital orthogonal filtering-enabled point-to-point PON system as described in Chapter 3, the work in this chapter focuses on the more challenging upstream DFMA PON transmission, where two orthogonal channels occupying the same signal spectral region are optically combined passively in an OC at the remote note. In addition, to investigate the DFMA PON upstream performance characteristics, comprehensive experimental investigations are also undertaken of ONU reconfigurability-induced power penalties, and ONU BER performance sensitivity to both sample timing offset (STO) between different upstream ONUs as well as the ONU differential launch power variation range. Furthermore, as channel frequency response roll-off influences the orthogonality between the spectrum-sharing orthogonal DFMA channels and leads to CCI and subsequent system performance degradation in DFMA PONs, the impact of various levels of channel frequency response roll-off on upstream transmission performance are numerically investigated in a 2-ONU DFMA PON system. The work presented in this chapter not only confirms the feasibility of the DFMA concept but also provides insights into the DFMA PON aspects associated with its practical implementation for future CANs.

5.2 DFMA PONs Operating Principles

As illustrated in Fig. 5.1, a DFMA PON is very similar to the point-to-point digital orthogonal filtering-based channel multiplexing PON system described in Chapter 3 as it employs the same channel multiplexing technique with the differences that 1) in a multipoint-to-point DFMA PON ONU channels are multiplexed in the optical domain; 2) synchronisation is required between different ONUs and 3) the ONU can process one or more digital orthogonal filtered channels and the OLT process all the channels. For the upstream operation, each ONU first digitally generates data encoded with an arbitrary signal modulation format, the produced signal is then M× up-sampled by inserting M-1 zeroes between two successive samples of the original data. The up-sampled data sequence is then digitally filtered with a dynamically reconfigurable digital SF. The digitally filtered data sequence is converted to an analogue electrical signal via a DAC. Finally, electrical-to-optical (E-O) conversion is performed by an optical IM. Optical signals from various ONUs, each generated with a different digital shaping filter, are all passively combined by an OC

in the remote node, and the combined optical signal propagates through the fiber transmission link to the OLT.

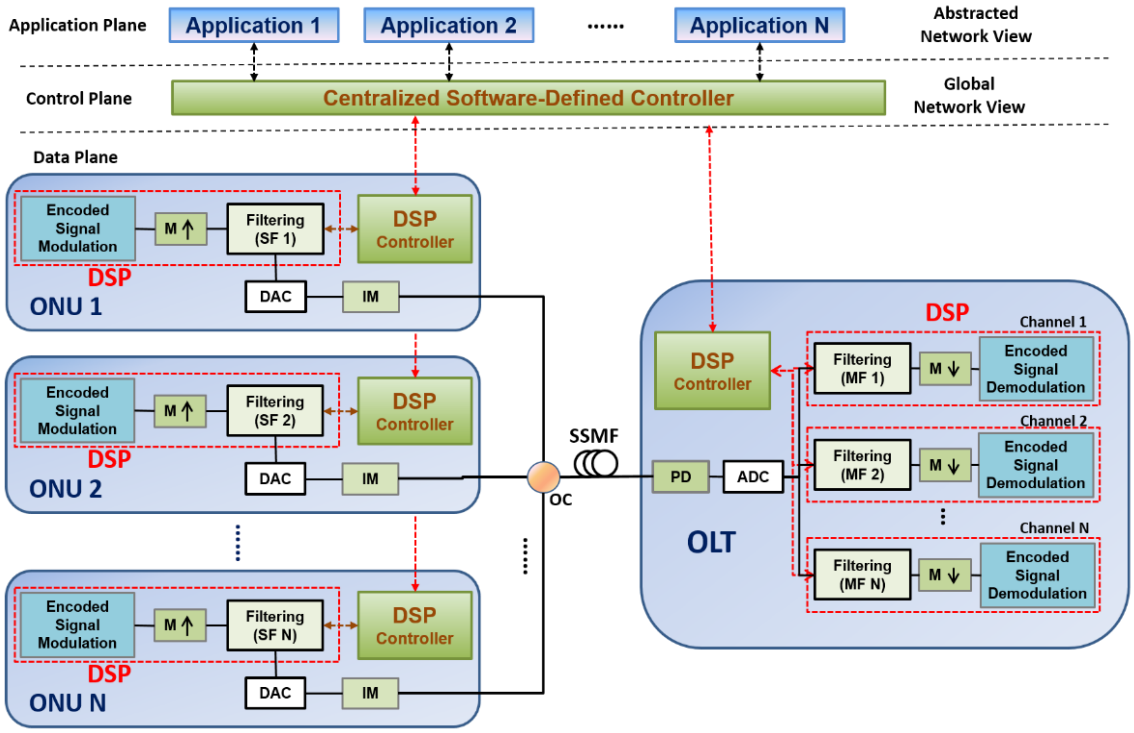

Fig. 5.1. Proposed DFMA PONs architecture supporting the SDN paradigm.

In the OLT receiver, the optical signal is detected by a square-law photodetector (PD) to convert the signal from the optical domain to the electrical domain. After that, the electrical signal is amplified, analogue low-pass filtered and subsequently digitized by an ADC. Next, the data stream is digitally filtered by a MF suitably configured with the appropriate coefficients corresponding to the specific ONU signal to be demultiplexed. The filtered signal is then down-sampled by selecting every M-th sample with the optimum phase. Data from the specific ONU is finally recovered by allowing for any underlying multiple-access schemes (if any) and also by applying suitable demodulation for the modulation format employed by the associated ONU.

In practice, a centralized SDN controller would be connected to the OLT and ONUs via network embedded control channels so the control channels are supported by the existing network infrastructure, it would of course be impractical to implement dedicated physical connections for the SDN control. The embedded SDN control channel between the OLT and ONUs can be realised by allocating a small part of the ONU's bandwidth as a low-bandwidth

control channel. Based on the currently active services and dynamic network traffic characteristics, the centralized SDN controller, which is aware of the corresponding send/receive SDN control information for each ONU, negotiates with the OLT and ONU-embedded DSP controllers, via extended OpenFlow [5], to determine all sets of digital filter coefficients to perform the shaping (matching) filtering process required by each individual ONU (the OLT). This leads to the flexible creation of software-reconfigurable elastic connections at the physical layer. In addition, the OLT-embedded DSP controller oversees the DFMA channel allocation, and takes full responsibility for maintaining the orthogonality between all channels employed in the DFMA PON.

5.3 Experimental Demonstrations of Upstream DFMA PONs

5.3.1 Experimental System Setup

Fig. 5.2 illustrates the considered DFMA PON upstream experimental system setup, which consists of two independent real-time ONUs feeding a 3dB optical coupler, a 26.4km SSMF IMDD transmission link and an offline OLT with a PIN+TIA. According to our numerical simulation results [1], for a specific ONU, the cross-talk effect between two ONUs

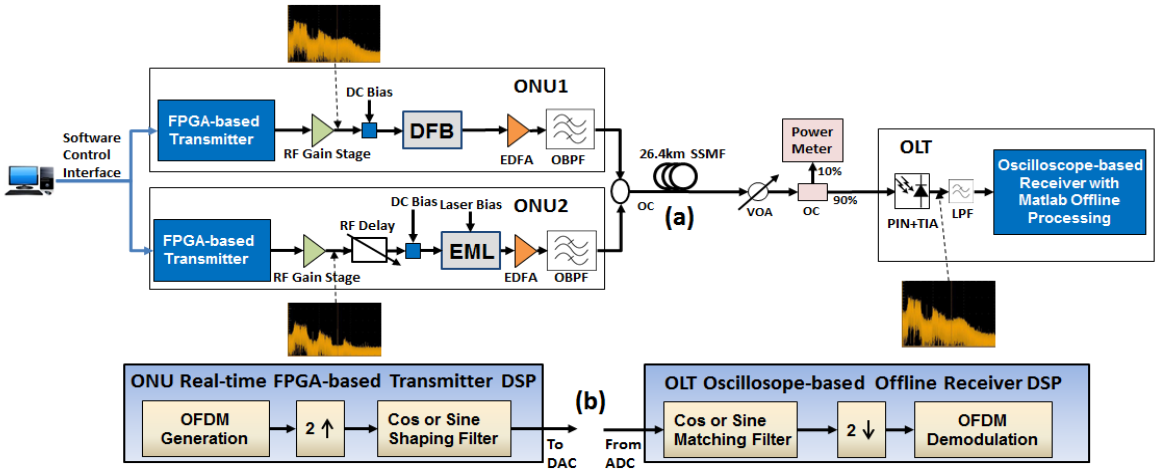

Fig. 5.2. (a) Upstream DFMA PON experimental system setup; (b) Major DSP functions in both the ONUs and the OLT. The insets are the electrical spectra of the ONU and OLT signals. DFB: distributed feedback laser, EML: electro-absorption modulated laser, EDFA: Erbium-doped fiber amplifiers, OBPF: optical band-pass filter, VOA: variable optical attenuator, OC: optical coupler, SSMF: standard single-mode fiber, PIN+TIA: photodetector with integrated transimpedance amplifier.

occupying the same spectral region has a significant impact on the maximum achievable upstream performance of the ONUs, whilst the cross-talk effect between all other ONUs occupying different spectral regions is almost negligible. For simplicity but without loss of generality, in this chapter, two ONUs named ONU1 and ONU2 are considered, each utilizing an entire I or Q channel constructed by a single Hilbert-pair filter of the same central frequency. ONU1 is composed of an FPGA and an 8bit at 2GS/s DAC-based real-time software reconfigurable OOFDM transmitter described in section 3.4 of chapter 3, where a 10GHz directly modulated distributed feedback (DFB) laser (DML) is employed to perform the E-O conversion. An EDFA followed by an optical filter is also utilized to set the optical launch power at a desired level. The architecture of ONU2 is almost identical to ONU1, except that in ONU2 a 10GHz electro-absorption modulated laser (EML) is employed as an intensity modulator (IM) and an electrical RF delay line is also introduced to alter the inter-ONU STO. The employment of different intensity modulators in various ONUs enables rigorous evaluations of the DFMA PON upstream performance robustness to different intensity modulator types.

As seen in Fig. 5.2 (a) and (b), in each individual real-time ONU transmitter, after generating a pseudo random binary sequence (PRBS)-based OFDM signal in the corresponding FPGA, the digital signal is first 2× up-sampled by introducing a zero-valued sample between two consecutive original samples. The up-sampled digital signal consisting of 16 parallel samples is then filtered by a bank of 16 parallel 32-tap finite impulse response (FIR) digital shaping filters to generate an I signal for ONU1 or a Q signal for ONU2. Furthermore, a single I or Q signal can also be shared by two or more ONUs using a multiple access method such as OFDMA [6].

To implement the embedded digital orthogonal filters in the real-time transmitters, the OFDM generation and filtering in the real-time ONU is the same as in the digital orthogonal filter-based transmitter in chapter 3 except that here only one channel is enabled in each transmitter. Two Hilbert-pair-based shaping filters as defined in Eq. 3.10 are employed. As the filter pair central frequency f_c is 500MHz and the sampling time interval T_s is 500ps the discrete impulse responses are:

$$s_1(k) = g(k)cos(\pi k/2) \tag{5.1}$$

$$s_2(k) = g(k)sin(\pi k/2) \tag{5.2}$$

where k = 0, 1, 2, …, 31, and $g(k)$ is the baseband pulse as defined in Eq. 3.11 with M=2 and α = 0. After having passed through a DAC, a RF gain stage, and combined with an optimized bias current, the digitally filtered OFDM signal directly drives the corresponding optical intensity modulator in each ONU. The inter-ONU STO between these two ONUs is optimized using the RF delay line included in ONU2. The optical launch power from each

Table 5.1 Transceiver and System Parameters

Parameter	Value	Unit
Total number of IFFT/FFT points	32	/
Data-carrying subcarriers	6 at highest frequencies	/
Adaptive subcarrier modulation formats	16-QAM, 32-QAM	/
Number of filter taps	32	/
DAC sample rate	2	GS/s
DAC resolution	8	bits
DSO sample(resample) rate	25(2)	GS/s
OFDM symbol rate	25	MHz
Samples per OFDM symbol$^{\alpha}$	32 (16ns)	samples
Cyclic prefix$^{\alpha}$	8 (4ns)	samples
Total samples per OFDM symbol$^{\alpha}$	40 (20ns)	samples
Signal clipping ratio	13	dB
Raw signal line rate per ONU	0.75	Gb/s
EML laser operating wavelength	1550.948	nm
3dB EML modulation bandwidth	10	GHz
EML bias current	125	mA
EAM bias voltage	-0.7	V
EML driving voltage	1.56	V_{pp}
DFB laser operating wavelength	1550.745	nm
3dB DFB modulation bandwidth	10	GHz
DFB laser bias current	42	mA
DFB laser driving voltage	295	mV_{pp}
PIN detector bandwidth	12	GHz
PIN detector sensitivity$^{\beta}$	-19	dBm

α Before up-sampling / after down-sampling
β Equivalent to 10 Gb/s NRZ data (PRBS 2^{31}-1) at a BER of 1×10^{-9}

ONU is fixed at 4dBm. These two upstream OOFDM signals occupying the same spectral region (0-1GHz) but different locations in the digital filter space, are subsequently passively combined in the optical domain with a 3dB optical coupler, and the combined optical signals propagate to the OLT through a 26.4km SSMF link. Both the 4dBm optical launch power from each ONU and the 26.4km SSMF length are chosen to represent typical PON scenarios.

In the OLT, a variable optical attenuator is utilized to vary the received optical signal power before injecting into a 12.4GHz PIN with a receiver sensitivity of -19dBm. After passing

through a 2GHz electrical low-pass filter, the converted signal is sampled at 25GS/s by a real-time digital sampling oscilloscope (DSO) and subsequently processed off-line using MATLAB for recovering data from either ONU1 or ONU2. The major OLT receiver DSP functions include: down-sampling to 2GS/s, selecting the optimum STO, filtering with a digital matching filter selected according to the ONU data to be recovered, 2× down-sampling, OFDM symbol synchronisation, detection of pilot subcarriers and channel estimation/equalization, as well as other DSP functions that are inverse to the transmitter's DSP counterparts. The selected digital matching filter frequency response satisfies:

$$m_1(k) = s_1(31-k) \tag{5.3}$$

$$m_2(k) = s_2(31-k) \tag{5.4}$$

with

$$s_i(k) \otimes m_j(k) = \begin{cases} \delta(k-k_0) & i=j \\ 0 & i \neq j \end{cases} \tag{5.5}$$

where k_0 is to the overall discrete time delay due to both filters. The optimum IM operating conditions adopted are: a DFB bias current of 42mA, an EML laser bias current of 125mA and an EML bias voltage of -0.7V, as well as a driving signal level of 295mV$_{pp}$ (1.56V$_{pp}$) for the DFB (EML). The wavelength of the DML is fixed at 1550.745 nm, whilst the wavelength of the EML is kept at 1550.948 nm. According to our experimental measurements [10], such a wavelength spacing between different ONUs is sufficiently large to completely eliminate the optical beat interference (OBI) effect associated with direct detection of the combined upstream signals in the OLT.

Due to finite tap count-induced digital filter frequency response ripples and channel frequency response roll-off-induced cross-talk between two spectrally overlapped DFMA channels [1, 3], only the 6 highest frequency subcarriers (out of 15) are used for each ONU to avoid the occurrence of excessive errors on the lower frequency subcarriers. It is, however, expected that all 15 subcarriers could be used by applying a recently proposed cross-channel interference cancellation (CCIC) technique [8]. The key transceiver and system parameters are summarized in Table 5.1. Based on Table 5.1 and taking into account the adopted signal modulation formats, the raw upstream signal transmission capacity per ONU is ~0.75Gb/s, and the raw aggregated upstream DFMA PON transmission capacity is thus ~1.5Gb/s. The

net upstream signal transmission capacity per ONU is ~0.6Gb/s and the net aggregated upstream DFMA PON transmission capacity is ~1.2Gb/s because of the following two reasons: a) a pilot subcarrier insertion approach reported in [22] is used, which requires negligible signal bandwidth, and b) a 25% OFDM cyclic prefix is considered, as presented in Table 5.1. Here it is also worth addressing that accurate synchronisation between two orthogonal upstream ONU signals occupying the same spectral region in a DFMA PON is vital for maximizing the ONU upstream transmission performance. In contrast, no synchronisation is required between ONU signals occupying different spectral regions. According to our numerical simulations [1], no spectral guardband is necessary between two adjacent spectral regions. By making use of our previously published synchronisation approach [10, 11], and considering the fact that the received signal at the DSO is sampled at 25GS/s, the following synchronisation approach is adopted here, which is experimentally proven to be very effective at achieving accurate synchronisation:

- In the initial phase of establishing an upstream DFMA PON system, ONU1 is switched on and ONU2 is switched off. In the OLT, after the ADC function within the DSO, the digitized signal is first resampled to 26GS/s, and then down-sampled to 2GS/s by selecting every 13th sample, the signal is subsequently passed through a corresponding matching filter, down-sampled by a factor of 2 and finally OFDM demodulated for BER calculations.
- A comprehensive sweep of sample offset (at 26GS/s) across two consecutive sample intervals (at 2GS/s) with a total sweep time interval of 1ns is conducted. By comparing the BER performances for different sample offsets, the samples for optimum timing can be easily identified for ONU1.
- Having synchronised ONU1, ONU2 is then switched on. After applying the relevant procedures mentioned above, the inter-ONU STO between these two ONUs is then optimized using the RF delay line included in ONU2. The RF delay is adjusted to minimise the BER on both channels.

It should also be addressed that, to easily differentiate the upstream signals emerging from ONU1 and ONU2, different signal modulation formats are implemented in ONU1 where 32-QAM is taken only on the 15th subcarrier and 16-QAM is taken on all other data-carrying subcarriers. Such signal modulation format manipulation is not necessary for practical

application scenarios. On the other hand, all the data-carrying subcarriers in ONU2 are encoded using 16-QAM.

5.3.2 Experimental Results

Having outlined the DFMA PON operating principle in Section 5.2 and described the experimental upstream system setup in Section 5.3.1, this section is dedicated to extensively exploring key upstream DFMA PON performance properties, which include ONU BER performance, ONU reconfigurability-induced power penalties, and performance tolerance to inter-ONU STO as well as differential ONU launch power variation range. Understanding these issues is of great importance for system design.

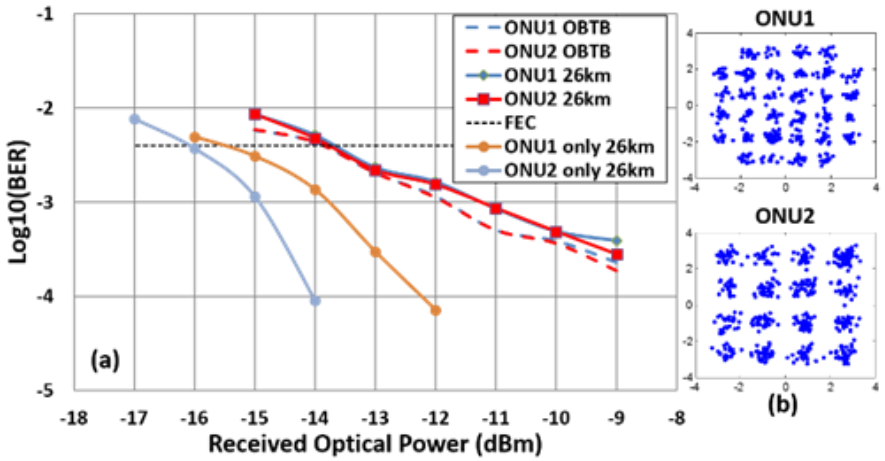

Fig. 5.3. (a) BER performance of aggregated 1.5Gb/s OOFDM upstream transmission over 26.4 km SSMF IMDD DFMA PON systems; (b) Example of received constellations of the 15th subcarriers for both ONU1 and ONU2.

5.3.2.1 Upstream DFMA PON BER performance

The upstream ONU BER performances versus received optical power (ROP) for optical back-to-back (BTB) and 26.4km SSMF transmission are both plotted in Fig. 5.3(a), which shows almost identical BER performances for both ONUs, as theoretically predicted in [1]. At the adopted FEC limit of 4×10^{-3} (this limit is used in this chapter to maintain good operating ONU launch power variation range in section 5.3.2.3 although there is a penalty of higher FEC overhead), for both ONUs, negligible power penalties are also observed, compared to the corresponding optical back-to-back cases. All these results mentioned above indicate that the DFMA PON upstream performance exhibits excellent robustness to different IM types.

To explore the ONU reconfigurability-induced optical power penalty, Fig. 5.3(a) presents the BER performance of each ONU with the other ONU deactivated. Fig. 5.3(a) emulates the worst-case reconfiguration scenario where one ONU's IM driving current is turned off and its corresponding optimum IM bias current is still active. Fig. 5.3(a) shows that, at the assumed FEC limit, the DSP-enabled ONU reconfigurability-induced optical power penalty is 1.8dB (2.3dB) for ONU1 (ONU2). It is also expected that the power penalties for the worst-case scenarios can be considerably reduced when the reconfigurability takes place between different ONUs utilizing digital filters at different central frequencies. Moreover, in comparison with the case where two ONUs are activated simultaneously, the existence of a single active ONU produces a sharper BER developing curve, as seen in Fig. 5.3(a). This is very similar to the previous experimental results measured in a point-to-point system in section 3.4 of chapter 3. This confirms the theoretical predictions [1] that the cross-talk effect between two spectrally overlapped ONUs is a major physical mechanism underpinning the minimum attainable BERs of the DFMA PON. This suggests that the optical power penalty is independent of the ONU count in the DFMA PON. Here it is also worth pointing out that the cross-talk effect can be substantially diminished by employing the CCIC technique [8]. For two active ONUs and a ROP of -9dBm, the representative equalized constellations of the15th subcarriers are shown in Fig. 5.3(b).

5.3.2.2 Tolerance to inter-ONU STO

As mentioned previously, achieving suitable timing synchronisation between ONUs occupying the same signal spectral region is essential for the DFMA PON. Thus, the upstream ONU BERs as a function of inter-ONU STO are plotted in Fig. 5.4, where STO = 0 represents an ideal timing relationship between these two involved ONUs. In obtaining Fig. 5.4 the inter-ONU STO is varied by adjusting the electrical RF delay line in ONU2 with ONU1 being kept at its optimum synchronised status. In measuring Fig. 5.4, the optical launch power of each ONU is fixed at 4dBm, and the total ROP at the OLT remains at -9dBm. Physically speaking, when the STO varies within the sample period of 500ps, an unwanted signal power leakage between the two spectrally overlapped ONUs occurs, which grows with increasing STO. As such, it is shown in Fig. 5.4 that to maintain upstream ONU BERs below the adopted FEC limit, both ONUs can tolerate an inter-ONU STO as large as 0.22ns, which is approximately 44% of the sample interval of 500ps. Modern clock timing circuits are capable of easily achieving the timing stability within such a range.

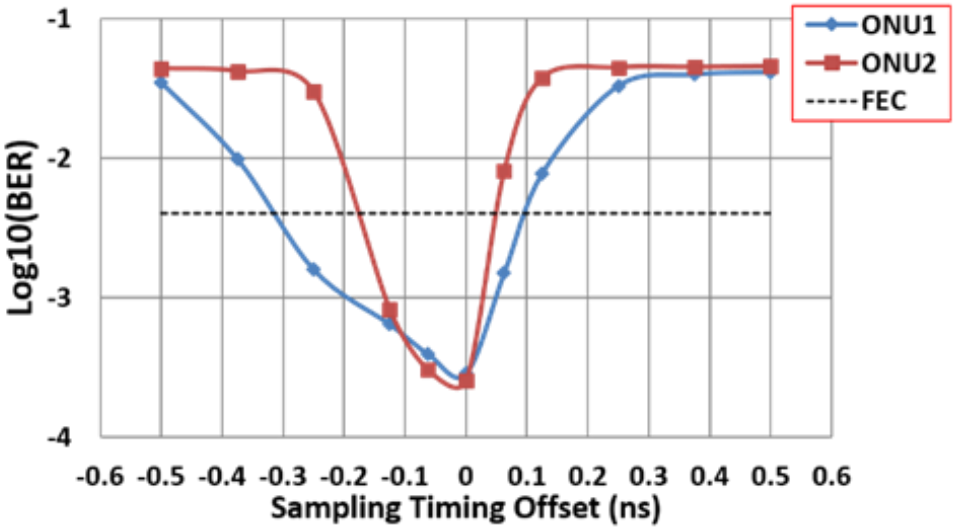

Fig. 5.4. ONU BER performance tolerance to inter-ONU STO

It is also interesting to note in Fig.5.4 that ONU2 is more sensitive to STO than ONU1. This is due to the fact that, the status of STO = 0 for ONU1 always maintains the optimum timing relationship between its associated shaping and matching filters, and so it only suffers power leakage from ONU2 due to the inter-ONU STO induced degradation in orthogonality. Whereas, the performance of ONU2 degrades as its STO deviates further from the ideal state. The recovered signal from ONU2 will not suffer increased leakage from ONU1 as timings and delays related to ONU1 are unchanged. Fig. 5.4 shows that the STO variation of ONU2 has a greater impact than the associated increased leakage on ONU1. Therefore, as shown in Fig. 5.4, the ONU which experiences the timing delay exhibits higher inter-ONU STO sensitivity than the ONU where timing delay was unchanged. From the above analysis, it is easy to appreciate that the DFMA PON's tolerance to inter-ONU STO can be considerably improved when further digital filter optimizations are made. It should also be pointed out, in particular, that the aforementioned STO-induced power leakages are negligible between ONUs occupying different signal spectral regions.

5.3.2.3 ONU launch power variation range

For a specific ONU, the launch power variation range is defined as the maximum allowable variation in its optical launch power, for a given ROP at the OLT, which maintains the BERs of all simultaneously transmitting ONUs below the adopted FEC limit. To examine the achievable ONU launch power variation range for the considered DFMA PON, Fig. 5.5 is presented, where the BER performances of all upstream signals are plotted against optical

launch power of each individual ONU. In obtaining Fig. 5.5, an EDFA is used to vary the optical launch power emerging from the variable-power ONU, whilst the optical launch power from the fixed-power ONU is always kept at a constant value of 4dBm. The ROP at the OLT remains at -9dBm.

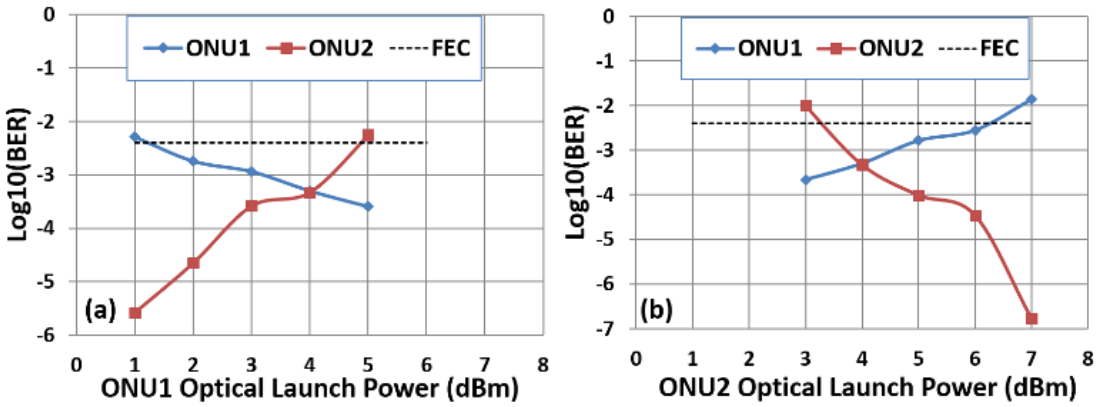

Fig. 5.5. ONU launch power variation range for the DFMA PON. (a) The optical launch power from the DML-based ONU1 varies and the optical launch power from the EML-based ONU2 is fixed at 4dBm. (b) The optical launch power from the DML-based ONU1 is fixed at 4dBm and the optical launch power from the EML-based ONU2 varies.

It is observed in Fig. 5.5 that, for a fixed total ROP of -9dBm in the OLT, increasing the optical launch power from the variable-power ONU improves its own BER performance and simultaneously degrades the BER performance of the fixed-power ONU. This mainly results from the variation in the effective optical signal-to-noise ratio (OSNR) of the corresponding upstream optical signals. It can be easily seen in Fig. 5.5(a) and Fig. 5.5(b) that the ONU launch power variation ranges are approximately 3.8dB for ONU1 and 3.0dB for ONU2. The observed launch power variation ranges are mainly attributed to three major physical mechanisms: the cross-talk effect induced by the imperfect ONU filter orthogonality, the non-ideal channel frequency response, and the relatively low extinction ratios of the intensity modulated optical signals [9]. Very similar launch power variation ranges have also been experimentally observed in OOFDMA PONs [10]. For a practical DFMA PON, its upper limit of the launch power variation range is determined by the minimum OSNR allowed by the fixed-power ONU, whilst its lower limit of the launch power variation range is determined by the minimum OSNR allowed by the variable-power ONU. In addition, it is also seen in Fig.5 that the minimum achievable BERs for ONU2 are lower than those for ONU1 for all the cases, this is because the EML employed in ONU2 has better intensity modulation performance characteristics compared to the DML employed in ONU1.

5.4 Performance Tolerance of IMDD DFMA PONs to Channel Frequency Response Roll-off

In the previous section, multipoint-to-point optical OFDM (OOFDM) upstream transmissions of IMDD DFMA PONs have been experimentally demonstrated, where individual Hilbert pair-based digital orthogonal filters are assigned to two spectrally overlapped orthogonal channels occupying a common spectral region. As such, the channel frequency response roll-off characteristics influenced the orthogonality between the channel pair, leading to cross-channel interference (CCI) and subsequent system performance degradation. A straightforward approach is to use digital pre-emphasis in the transmitter to compensate such roll-off. The pre-emphasis works by attenuating the lower frequencies (not amplifying higher frequencies) of the transmitted signal before the DAC. Thus the lower frequencies of the signal will suffer a performance degradation due to the quantisation effect and reduced SNR. The drawback of the above method is that it generally only works for lower roll-offs but is not effective for large roll-offs. To effectively mitigate the channel frequency response-induced CCI, a DSP-based CCI cancellation (CCIC) technique has been proposed and experimentally demonstrated in a point-to-point IMDD DFMA PON system [11]. Also a more comprehensive DSP-based DFMA channel interference cancellation (DCIC) technique has been numerically investigated in multipoint-to-point IMDD DFMA PONs [12].

As component, transceiver and system designs ultimately determine total system frequency response, it is highly beneficial to explore the IMDD DFMA PON performance robustness to various levels of channel frequency response roll-off (here on "channel roll-off"), as such studies can: i) offer insights into optimum PON operating conditions where CCIC becomes unnecessary, allowing further simplifications of both transceivers and PON architectures without considerably compromising the overall PON performance; and ii) indicate the feasibility of utilising low-cost and narrowband electrical and optical components. This is essential for achieving the optimum balance between PON installation and operation costs and the required PON performance. To explore the aforementioned performance robustness, this chapter details performance comparisons between experimental measurements and numerically simulated results, and analyses the impacts of channel roll-off on upstream IMDD DFMA PONs in terms of BER versus received optical power (ROP), maximum

achievable ONU capacity, ONU launch power variation (LPV) range, and tolerance to inter-ONU sampling time offset (STO). Here we focus on upstream PON performance as this is subject to more variations in its operating conditions, resulting from the independently operating ONUs. Furthermore, a two ONU PON is considered sufficient for the analysis as roll-off induced CCI is only dependent on roll-off within orthogonal sub-bands.

5.4.1 IMDD DFMA PONs Numerical Simulation System

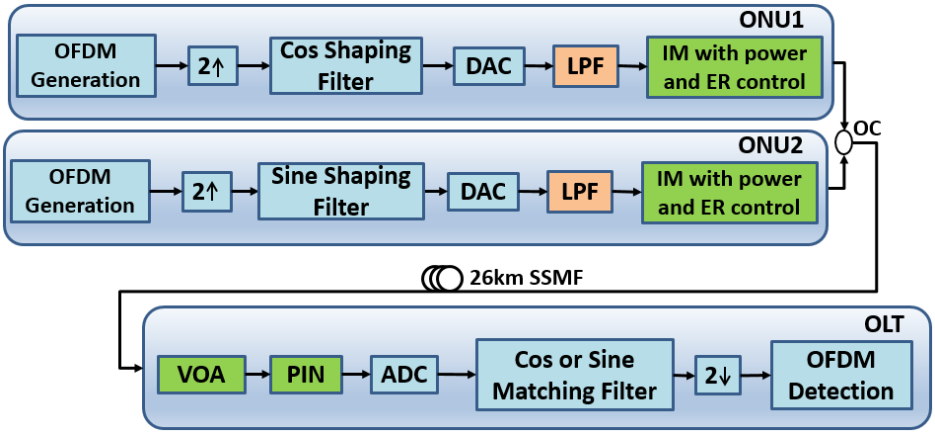

Fig. 5.6. DFMA PON system model adopted in the simulation.
(DAC: digital-to-analogue converter, ADC: analogue-to-digital converter, OC: optical coupler)

Fig. 5.6 illustrates the considered two ONU IMDD DFMA PON, which is identical to that employed in experimental measurements in chapter 5, except that in Fig. 5.6 an electrical low pass filter (LPF) is introduced in each ONU to take into account the roll-off effect attributed by relevant analogue electrical and optical components. As shown in Fig. 5.6, the upstream signal DSP and transmission processes can be described as follows: in each ONU transmitter, a digital OFDM signal is firstly generated and then 2× up-sampled by adding a zero-valued sample between two consecutive original samples. The up-sampled digital signal is filtered by a 32-tap finite impulse response (FIR) digital shaping filter to generate an in-phase signal for ONU1 (cosine filter) or a quadrature-phase signal for ONU2 (sine filter). After passing through a 2GS/s, 8-bit DAC and the LPF, the electrical signal is utilized to drive an intensity modulator (IM) in the corresponding ONU. Each ONU's optical signal power is fixed at 4dBm. After passively combining these two upstream DFMA signals in an optical coupler, the combined optical signals propagate along a 26km SSMF to the OLT.

In the OLT, the ROP of the optical signal is adjusted with an optical attenuator. The received optical signal is detected with a 12.5 GHz PIN with a receiver sensitivity of -19 dBm. The detected electrical analogue signal is converted into the digital domain using a 2GS/s, 8-bit ADC. Finally, the major OLT receiver DSP procedures include: filtering by a digital matching filter selected according to the ONU data to be recovered, 2× down-sampling and OFDM signal recovery, including an ultra-low overhead (0.001%) pilot-subcarrier based channel estimation/equalization function and a zero overhead symbol alignment algorithm. It should also be noted the ONUs and OLT use a common 2GHz sample clock providing zero sampling frequency offset.

In performing numerical simulations, an IMDD DFMA PON theoretical model detailed in [1] is adopted, where an approach published in [13] is employed to simulate the OOFDM signal generation, transmission and detection. Here all experimentally measurable transceiver/PON parameters used in the last section are also adopted, which are summarized in Table 5.2. In numerical simulations, different channel roll-off levels are realized by varying the LPF profiles. For simplicity, the roll-off value, *R*(dB), is defined as the LPF attenuation at the Nyquist frequency (1GHz for all the cases considered here). The various LPF magnitude responses used in the performance analysis are plotted in Fig. 5.7. The optical signal extinction ratio (ER) [14] in each ONU is finely adjusted to ensure good agreement between numerical simulations and the experimental measurements in Section 5.3, for all the different measurement scenarios. The introduction of the LPF profiles and suitable signal ERs allows the utilization of an ideal intensity modulator in each ONU. As a direct result, the intensity modulation-induced frequency chirp is also negligible.

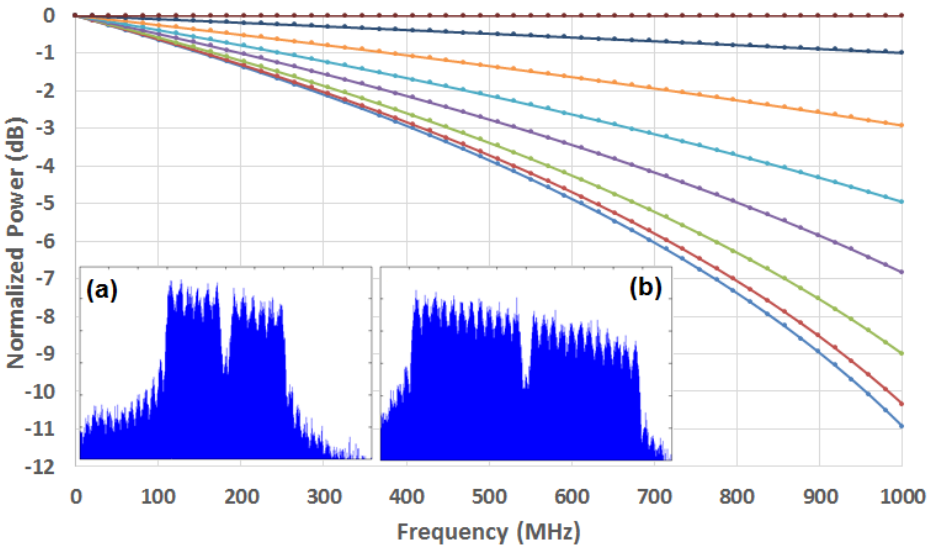

Table 5.2 System Parameters

Parameter	Value	Unit
Total number of IFFT/FFT points	32	/
Data-carrying subcarriers	6 or 12 at highest frequencies	/
Subcarrier modulation format	16-QAM	/
Subcarrier frequency spacing	31.25	MHz
Up-sampling factor	2	/
Digital filter length	16	/
OFDM symbol rate	25	MHz
Samples per OFDM symbol$^{\alpha}$	32	samples
Cyclic prefix$^{\alpha}$	8	samples
Total samples per OFDM symbol$^{\alpha}$	40	samples
OFDM signal clipping level	13	dB
DAC/ADC sample rate	2	GS/s
DAC/ADC resolution	8	bit
Excess of bandwidth of digital filters	0	/
Orthogonal sub-band bandwidth	1	GHz
Maximum total raw bit rate	~3.6	Gb/s
Extinction ratio of IMs	0.49	dB
PIN quantum efficiency	0.8	/
PIN power sensitivity$^{\beta}$	-19	dBm
PIN detection bandwidth	12.5	GHz
Fiber dispersion parameter	17	ps/nm/km
Fiber dispersion slope	0.07	ps/nm^2/km
Fiber loss	0.2	dB/km
Fiber Kerr coefficient	2.35×10^{-20}	m^2/W

α Before up-sampling / after down-sampling
β Corresponding to 10Gb/s NRZ data (PRBS 2^{31}-1) at a BER of 1×10^{-9}

Fig. 5.7. Different frequency response roll-offs introduced by the LPFs. Inset: DFMA electrical signal spectra at R=10dB (a) α=0.43, (b) α=0.81

5.4.2 Parameter Identification and Simulation Model Validation

To identify the optical signal ER and subsequently verify the above-described numerical simulation models, BER versus ROP performance comparisons are made between numerical simulations and experimental results in Section 5.3 by taking into account all the aforementioned transceiver/PON parameters and the experimentally adopted conditions including R=10dB and the six highest frequency subcarriers enabled. The comparisons are shown in Fig. 5.8, in obtaining which the optical signal ER is finely adjusted until the simulated results closely match all the experimental measurements. The resulting optical signal ER is 0.49dB, which is taken to be a constant value throughout the chapter. It can be seen in Fig. 5.8 that a good match between simulated and experimental results is obtained across the entire dynamic ROP range. In addition to the BER versus ROP performance, good

agreements between numerically simulated results and experimental measurements are also achieved in terms of upstream ONU transmission capacity, ONU launch power variation range and inter-ONU STO, as detailed in Section 5.4.3. The above discussions confirm not only the accuracy of the identified ER parameter but also the validity of the numerical simulation models.

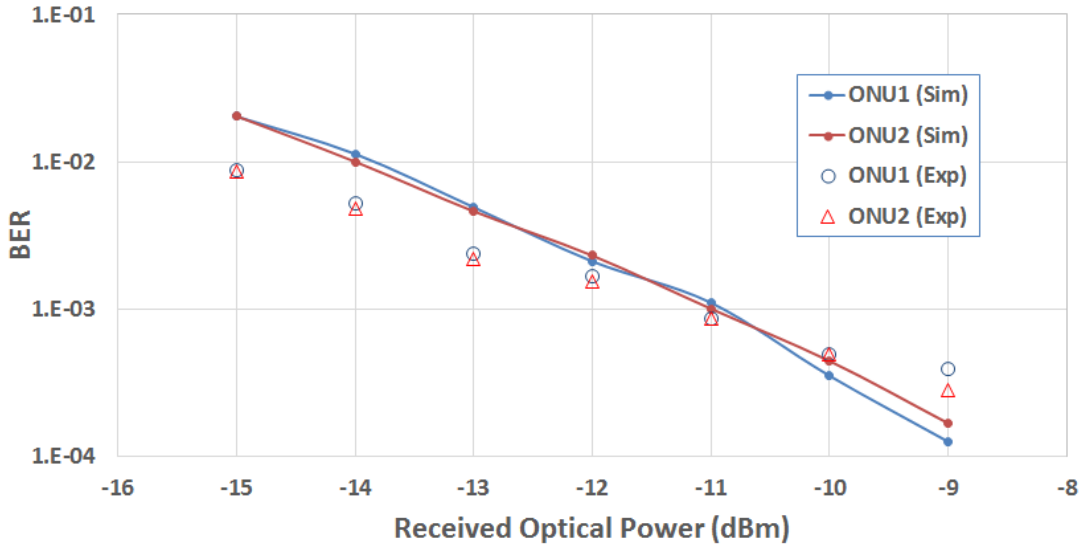

Fig. 5.8. Comparisons of BER versus received optical power performance between simulations and experiments. (Sim: simulations, Exp: experiment).

5.4.3 Upstream ONU Performance Tolerance to Channel Roll-off

By making use of the verified numerical models and the identified ER parameter, in this section detailed explorations are undertaken numerically to investigate the upstream IMDD DFMA PON performance tolerance to channel frequency response roll-off. Fig. 5.9 presents the simulated channel roll-off-dependent ONU upstream transmission capacity together with experimentally measured results. For each ONU, the signal transmission capacity is calculated by considering the subcarriers with BERs of $\leq 4\times10^{-3}$ (FEC limit) only. Fig. 5.9 is plotted using a 0.625Gb/s raw bit rate per ONU as reference, where R=10dB and the 5 highest frequency subcarriers are enabled.

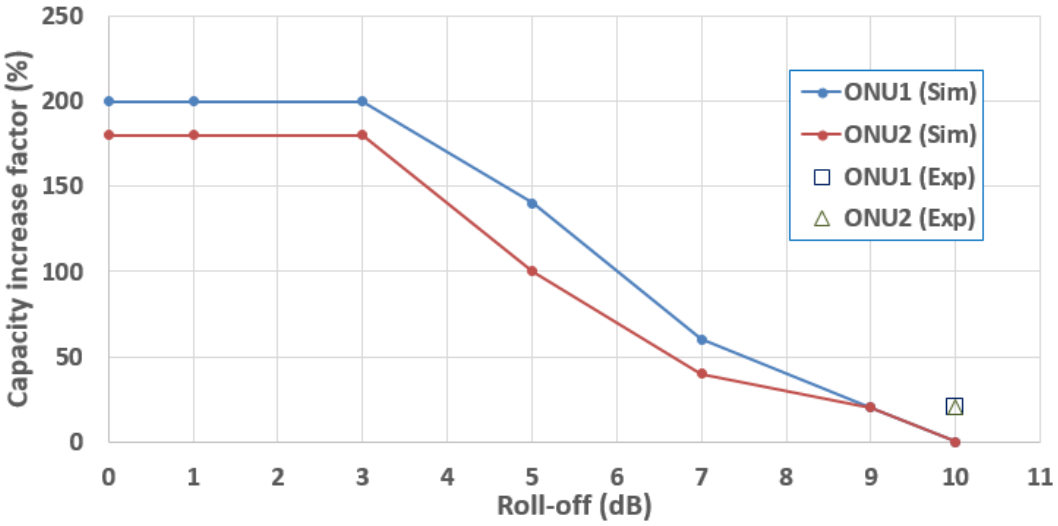

Fig. 5.9. Capacity increase ratio of each ONU versus channel roll-off.

It can be seen in Fig. 5.9 that the ONU transmission capacity can be increased by 200% (180%) for ONU1 (ONU2), when R is reduced from 10dB to ≤3dB. This is because the DFMA signal generation produces a double sideband spectrum, as shown in the inset of Fig. 2, with the original signal spectrum mapped to both the upper and lower sidebands. The channel roll-off effect introduces amplitude variations between the corresponding frequency components in the upper and lower sidebands, this prevents full cancellation between the sidebands of the unwanted signal when these sidebands are mapped back in the DFMA receiver. As such, the CCI effect occurs. In particular, a large roll-off causes a great amplitude variation between the two sidebands, thus lower frequency subcarriers suffer more CCI and more low frequency subcarriers' BERs exceed the FEC limit as the roll-off increases [4]. The ONU transmission capacities saturate to maximum when R≤3dB, where ONU2 can support at most 14 (of 15) subcarriers as the first subcarrier must be dropped due to the high attenuation of its sine filter near the DC component.

As the impact of channel frequency response roll-off also depends upon actual signal bandwidth, performance analysis is performed for the cases of both the 6 and 12 highest frequency subcarriers enabled. Channel bandwidth utilisation factor α is thus defined as the ratio of useful information-carrying signal bandwidth B_{SIG} to maximum available channel bandwidth B_{CH} determined by the Nyquist theorem. For the considered OOFDM cases, B_{SIG} is approximated as $2(N+1)\Delta f$, where N is the number of enabled subcarriers and Δf is the subcarrier frequency spacing. As B_{CH}=1GHz and Δf is 31.25MHz, the value of α is 0.43 (0.81) when 6 (12) subcarriers are enabled.

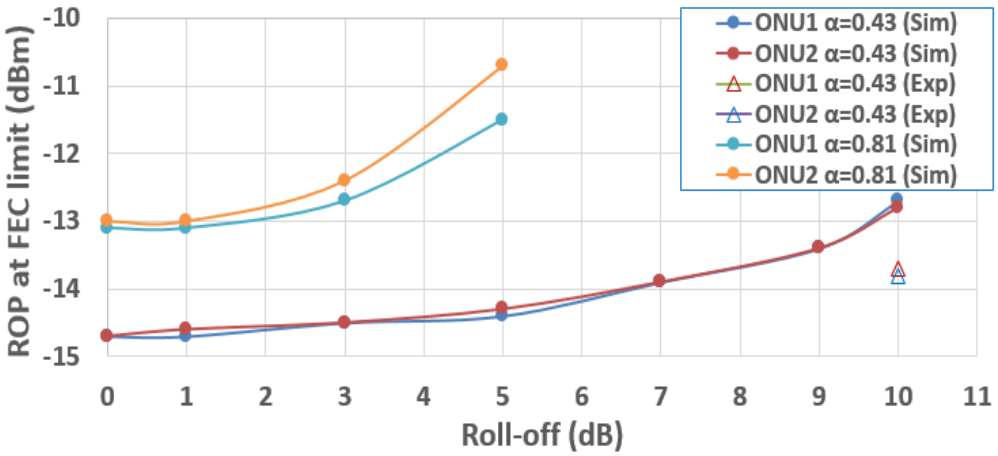

Fig. 5.10. Received optical power at FEC limit versus roll-off.

For α=0.43 and α=0.81, Fig. 5.10 shows the minimum required ROP at the adopted FEC limit versus roll-off. Once again, very similar experimental results are also obtained in the same figure. When α=0.43 (0.81), there is a ~2 dB power penalty when R=10dB (5dB) relative to R=0dB. This indicates that as α increases the ROP sensitivity to roll-off increases. This is due to higher CCIs associated with lower frequency subcarriers, thus the ROP must grow as roll-off and/or α increases in order to maintain the required optical signal-to-noise ratio (OSNR) at the FEC limit.

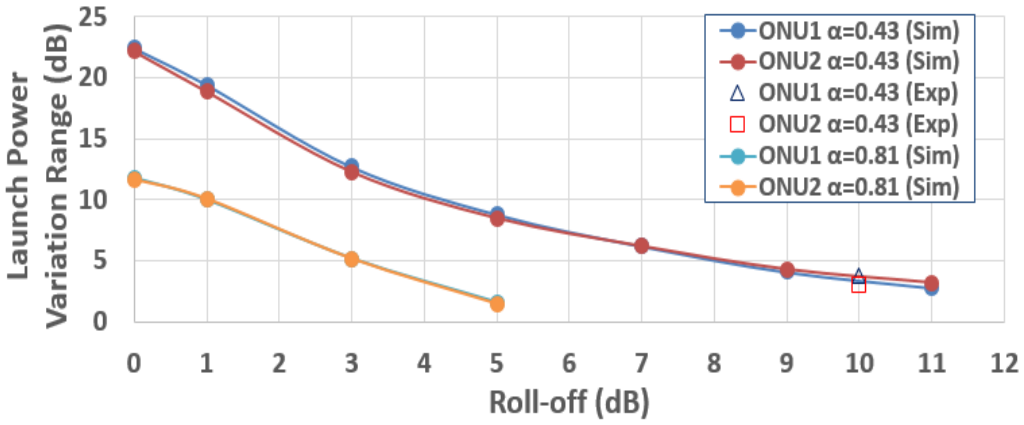

Fig. 5.11. ONU Launch power variation range versus roll-off.

Fig. 5.11 presents the ONU launch power variation range versus channel frequency response roll-off. The ONU launch power variation range is defined as the maximum allowable variation in an ONU's optical launch power for a fixed ROP at the OLT, which maintains the BERs of all ONUs below the adopted FEC limit. In obtaining Fig. 5.11, ONU1's optical launch power is varied from an initial value of 4dBm, whilst ONU2's is fixed at 4 dBm and

the ROP is held at -9 dBm. As ROP is fixed the LPV range limits are found to be roughly symmetrical about 4dBm. The experimental results plotted in Fig. 5.11 show excellent correlation with numerical simulations. Fig. 5.11 shows a fairly rapid reduction in ONU launch power variation range as roll-off increases. This is due to the fact that as the ROP from ONU1 increases the ROP from ONU2 decreases, thus ONU1's CCI from ONU2 decreases, whilst ONU2's CCI from ONU1 increases. Such effect is magnified for higher roll-off-induced CCI. In addition, there is a ~8dB reduction in ONU launch power variation range for a given roll-off for α=0.81 in comparison with α=0.43, indicating that ONU launch power variation range is also sensitive to α.

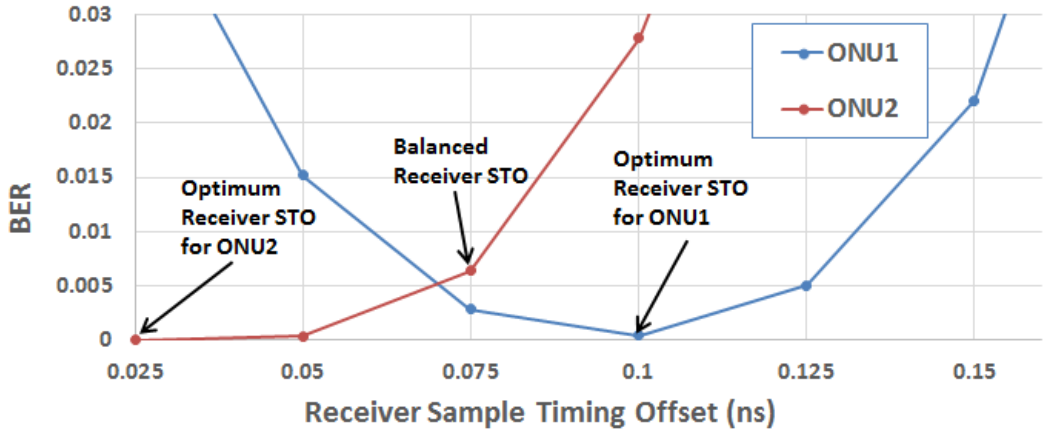

Fig. 5.12. Example of ONU BER versus receiver STO when the inter-ONU STO is 0.075 ns at 10 dB roll-off and α=0.43.

As channel orthogonality is dependent on sample timing synchronization between two spectrally-overlapped orthogonal channels, numerical explorations are also made of the upstream performance tolerance to inter-ONU STO (IOS) at various channel roll-offs. Here the IOS range is defined as the maximum signal time delay adjustment range of one ONU to maintain both ONU BERs below the adopted FEC limit. To finely control the IOS, in each ONU the electrical signal after the DAC is firstly up-sampled from 2GS/s to 40GS/s. Then an adjustment of the time delay is made to the electrical signal from ONU2 at a resolution of 25ps. In the OLT, after the ADC, the digital signal is down-sampled from 40GS/s back to 2GS/s. To find the required receiver STO, a comprehensive sweep across two consecutive original sample intervals totalling 1ns is conducted in order to compare the BER against receiver STO for each ONU. To determine the required receiver STO, two approaches are investigated: i) select the same receiver STO for both ONUs with their BERs kept minimized and as close as possible, referred to as "balanced BER", and ii) select separate receiver STO

for each ONU for minimum BERs, referred to as “optimum BER”. The first approach is necessary when both channels are received in the same transceiver incorporating a common ADC, and the second approach is applicable when an independent ADC is employed for each channel.

For the abovementioned balanced and optimum approaches, examples of BER versus receiver STO are plotted in Fig. 5.12, and the corresponding IOS range variations with roll-off are shown in Fig. 5.13, where again the experimental results match very well the simulations. The results in Fig. 5.13 reveal that: i) a sharp roll-off-induced large CCI leads to a reduced IOS range; ii) the IOS range is significantly lower for the balanced case, thus employing independent channel ADCs considerably reduces timing synchronization requirements between ONUs, and iii) a high α value reduces the IOS range for a specific roll-off, thus the maximum required α value dictates the maximum roll-off for a fixed IOS range. The worst-case IOS range in Fig. 6.8 (0.1 ns) is easily accommodated with modern timing delay circuits, however a larger IOS range is still preferred as it relaxes the requirements on tracking speed and complexity of the ONU timing control algorithms.

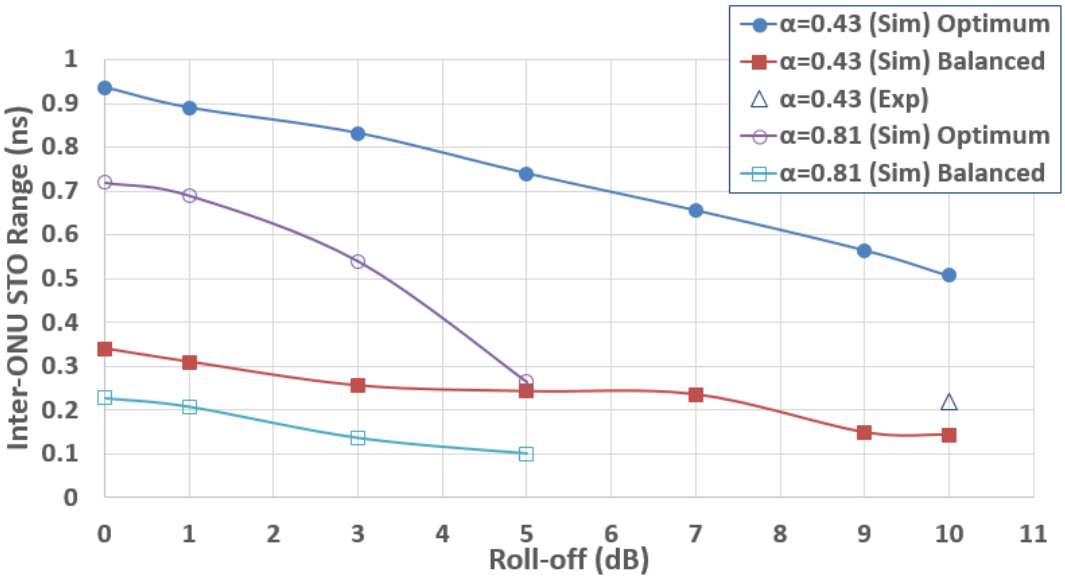

Fig. 5.13. Example of ONU BER versus receiver STO when the inter-ONU STO is 0.075 ns at 10 dB roll-off and α=0.43.

5.5 Conclusion

For the first time, upstream IMDD DFMA PON transmission has been experimentally demonstrated, by making use of two real-time reconfigurable OOFDM-modulated ONUs and an offline OLT. Experimental results have shown that the employed ONUs have similar upstream BER performances, negligible power penalties, excellent tolerance to inter-ONU STO, and large ONU launch power variation ranges. The proof-of-concept experimental work implies that the DFMA technique has great potential for implementing future SDN-based reconfigurable cloud access networks. In addition, as the channel roll-off effect is a key system feature impacting IMDD DFMA PON performance and as channel roll-off severity is highly design dependent, it is a key issue for component, transceiver and system designers to understand when balancing cost and performance. The tolerance of various performance characteristics to varying degrees of channel roll-off have therefore been fully investigated in a numerically simulated upstream IMDD DFMA PON, validated by strong agreement with experimentally obtained results. These results therefore provide important insights to facilitate the effective design of DFMA transceivers and PONs.

References

[1] M. Bolea, R. P. Giddings, M. Bouich, C. Aupetit-Berthelemot, and J.M. Tang, “Digital filter multiple access PONs with DSP-enabled software reconfigurability,” *IEEE/OSA J. Opt. Commun. Netw*., vol. 7, no. 4, pp. 215–222, Apr. 2015.

[2] W. Jin, X. Duan, Y. Dong, B. Cao, R. P. Giddings, C. F. Zhang, K. Qiu, and J. M. Tang, “DSP-enabled flexible ROADMs without optical filters and O-E-O conversions,” *J. Lightw. Technol*., vol. 33, no. 19, pp. 4124-4131, Oct. 2015.

[3] M. Bolea, R. P. Giddings, and J. M. Tang, "Digital orthogonal filter-enabled optical OFDM channel multiplexing for software-reconfigurable elastic PONs," *J. Lightw. Technol*., vol. 32, no 6, pp. 1200-1206, Mar. 2014.

[4] X. Duan, R. P. Giddings, M. Bolea, Y. Ling, B. Cao, S. Mansoor, and J. M. Tang, “Real-time experimental demonstrations of software reconfigurable optical OFDM transceivers utilizing DSP-based digital orthogonal filters for SDN PONs,” *Opt. Express*, vol. 22, no. 16, pp. 19674-19685, 2014.

[5] T. Tsuritani and X. Cao, “Transport SDN for integrating multi-optical technology networks,” in *Optical Fiber Communication Conference (OFC)*, Anaheim, 2016, paper Th3K.2.

[6] G. H. Im, D. D. Harman, G. Huang, A. V. Mandzik, M. H. Nguyen, and J. J. Werner, “51.84 Mb/s 16-CAP ATM LAN standard,” *IEEE J. Sel. Areas Comm*., vol. 13, no. 4, pp. 620–632, 1995.

[7] X. Duan, R. P. Giddings, M. Bolea, Y. Ling, B. Cao, S. Mansoor, and J. M. Tang, “Real-time experimental demonstrations of software reconfigurable optical OFDM transceivers utilizing DSP-based digital orthogonal filters for SDN PONs,” *Opt. Express*, vol. 22, no. 16, pp. 19674-19685, 2014.

[8] E. Al-rawachy, R. P. Giddings, and J. M. Tang, “Experimental demonstration of a DSP-based cross-channel interference cancellation technique for application in digital filter multiple access PONs,” *Opt. Express*, vol. 25, no. 4, pp. 3850-3862, 2017.

[9] J. L. Wei, A. Hamie, R. P. Giddings and J. M. Tang, "Semiconductor optical amplifier-enabled intensity modulation of adaptively modulated optical OFDM signals in SMF-based IMDD systems," *J. Lightwave Technol*., vol. 27, no. 16, pp. 3678–3688, 2009.

[10] X.Q. Jin, E. Hugues-Salas, R. P. Giddings, J. L. Wei, J. Groenewald, and J. M. Tang, "First real-time experimental demonstrations of 11.25Gb/s optical OFDMA PONs with adaptive dynamic bandwidth allocation," *Opt. Express*, vol. 19, no. 21, pp. 20557-20570, 2011.

[11] E. Al-Rawachy, R. P. Giddings, J. M. Tang, "Experimental demonstration of a DSP-based cross-channel interference cancellation technique for application in digital filter multiple access PONs," *Opt. Express*, vol. 25, no. 4, pp. 2850-3862, 2017.

[12] Y. Dong, E. Al-Rawachy, R.P. Giddings, W. Jin, D. Nesset, J.M. Tang, "Multiple channel interference cancellation of digital filter multiple access PONs," *J. Lightw. Technol*., vol. 35, no. 1, pp. 3444, Jan. 1, 2017.

[13] J. M. Tang and K. A. Shore, "30-Gb/s signal transmission over 40-km directly modulated DFB-laser-based single-mode-fiber links without optical amplification and dispersion compensation," *J. Lightwave Technol*., vol. 24, no. 6, pp. 2318–2327, 2006.

[14] J. L. Wei, A. Hamie, R. P. Giddings and J. M. Tang, "Semiconductor optical amplifier-enabled intensity modulation of adaptively modulated optical OFDM signals in SMF-based IMDD systems," *J. Lightwave Technol*., vol. 27, no. 16, pp. 3678–3688, Aug. 15, 2009.

6. Conclusions and Future Work

Contents

6.1 Conclusions

To satisfy the ever-increasing data traffic growth associated with a considerably diversified and unprecedented range of emerging network applications and services as well as reduce CAPEX and OPEX [1, 2], Cloud access networks have recently been proposed which seamlessly integrate traditional optical access networks, metropolitan optical networks and 4G/5G mobile fronthaul/backhaul networks. As discussed in Chapters 1-2, it is greatly advantageous if CANs not only have strong adaptability to highly dynamic traffic with arbitrary bandwidth granularity, but also simultaneously accommodate various major network design features including, for example, signal modulation format, signal detection scheme, WDM grid, multiple access technique, as well as network topology. In addition, CANs are also envisaged to be equipped with a wide diversity of SDN functionalities to dynamically provide flexible and fast on-demand connections/services with elastic bandwidth granularities at wavelength, sub-wavelength and sub-band levels. In this thesis, numerical and experimental investigations have been undertaken to explore the feasibility of practical implementation of three novel techniques essential for future CANs from device to network architecture level: i) software reconfigurable optical transceivers with channel multiplexing/demultiplexing in the digital domain without involving any extra analogue hardware, ii) DSP-switched O-E-O conversion-free flexible ROADMs, and iii) DFMA PONs with DSP-enabled software reconfigurability.

As software reconfigurable adaptive optical transceivers, employing digital integrated circuit-based DSP, are the fundamental building blocks of CANs in the physical layer, in Chapter 3, both experimental and numerical investigations are undertaken to explore the technical feasibility of newly proposed software reconfigurable transceivers utilizing digital orthogonal filters embedded in DSP logic. Using numerical simulations, impacts of major transceiver design aspects including number of digital filter taps and different modulation formats on the transmission performance is explored in a IMDD SSMF system consisting two independent, digital orthogonal filter multiplexed channels employing OFDM modulation. To further validate the proposed transceivers, real-time experimental demonstrations of on-line software reconfigurable adaptive OOFDM transceivers are reported, for the first time, where two real-valued OOFDM modulated channels are multiplexed/demultiplexed utilizing field programmable gate array (FPGA)-based 32-tap digital orthogonal filters in the digital domain without involving any sophisticated signal

conversion in the RF domain and/or IQ modulation in the optical domain. The transmission performance and channel reconfigurability of the transceivers are experimentally examined in simple 25km standard single-mode fibre (SSMF) IMDD systems, over which experimental explorations are also undertaken of the inherent transceiver adaptability enabled by adaptive bit loading.

Having explored the software reconfigurable optical transceivers in Chapter 3, in Chapter 4 the focus is shifted to another key optical device, the cost-effective and flexible ROADMs which, in combination with the reconfigurable transceivers from Chapter 3, play a vital role in offering fast and flexible reconfiguration of network connectivity in CANs. In this chapter, both experimental and numerical investigations are undertaken to explore the newly proposed DSP-enabled flexible ROADMs in IMDD-based optical network nodes. Using numerical simulations, add and drop operation characteristics of the proposed ROADMs are investigated which clearly demonstrate the feasibility of the proposed technology. To further validate the feasibility of the proposed ROADMs, experimental demonstration are performed where the physical-layer add and drop operation performances of the proposed ROADMs are fully investigated. The demonstrated ROADMs are shown to be robust to variations in both differential optical power dynamic range and drop RF signal power variation.

In addition to exploring the software reconfigurable optical devices including transceivers and ROADMs, in Chapter 5, experimental investigations are first undertaken to explore multipoint-to-point upstream signal transmission in IMDD DFMA PONs for application in CANs using two real-time, reconfigurable, OOFDM-modulated ONUs and an offline OLT. Experimental demonstrations show that each ONU achieves similar upstream BER performance, excellent tolerance to inter-ONU sample timing offset and a relatively large ONU launch power variation range. Moreover, as channel frequency response roll-off influences the orthogonality between the spectrum-sharing orthogonal DFMA channels thus leading to CCI and subsequent system performance degradation in DFMA PONs, the impact of various levels of channel frequency response roll-off on transmission performance are numerically investigated in a 2 channel upstream IMDD DFMA PONs employing OOFDM. For two different signal bandwidths, transmission performance is analysed in terms of BER versus received optical power performance, ONU transmission capacity, ONU launch power variation range and inter-ONU STO. Over all the aforementioned aspects, good agreements

are obtained between numerical simulations and the corresponding experimental measurements. The observed results are valuable for facilitating the implementation of cost-effective designs of both DFMA transceivers and IMDD DFMA PONs for application in CANs.

6.2 Future Work

Although extensive research work has been undertaken in this thesis on reconfigurable CANs and the great potential of the proposed technologies have been demonstrated, there are still a number of technical issues to be researched in order to fully validate and verify the technical and commercial feasibility of the associated CAN technologies. Some of the key future areas of research work are as follows:

1) Automatic control and/or compensation of transceiver clock frequencies and sample timings in DFMA PONs.

   As discussed in Chapter 5, in order to maintain the orthogonality between different ONUs operating on orthogonal channels, it is necessary to adjust the relative sample timing offset (STO) between ONUs until the ONUs achieve orthogonality and thus reach their best transmission performance. Therefore, it is necessary to investigate and develop DSP algorithms which can estimate and automatically adjust the relative STO between different ONUs. Furthermore, as absolute STO is critical in a DFMA receiver DSP algorithms must also be developed to automatically adjust or compensate for STO in the DFMA receiver. It is also of course necessary to develop solutions to account for sampling frequency offset (SFO) between ONUs and OLTs, however as SFO typically results in a drift in STO, algorithms could be designed for combined STO and SFO compensation. As all network elements are under SDN control, the SDN-controller can also potentially be employed to aid the timing/frequency synchronisation and simplify the required DSP algorithms.

2) Automatic control of drop RF signal amplitude, frequency and phase in flexible ROADMs.

To perform the drop operation at orthogonal sub-band level in the proposed DSP-switched flexible ROADMs in Chapter 4, manual adjustment of amplitude, frequency and phase of the drop RF signal was employed to select the sub-band to be dropped. It is therefore necessary to explore and develop solutions for automatic control of the drop RF signal to optimize drop operation performance for each sub-band. The desired RF drop signal parameters are set by the SDN controller, however for optimum performance the set values must be continuously tuned to follow any drift in the drop signal parameters. As the TETs can more easily monitor add/drop signal parameters the SDN controller can again be potentially utilised to provide a connection between TETs and ROADMs for optimum control of the RF drop signal parameters.

3) The impact on transmission performance of concatenated flexible ROADMs in a CAN.

From the practical deployment perspective, as illustrated in Chapter 2, multiple flexible ROADMs need to be concatenated in a ring-type network for CANs. Such concatenation can have a potential impact on system transmission performance. Therefore both numerical and experimental investigations should be undertaken to address this issue and determine the maximum number of ROADMs that can be concatenated for various scenarios.

4) Real-time demonstration of CCIC in DFMA transceivers.

As seen in Chapter 5, the cross-talk effect between the spectrum-sharing orthogonal DFMA channels is the major physical mechanism limiting the upstream DFMA PONs transmission performance. Recently a DSP-based CCIC technique [3] has been experimentally demonstrated in a two channel point-to-point IMDD-based DFMA PON system. To further evaluate the technical potential of CCIC technique for practical application in future CANs, it is thus vital to conduct research in real-time experimental demonstration of this technique in a multipoint-to-point DFMA PON system.

5) Experimental demonstration of DFMA PONs using multiple orthogonal channels

In Chapter 5, only two orthogonal channels at the same frequency has been considered. To further evaluate the proposed DFMA PON technique, upstream DFMA PON transmission of multiple channels at different frequencies should be experimentally

investigated. In addition, according to theoretical simulations [4] significant CCIs only exist between orthogonal channels. Therefore the CCIs on both orthogonal channels and those channels occupying different frequencies should be experimentally verified.

References

[1] P. Chanclou, A. Cui, F. Geilhardt, J. Nakamura and D. Nesset, "Network operator requirements for the next generation of optical access networks," *IEEE Netw*., vol. 26, no. 2, pp. 8-14, Mar. 2012.

[2] J. E. Mitchell, "Integrated wireless backhaul over optical access networks," *J. Lightw. Technol*., vol. 32, no. 20, pp. 3373-3382, Oct. 2014.

[3] E. Al-Rawachy, R. P. Giddings, J. M. Tang, "Experimental demonstration of a DSP-based cross-channel interference cancellation technique for application in digital filter multiple access PONs," *Opt. Express*, vol. 25, no. 4, pp. 2850-3862, 2017.

[4] Y. Dong, E. Al-Rawachy, R.P. Giddings, W. Jin, D. Nesset, J.M. Tang, "Multiple channel interference cancellation of digital filter multiple access PONs," *J. Lightw. Technol*., vol. 35, no. 1, pp. 34-44, Jan. 1, 2017.

Appendix

Journal Publications

[1] M. L. Deng, **X. Duan**, W. Jin, R.P. Giddings, S. Mansoor, and J.M. Tang, "Experimental Demonstration and Performance Evaluation of DSP-Switched Flexible ROADMs for Cloud Access Networks," *Optics Communications*, submitted.

[2] W. Jin, C. F. Zhang, X. L. Zhang, **X. Duan**, Y. X. Dong, R. P. Giddings, K. Qiu, and J. M. Tang, "OSNR Penalty-Free Add/Drop Performance of DSP-Enabled ROADMs in Coherent Systems," *J. Opt. Commun. Netw*., vol. 9, no. 9, pp. 730-738, 2017.

[3] **X. Duan**, R.P. Giddings, S. Mansoor, and J.M. Tang, "Performance Tolerance of IMDD DFMA PONs to Channel Frequency Response Roll-off," *IEEE Photon. Technol. Lett*., vol. 29, no. 19, pp. 1655-1658, 2017.

[4] **X. Duan**, R.P. Giddings, S. Mansoor, and J.M. Tang, "Experimental Demonstration of Upstream Transmission in Digital Filter Multiple Access PONs With Real-Time Reconfigurable Optical Network Units," *J. Opt. Commun. Netw*., vol. 9, no. 1, pp. 45-52, 2017.

[5] W. Jin, C. Zhang, **X. Duan**, M.R. Kadhum, Y. X. Dong, R.P. Giddings, N. Jiang, K. Qiu, and J. M. Tang, "Improved Performance Robustness of DSP-Enabled Flexible ROADMs Free from Optical Filters and O-E-O Conversions", *J. Opt. Commun. Netw*., vol. 8, no. 8, pp. 521-529 (2016).

[6] W. Jin, **X. Duan**, Y. X. Dong, B. Y. Cao, R. P. Giddings, C. F. Zhang, K. Qiu and J. M. Tang, "DSP-Enabled Flexible ROADMs without Optical Filters and O-E-O Conversions", Journal of Lightwave Technology, vol. 33, no. 19, pp. 4124-4131 (2015).

[7] M. L. Deng, N. Jiang, **X. Duan**, R. P. Giddings, X. W. Yi, B. Y. Cao, S. Mansoor, K. Qiu, and J.M. Tang, "Robust and tunable 16.375Gb/s dual-band optical OFDM

tranmissions over directly modulated VCSEL-based 200m OM2 MMFs" *Opt. Express*, vol. 23, no. 1, pp. 373-383 (2015).

[8] **X. Duan**, R.P. Giddings, M. Bolea, Y. Ling, B. Cao, S. Mansoor, and J.M. Tang, "Real-time experimental demonstrations of software reconfigurable optical OFDM transceivers utilizing DSP-based digital orthogonal filters for SDN PONs" *Opt. Express*, Vol. 22, no. 16, pp. 19674-19685 (2014).

Conference Publications

[1] **X. Duan**, M. L. Deng, W. Jin, R.P. Giddings, S. Mansoor, and J.M. Tang, "Experimental Demonstration of DSP-enabled Drop Operations of Flexible ROADMs Excluding Optical Filters and O-E-O Conversions" *Optical Fiber Communication Conference (OFC)*, Anaheim, 2016, paper M3E.4.

[2] R.P. Giddings, **X. Duan**, and J.M. Tang, "Experimental Demonstration of Cross-Channel Interference Cancellation for Digital Filter Multiple Access PONs" *Optical Fiber Communication Conference (OFC)*, Anaheim, 2016, paper Th3C.5.

[3] M. Bolea, **X. Duan**, R.P. Giddings and J.M. Tang, "Software Reconfigurable PONs Utilizing Digital Filter Multiple Access" *European Conference on Networks and Communications (EUCNC)*, Paris, 2015.

[4] W. Jin, **X. Duan**, M. Bolea, R.P. Giddings, N. Jiang, C.F. Zhang, K. Qiu and J.M. Tang, "New ROADMs with DSP-Enabled Dynamic and Flexible Operations for Elastic Optical Networks" *Optical Fiber Communication Conference (OFC)*, Los Angeles, 2015, paper Th2A.50.

[5] B. Y. Cao, M.L. Deng, R.P. Giddings, **X. Duan**, Q.W. Zhang, M. Wang and J.M. Tang, "RSOA Intensity Modulator Frequency Chirp-Enabled 40Gb/s over 25km IMDD PON Systems" *Optical Fiber Communication Conference (OFC)*, Los Angeles, 2015, paper W1J.3.

[6] **X. Duan**, R. P. Giddings, M. Bolea, Y. Ling, S. P. Mansoor and J. M. Tang, "Real-time Demonstrations of Software Reconfigurable Optical OFDM Transceivers Utilising DSP-based Digital Orthogonal Filters for Channel Multiplexing" *Asia Communications and Photonics Conference (ACP)*, Shanghai, 2014, paper AW3E.1.